Unsaturated soils: constitutive modelling and explicit stress integration

Wojciech Tomasz Solowski

Durham University

School of Engineering

Unsaturated soils: constitutive modelling and explicit stress integration

Wojciech Tomasz Sołowski

PhD thesis

0 7 OCT 2008

July 2008

Table of Content

3

Abbreviations

AEV – Air entry value, the suction value at which soil desaturates

BBM – Barcelona Basic Model, constitutive model proposed by Alonso et al. (1990)

ENPC – Ecole Nationale des Ponts et Chaussées (Paris, France)

EPFL – Ecole Polytechnique Fédérale de Lausanne (Lausanne, Switzerland)

ESEM – Environmental Scanning Electron Microscopy

MC-BBM – Multi-cell enhanced Barcelona Basic Model

RMC-BBM – Random multi-cell enhanced Barcelona Basic Model

MCC – Modified Cam Clay

MIP – Mercury Intrusion Porosimetry

MUSE – Mechanics of Unsaturated Soil for Engineering

RK – Runge-Kutta

SEM – Scanning Electron Microscopy

UPC – Universitat Politécnica de Catalunya (Barcelona, Spain)

List of symbols

<u>Capital letters</u>

C – suction capacity (after Marinho 1994)

I – elasto-plastic tangent matrix

$\mathbf{D}^{el}$ – elastic tangent matrix

$\mathbf{D}_{sec}$ – secant elastic matrix (elastic stress integration)

$\mathbf{D}_c^{(i)}$ – tangent elasto-plastic (or elastic) matrix corresponding to cell c in i-th iteration of stress integration

$\mathbf{E}$, E_{ij} – error tensor, error in component (i,j)

E_{av} – average error

F – yield function

F – compressive force between the spheres connected by meniscus (chapter 5)

G – shear modulus

G – plastic potential function

K – bulk modulus, secant bulk modulus (elastic stress integration)

K_p – secant bulk modulus corresponding to mean net stress change (elastic stress integration)

K_s – bulk modulus corresponding to suction change (elastic stress integration)

M – slope of the critical state line in the p – q space

N(0) – BBM – specific volume for virgin compressed soil at reference mean stress p^c

N(s) – BBM – specific volume for virgin compressed soil reached reference mean stress p^c and suction s

N_i – number of equally sized subincrements in i-th calculation of stress with extrapolation method

NoS – Number of stages in given Runge-Kutta method.

S_r – degree of saturation

T – surface tension

TOL – tolerance value, describes accepted error in stress integration

V – volume; V_s, V_w, V_a refers to volume of solids, water and air (gas) phase respectively

V_m – volume of a meniscus connecting two soil grains

6

<u>Letters</u>

abs – absolute value

c' – cohesion at zero matric suction and zero net normal stress

c – cell number (section 6.4)

e – void ratio

e_w – water ratio

$\mathbf{h}$ - (vector of) hardening parameter(s)

$\delta\mathbf{h}_i^{(s)}$ - s-th estimation of (vector of) hardening parameter(s) in i-th subincrement

i – cell number (chapter 5)

i – subincrement number

k – BBM – parameter describing the increase in cohesion with suction at atmospheric pressure

k_1, k_1 – coupling parameters in Wheeler et al. model (2003)

m – mass; m_w and m_s refer to mass of water and mass of solids respectively.

m – order of Runge-Kutta method, used in assessing next subincrement size

n – porosity

n – number of cells in multi-cell enhanced model (chapter 5, section 6.4)

p – mean net stress

p_{agg} – total mean stress within aggregates

p_{atm} – atmospheric pressure

p^c – BBM – reference mean stress

p' – normalised mean net stress

p_0^* – preconsolidation stress for saturated conditions, hardening parameter in BBM

p_0^* – preconsolidation stress, hardening parameter in Wheeler et al (2003) model

q – shear stress

q' – normalised shear stress

r – parameter defining the maximum soil stiffness

r – radius of a soil grain (chapter 3)

r_1, r_2 – radii of meniscus connecting soil grains of radius r

s – suction (difference between the pore water and atmospheric pressures)

s^* – modified suction equal to suction multiplied by porosity s^*=ns used in Wheeler et al. model (2003)

$\overset{\bullet}{s_I}$, $\overset{\bullet}{s_D}$ - hardening parameters of Wheeler et al. (2003) model describing suction increase and suction decrease yield losuc

u_w – water pressure

u_a – air pressure

w – water content

w_v – volumetric water content

w_r – residual water content

w_s – water content at saturation

Greek letters

α, α_0, α_1 – scalar parameters used in Pegasus algorithm, referring to the percentage of elastic strain (chapter 6).

α - parameter describing amount of elastic strain (chapter 7)

β – parameter controlling the rate of increase of soil stiffness with suction

$\delta\varepsilon_i$ – i-th strain subincrement

$\Delta\varepsilon$ – strain increment

$\Delta\varepsilon^{enh}$ – enhanced strain increment (with additional 7th component – suction change)

$\Delta\varepsilon_v$ – volumetric strain increment

$\Delta\varepsilon_q$ – shear strain increment

$\Delta\varepsilon_{v,s}$ – change of volumetric strain due to suction change (elastic stress integration)

$\Delta\varepsilon_{v,p}$ – change of volumetric strain due to mean net stress change (elastic stress integration)

ε – strain tensor; in particular ε_{ij} (i, j =1,2,3) refers to the ij component of strain tensor

ε_v – volumetric strain

ε_q – shear strain

ε_{pl}, ε^p – plastic strain

ε_{el}, ε^e – elastic strain

ϕ' – internal friction angle associated with net normal stress

ϕ^b – internal friction angle associated with suction

κ – slope of the elastic loading – unloading line in the log (p) – v plot ,

κ_s – BBM – slope of the elastic loading – unloading line in the log (s) – v plot,

κ_s – Wheeler et al (2003) – slope of elastic line in the water retention curve, given in log (modified suction s^*) – degree of saturation plane

λ – stiffness parameter for changes in mean net stress for virgin states of soil (slope of the normal compression line for saturated conditions)

$\lambda(s)$ – stiffness parameter for changes in mean net stress for virgin states of soil for given value of suction (slope of the normal compression line for unsaturated conditions)

λ_s – gradient of primary drying and wetting curves in Wheeler et al (2003) model

Λ – scalar plastic multiplier

ξ – scalar 'safety' factor used in calculation of size of next subincrement

$\delta\sigma_i$ – i-th integrated stress subincrement

$\delta\sigma_i^{(j)}$ – j-th stress estimate used to calculate i-th stress subincrement

$\Delta\sigma_i^{(m)}$ – m-th level extrapolation of i-th stress estimate (extrapolation method)

$\sigma_{av}^{(i)}$ – average stress across all the cells in multi-cell enhanced model in i-th iteration of stress integration

σ – stress tensor; in particular σ_{ij} (i, j =1,2,3) refers to the ij component of stress tensor

$\sigma_A, \sigma_B, \sigma_C$ – stress state: at the beginning of subincrement (A), at the end of subincrement (B) and after drift correction (C)

σ_{ij}^* – 'effective' stress used in Wheeler et al. (2003) model, see eq. (4.16)

χ – effective stress parameter

v – specific volume of soil

List of Figures

List of Tables

Acknowledgments

this page is intentionally left blank

1. Introduction and definitions

This thesis deals with the modelling of partially saturated soils and the explicit stress integration of elasto-plastic constitutive models idealising the behaviour of such soils.

The document is divided into 8 chapters. This short chapter describes the thesis structure and introduces some commonly used definitions. Chapter two provides a review of key features found in unsaturated soils. Both the macroscopic behaviour and microscopic behaviour of partially saturated soils are described. Chapter three gives some insight into the microscale modelling of unsaturated soils and provides some results regarding the influence of suction on the unsaturated soil fabric. Chapter four describes existing constitutive models for unsaturated soils. The models discussed include both those predicting deformation of unsaturated soils under loading, as well as those for the water retention behaviour. Chapter five introduces the novel concept of a multi-cell enhanced model and the implementation of this concept for the Barcelona Basic Model. Chapter six reports on the explicit stress integration of constitutive models for unsaturated soils. It covers several Runge-Kutta algorithms and an extrapolation algorithm for stress integration. The details of their implementation for the Barcelona Basic Model are given. Chapter seven provides a thorough comparison between those stress integration methods and chapter eight presents a final summary of the main findings from the thesis.

Original developments include: (i) results on micromechanics given in chapter three, (ii) the multi-cell concept, (iii) implementation of Runge-Kutta methods for stress integration for the Barcelona Basic Model given in chapter six, (iv) use of the extrapolation method for stress integration as given in chapter six, (v) the stress integration algorithm for multi-cell enhanced model (chapter six), (vi) a set of benchmark tests to evaluate the performance of the stress integration schemes for the Barcelona Basic Model (chapter seven) and (vii) accuracy, robustness and efficiency comparisons between various integration schemes (chapter seven). This work may be of particular interest to computational geomechanicians and those engaged in the detailed analysis of engineering structures comprising unsaturated soils.

1.1. Definitions

In this section commonly used terms in soil mechanics and unsaturated soil mechanics are defined (although it is assumed that the reader has a good knowledge of solid mechanics).

1.1.1. Coordinate system used

Through the thesis a Cartesian coordinate system is used. The axes are usually denoted by numbers 1, 2 and 3 corresponding to the x, y and z axes.

1.1.2. Stress quantities and suction

The total mean stress is defined as an average of the direct stresses: $\frac{1}{3}(\sigma_{11} + \sigma_{22} + \sigma_{33})$

The mean net stress p is defined as a difference between total mean stress and air pressure (usually atmospheric pressure)

$$p = \frac{1}{3}(\sigma_{11} + \sigma_{22} + \sigma_{33}) - u_a \overset{usually}{=} \frac{1}{3}(\sigma_{11} + \sigma_{22} + \sigma_{33}) - p_{at}$$

The shear stress is defined by stress tensor components as

$$q = \sqrt{\frac{1}{2}\left((\sigma_{11} - \sigma_{22})^2 + (\sigma_{11} - \sigma_{33})^2 + (\sigma_{22} - \sigma_{33})^2 + 6(\sigma_{12}^2 + \sigma_{13}^2 + \sigma_{23}^2)\right)}$$

Suction is the difference between the air pressure and water pressure

$$s = u_a - u_w$$

In unsaturated soils, due to capillary forces, the soil water pressure is less then the atmospheric pressure and thus suction, s, is a positive quantity.

1.1.3. Strain and quantities describing deformations

Volumetric strain is defined as sum of direct strains $\varepsilon_v = \varepsilon_{11} + \varepsilon_{22} + \varepsilon_{33}$. The shear strain is defined as

$$\varepsilon_q = \frac{\sqrt{2}}{3}\sqrt{\left[(\varepsilon_{11} - \varepsilon_{22})^2 + (\varepsilon_{11} - \varepsilon_{33})^2 + (\varepsilon_{22} - \varepsilon_{33})^2\right] + 6(\varepsilon_{11}^2 + \varepsilon_{22}^2 + \varepsilon_{33}^2)}$$

The unsaturated soil volume V may be divided into the volume of solids (volume of soil grains) V_s, volume of pore fluid V_w and volume of gas V_a, where $V = V_s + V_w + V_a$. The void ratio e is the proportion of volume of voids and water to volume of solids

$e = \dfrac{V_a + V_w}{V_s}$ whereas specific volume v is the volume of soil divided by the volume of

soil grains $v = \dfrac{V}{V_s} = e + 1$.

1.1.4. Quantities describing water content

In saturated soil, if one wishes to characterise the amount of water present in soil it is enough to give the void ratio of soil. The other often used quantity is water content, being the ratio of masses of water and solid particles in any soil volume $w = \dfrac{m_w}{m_s}$. The amount of water can be also often given in terms of volumetric water content defined as ratio of volume of water and total soil volume $w_v = \dfrac{V_w}{V}$. However, in the case of unsaturated soils the most often used quantity describing the amount of water is the degree of saturation S_r. The degree of saturation is defined as the volume of water divided by volume of water and air in soil $S_r = \dfrac{V_w}{V_a + V_w}$. The other quantity characteristic to unsaturated soils is the water ratio e_w defined as ratio of the volume of water and volume of solids $e_w = \dfrac{V_w}{V_s}$.

2. Review of key features of unsaturated soil behaviour

Unsaturated soils are encountered frequently above the water table level and thus must be often dealt with in engineering practice. However, until recently, the behaviour of unsaturated soils has not been extensively researched. It is only during the last twenty years that the unsaturated soil has become an important topic within geotechnical engineering. This branch of geomechanics has been slow to reach practicing engineers. It currently is understood only by academic scholars and few specialist soil mechanicians. Thus, in engineering practice, more often than not, such soil is still treated as fully saturated. In this chapter some features of the unsaturated soil behaviour are discussed and explained.

This chapter covers only the most important aspects of unsaturated soil behaviour due to changes in water content and mechanical loading. The behaviour described is typical for clayey or silty soil. Soils with little or no fine grain content (e.g. sand, gravel, and other coarse grained materials) and soils with substantial organic content (e.g. peat) will behave differently.

2.1. Macroscopic behaviour

This section focuses on the macroscopic behaviour of unsaturated soil. The macroscopic behaviour is here defined as the behaviour observed where the soil is treated as a continuum instead of discrete soil grains. Then, the quantities such as soil deformation are relatively easy to observe and measure using conventional instruments and laboratory equipment usual to geotechnics. In contrast, the microscopic behaviour is spoken about when the changes in single soil grains or small clusters of soil particles are observed. The investigation of the microscopic soil behaviour requires either electro-scanning microscope or indirect tests such as Mercury Intrustion Porosimetry (MIP).

2.1.1. Mechanical behaviour

Suction is the variable that is used instead of pore water pressure in partially saturated soils. Suction is defined as the difference between the air pressure and pore water pressure and is generally higher the dryer a soil is. As long as suction and degree of saturation of soil may be regarded as constant, then the behaviour of unsaturated soil is

very similar to the behaviour of a fully saturated one (including features like e.g. small strain nonlinearity). It is expected that deformations of unsaturated soil will be smaller compared to the fully saturated soil. This typical behaviour of unsaturated soils is illustrated in Fig. 2.1. (Sharma 1998). It is clear that the higher the suction is, the higher is the yielding point and the stiffer is the soil before yielding. A constitutive model created for saturated soils but calibrated for a given unsaturated soil should be able to predict soil behaviour with similar accuracy as for the saturated soil, as long as suction remains constant. For a useful description of saturated soil behaviour see e.g. Muir Wood (1990).
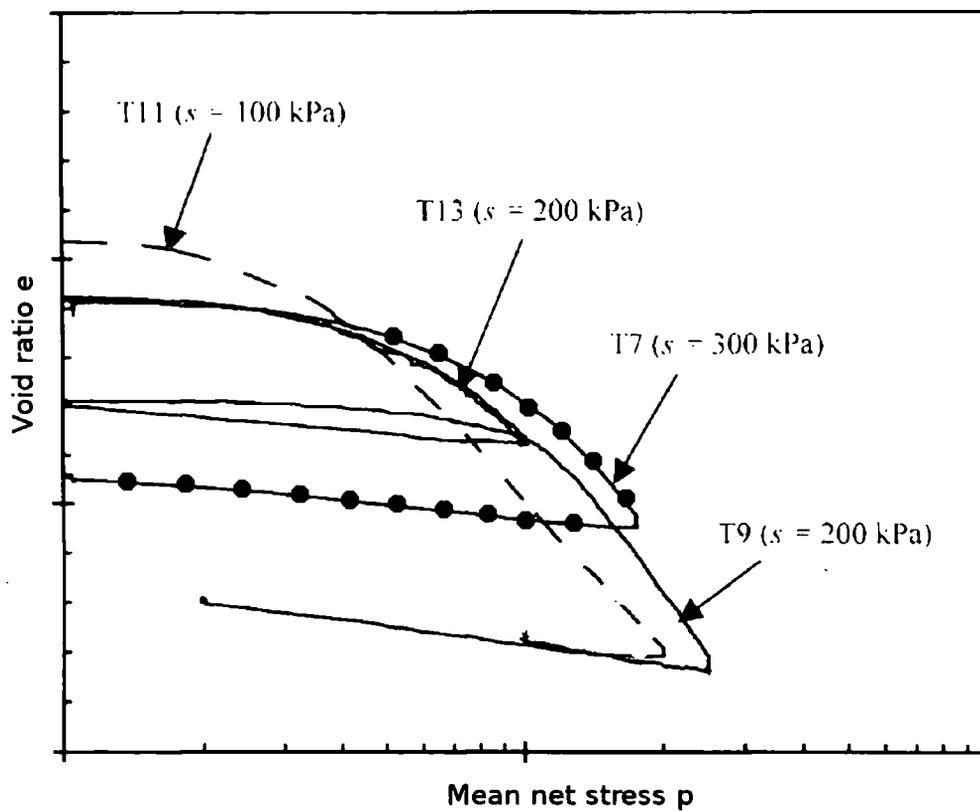
Figure 2.1. Increase in soil stiffness and resistance with suction increase under mean net stress loading (after Sharma 1998).

The increase in mean stress invariably leads to volume reduction in soils. It has been suggested that this behaviour can be described by a bilinear relationship in the e – ln p plane. In particular, when the soil is compressed beyond a certain level, the slope of this line becomes steeper and the soil deforms irreversible (that is, elasto-plastically). This steeper line is commonly referred to as a virgin compression line. The slope of virgin compression line for unsaturated soil may not be constant and may depend on suction

for some soils, as suggested by Alonso et al. (1990, Fig. 2.2). It is, however, not clear whether the suction dependence of this slope is characteristic for all unsaturated soils and how significant this effect is, as in most of the recently published experimental data the slopes of fully yielded virgin compression lines appear similar (see e.g. Wheeler & Sivakumar 1995, shown on Fig. 2.3, Sharma 1998, Barrera 2002). On the other hand, some evidence suggests that the slope of virgin compression line changes also at constant suction, when sufficiently high loading is considered. Thus, it is likely that during a mean net stress increase, the unsaturated virgin compression line may initially be less steep than the saturated one (as the transition between elastic and elasto-plastic regions in unsaturated soils is less pronounced than for the saturated soils), then upon further loading those lines become parallel to each other and finally the virgin compression lines for unsaturated and saturated states become closer together (see Fig. 2.4.). Such behaviour is confirmed by the maximum amount of possible collapse (e.g. Yudhbir 1982, González and Colmenares 2006, Sun et. al 2007b), see also Fig. 2.5. Note that for high mean net stresses the description in the commonly used $e - \ln p$ space is rather imperfect and use of a $\ln e - \ln p$ space is advised, as advocated by Butterfield (1979).
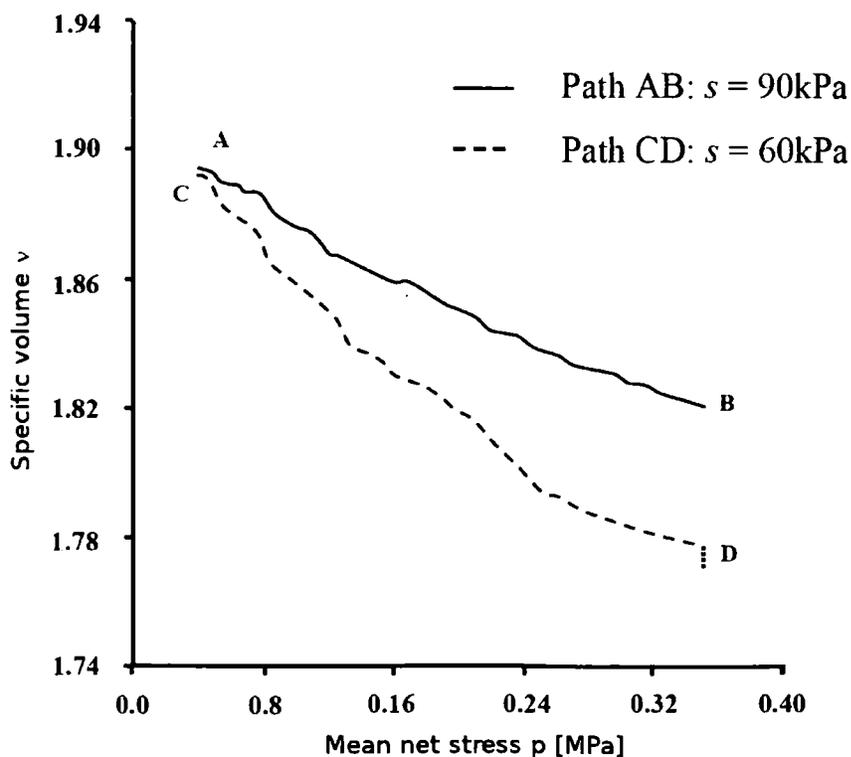
Figure 2.2. Virgin compression lines slopes for suction s=60 and s=90 kPa (after Alonso et al. 1990).
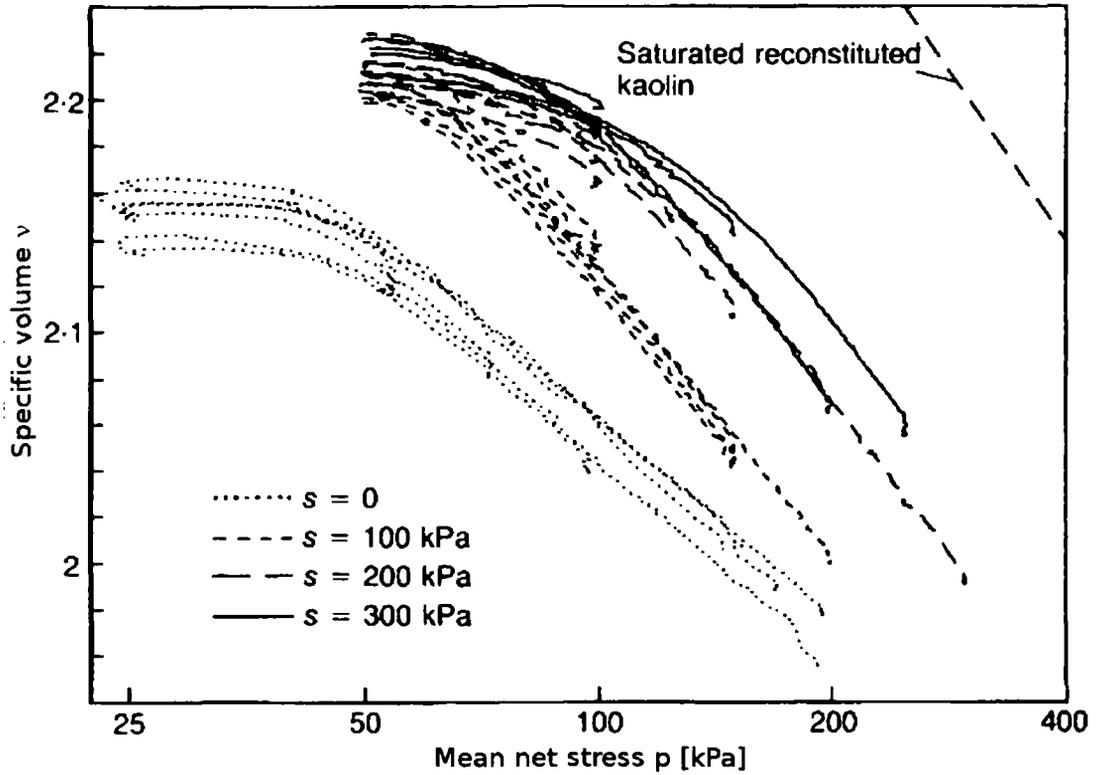
Figure 2.3. Isotropic compression tests for suctions 0, 100, 200 and 300 kPa (after Wheeler and Sivakumar 1995). Note that virgin compression lines corresponding to the reconstituted saturated kaolin and kaolin with non-zero suction have very similar slopes.
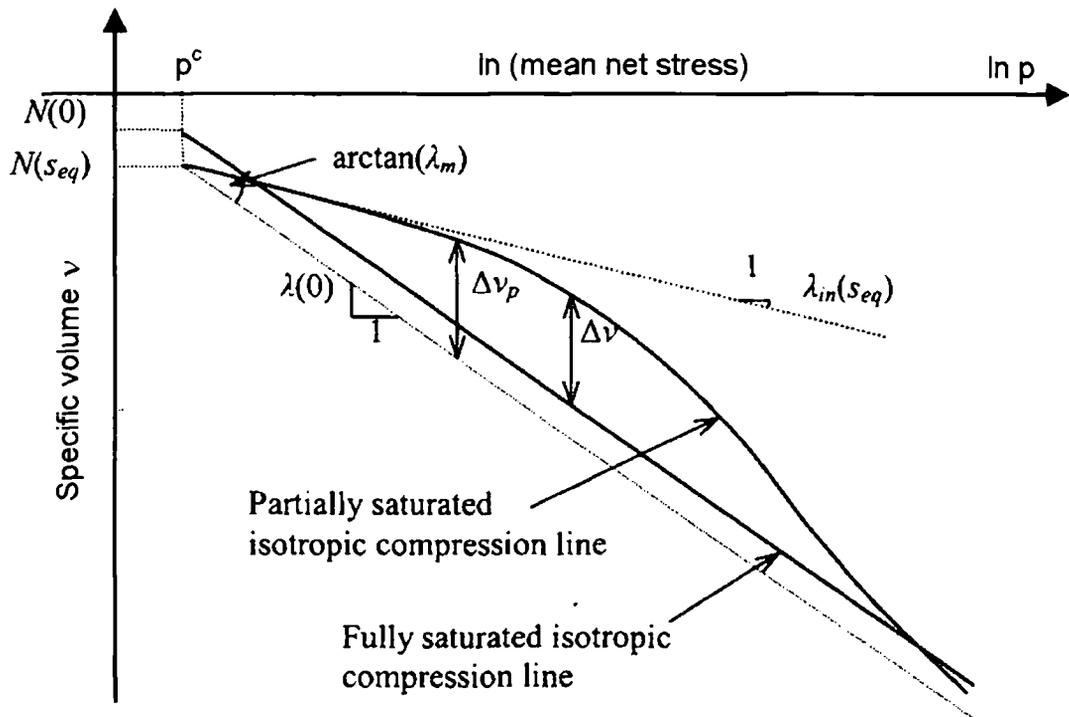
Figure 2.4. Schematic of isotropic compression line for fully saturated and partially saturated soil (after Georgiadis et al. 2005). The amount of collapse initially increases then reduces, in line with the results presented by Sun et al. (2007), see Fig. 2.5.
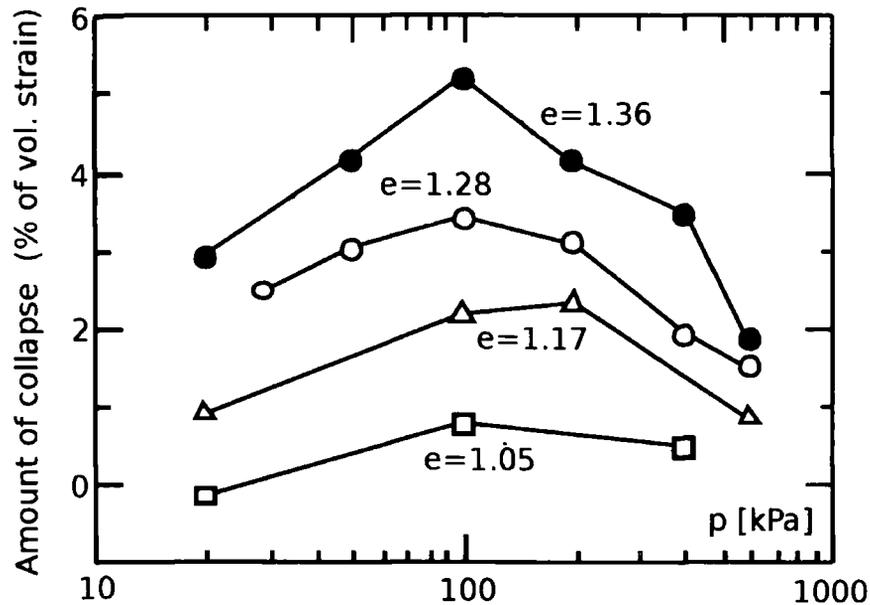
Figure 2.5. Amount of collapse for compacted soil samples to different initial void ratio. The relative amount of collapse decreases in high mean net stresses (after Sun et al. 2007b).

Most constitutive models use a framework similar to the one for saturated soils, thus suggesting that the virgin compression behaviour is well described by straight lines in the semi-log or log-log plots. Models that do not assume straight virgin compression lines for partially saturated soil are relatively scarce. Such models have been proposed by Georgiadis et al. (2005) and Russel and Khalili (2005) (though it appears that the latter model was mostly designed for coarse grained soils).

When the effects of changes in suction and water content are investigated, it has been observed that soils generally shrink while dried and swell while wetted. During drying the suction increases and the soil becomes stiffer. The soil behaves purely elastically at higher stress levels and thus the elasto-plastic deformations are much smaller compared to the fully saturated case (see Fig. 2.1).

When an unsaturated soil is wetted, suction decreases. If this decrease happens under a mean stress much lower than the historical maximum (i.e. for heavily overconsolidated soil), then the soil swells. However, the soil that is under a high mean net stress (for example when deforming elasto-plastically while unsaturated) is likely to reduce its specific volume during wetting, contrary to the expected swelling behaviour of the unloaded soil (although, some initial swelling is possible). Such a reduction in the void ratio during wetting is usually referred to as a collapse and is unique to unsaturated soils. The collapse behaviour has been observed in great many laboratory tests (e.g. Josa

1988, Sivakumar 1993, Sharma 1998, Geiser 1999, Romero 1999, Barrera 2002, Colmenares 2002, Vasallo 2003, Jotisankasa 2005 and Monroy 2005 provide recent findings, see also Fig. 2.5). However, despite a large number of tests, the understanding of collapse is still somewhat limited. This is shown by Colmenares (2002), who not only reports that after full saturation and collapse the specific volume of soil does not necessarily lie on the virgin compression line for saturated soil (which is the usual assumption in constitutive modelling) but also that 'there is insufficient evidence in this work to conclude that yield caused by loading is similar mechanistically to yield caused by wetting'.

The amount of shrinkage and swelling in a soil during drying and wetting is not easy to assess. Most often it is assumed that this behaviour is fully elastic (as typically assumed in the Barcelona Basic Model, though originally described as elasto-plastic by Alonso et al. 1990) or elasto-plastic (Wheeler et al. 2003). In general, the constitutive models for unsaturated soils struggle to accurately predict the outcome of multiple cycles of drying and wetting. Even for a fairly uncomplicated stress path, consisting only of isotropic loading, unloading and some wetting and drying (as given in Fig. 2.6), most models do not predict soil behaviour similar to that one observed in the laboratory test.

The dilative and contractive behaviour during shearing, seen in saturated soils is also present in unsaturated soils. Some experimental evidence suggests that the higher the suction is, the more dilation during shearing the soil exhibits and the higher is its shear angle (e.g. Vaunat et al. 2007, Fig. 2.7).

Once other external influences are included, unsaturated soil behaviour becomes more complex, exhibiting hydro-thermo-chemo-mechanical coupling. The thermo-chemo aspects are beyond the scope of this thesis. The reader is referred to Romero (1999), Villar (2000) and Sanchez et al. (2005) for further information on this subject.
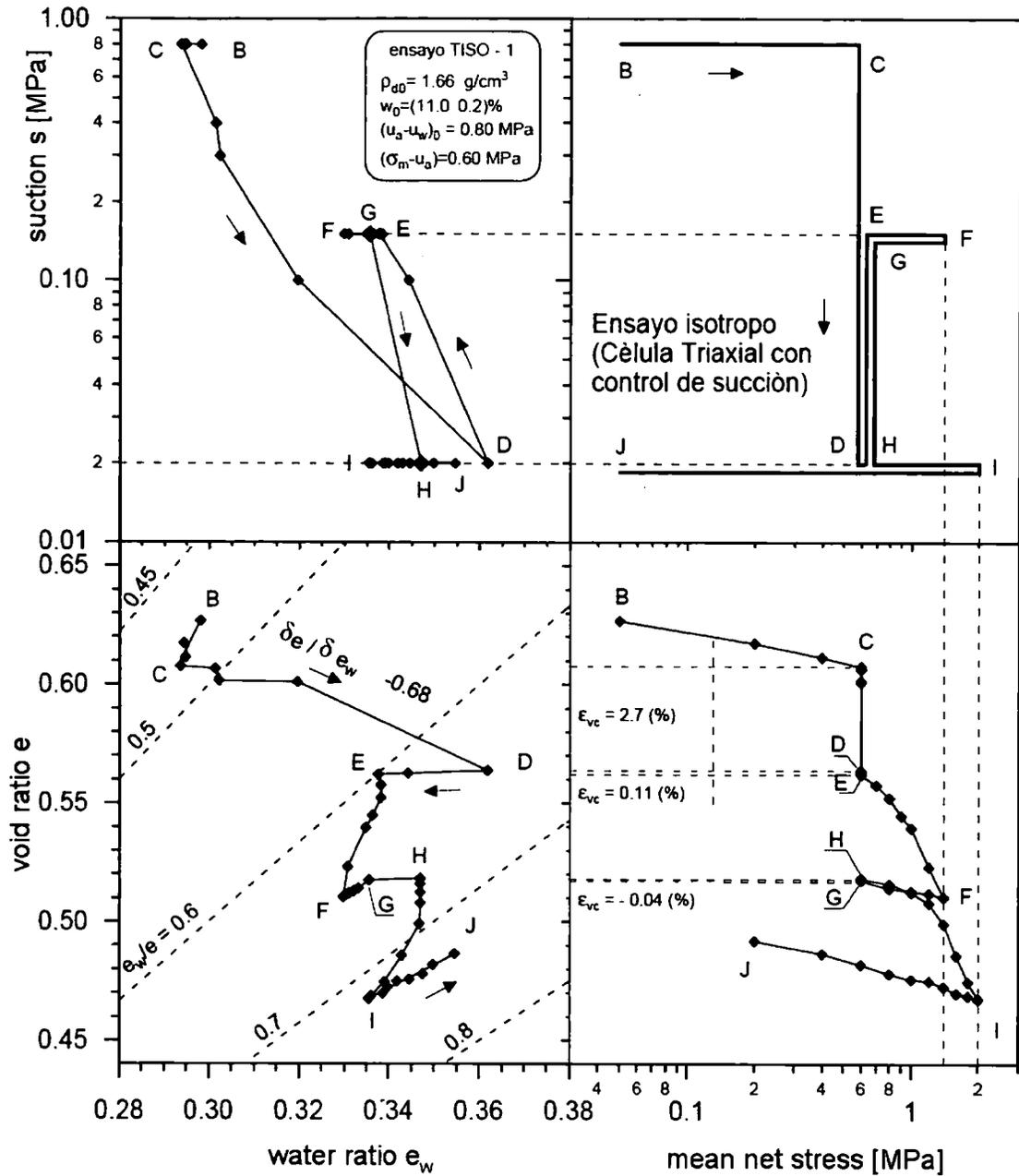
Figure 2.6. Mean net stress loading of a compacted sample with changes in suction (after Barrera 2002).
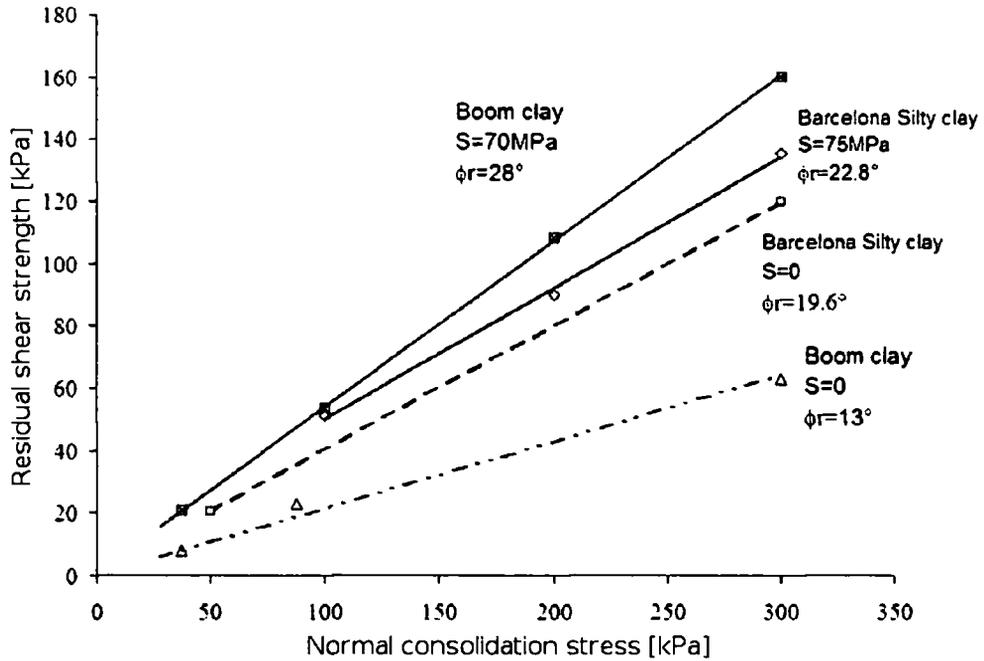
Figure 2.7. Residual shear resistance envelopes for saturated and unsaturated (s=70MPa) Boom clay and Barcelona silty clay (at s=75 MPa, after Vaunat et al. 2007).

2.1.2. Water retention behaviour

The water retention behaviour describes the relation between the suction and degree of saturation for given state of soil. This relation has been found not to be unique since the water retention behaviour is influenced heavily by the history of soil. Both the mechanical history of soil and the hydrological (wetting and drying) are important.

In particular, the degree of saturation versus suction curve obtained from soil dried from a fully saturated state is often referred to as main drying curve, whereas the curve obtained from a fully dry state is often referred to as main wetting curve. The hysteretic curves connecting the main wetting and main drying curves are usually referred to as the scanning curves (see Fig. 2.8).

To describe the soil behaviour during drying one clearly needs, apart of the relation between the water content and suction, an understanding of the volumetric behaviour. Marinho (1994) observed that a fully saturated soil subjected to drying will initially shrink. The loss of volume due to shrinkage is the same as the volume of evaporated water as confirmed by Marinho (1994). Thus, the soil remains fully saturated and the suction should be acting as an additional pressure. At some point the soil ceases to be fully saturated. This happens when the suction equals to the Air Entry Value (AEV, which is sometimes referred to as the bubbling pressure).
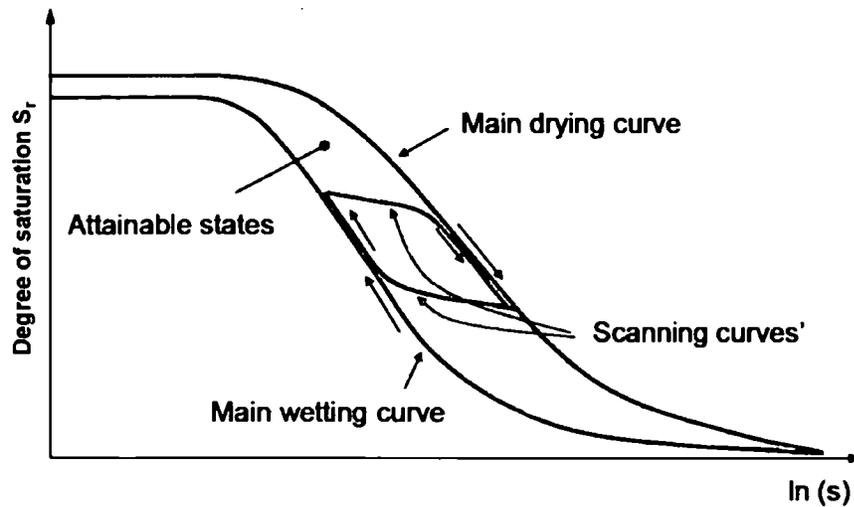
Figure 2.8. Typical water retention behaviour (after Tarantino 2007). Note that the difference in degree of saturation after a full drying-wetting cycle is rather exaggerated.

Upon attaining the AEV, the soil volume can be divided into dry and wet regions. The dry zones are not compressed with suction, whereas the wet parts are compressed with increasing suction during drying (and some additional forces due to surface tension). Finally one may hypothesise that this process leads to creation of a double structure in soil. It has been found (e.g. Marinho 1994) that the soil usually does not shrink much after suction has reached the AEV. This may be because there is part of soil where suction is not acting and thus it is not being compressed.

While the unsaturated soil is being mechanically compressed it has been found (e.g. Cuisinier and Laloui 2004, Monroy 2005) that the larger pores, which become unsaturated first, decrease in volume much more than the smaller pores (see Fig. 2.9.). Thus, as the AEV depends mostly on the size of largest pores, the AEV changes during mechanical loading. It is not just the AEV but also the water retention behaviour which is altered.

As the water retention behaviour describes the relationship between the degree of saturation and suction, it is clear that when at some given suction we start to compress the soil undrained (i.e. keeping the water volume in soil constant), the degree of saturation of soil will rise and the suction will drop. This decrease of suction will be smaller than the decrease of suction reached at the same degree of saturation during wetting. This is possibly due to the volume of the larger pores decreasing more than the volume of the smaller pores during mechanical loading and thus the overall degree of

33

saturation being higher for the same amount of suction than in the case of wetting (see e.g. Tarantino 2007, 2008).
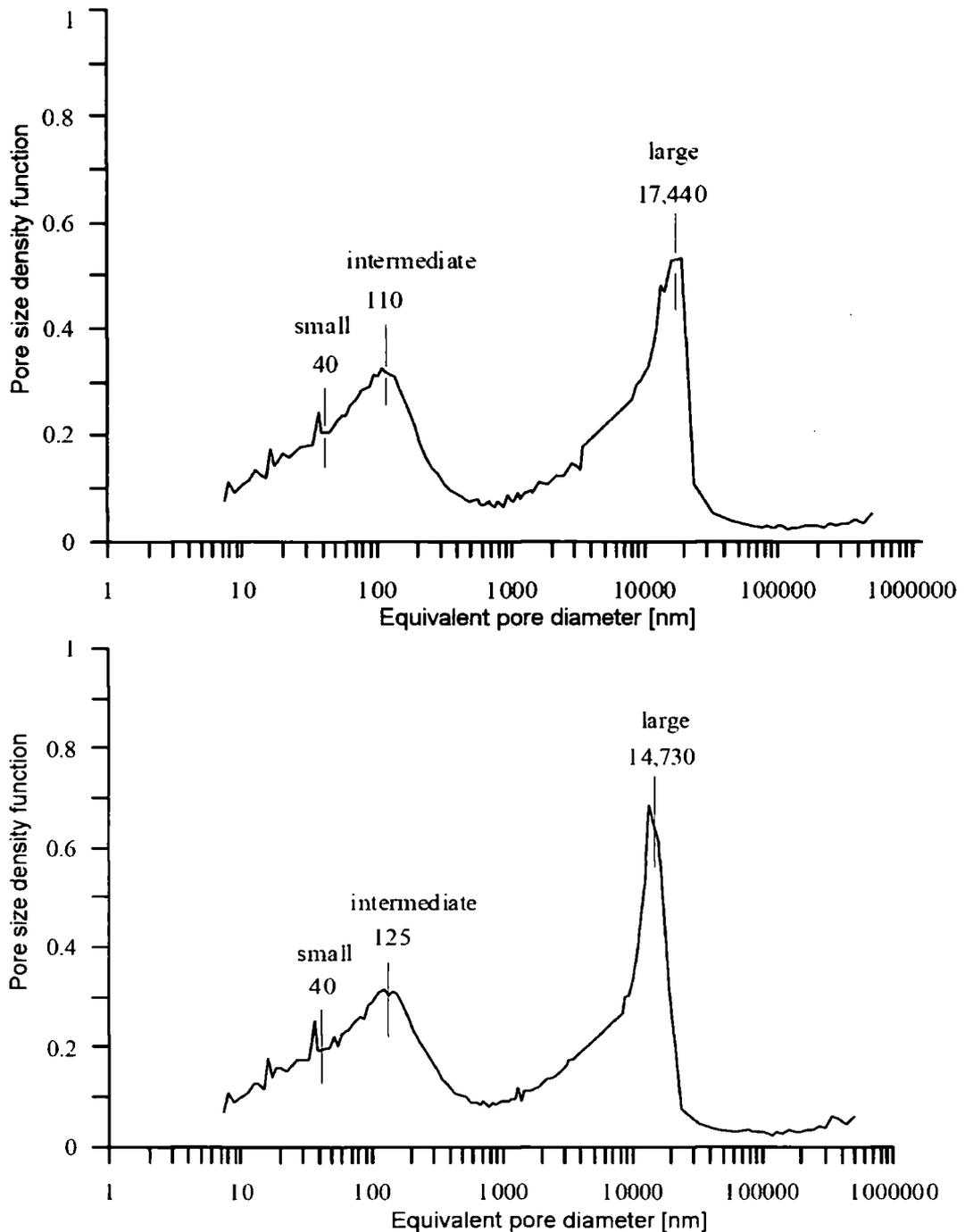
Figure 2.9. Pore size distribution at the initial state (top) and after mean net stress loading (bottom) at constant water content for compacted London Clay (after Monroy 2005).

As mentioned before, the water retention curve depends on whether the soil is being dried or wetted. This difference has often been explained by the 'ink-bottle' effect (e.g. Hillel 1998, Lourenço 2008). The 'ink bottle' effect is explained by the existence of

large pores connected to the other pores via much smaller pores. Those smaller pores will not dry until a much higher value of suction is reached, thus some water is trapped in the larger pores. This effect does not exist during wetting. This gives rise to a difference in the water retention behaviour (note that during wetting some air may be trapped in the soil pores such that a degree of saturation equal to 1 may be difficult to obtain, compare Fig. 2.8). To experimentally check the ink-bottle hypothesis one may try to induce small cyclic deformations on unsaturated soil (preferably in the elastic range), just large enough to break the ink-bottle effect and check whether the water retention curves merge. Other explanations of the hysteresis phenomena include effects of contact angle (as the contact angle will be different when the meniscus is advancing or retreating), and the effect of chemical swelling/shrinking of soil minerals due to the presence of water. Finally, recently Lechman et al. (2006) researched disk-shaped particles and obtained hysteretic water retention curve basing on a thermodynamical energy stability concept without explicit involvement of the contact angle and ink-bottle hypothesis.

Some research suggests that the water retention curves obtained for the same soil but with different loading history (and different stress state during wetting and drying) may merge into one curve while being plotted in the appropriate space. Marinho (1994) suggest a log s − w/C space, where s - suction, w - water content and C - suction capacity. Suction capacity C is defined as $\delta w / \delta \log s$. Tarantino (2007, 2008) suggest plotting water retention curve in log s − log e_w space (where e_w is the water ratio being ratio between volume of water and volume of solids) or in log s − log e'_w space (where e'_w stands for modified water ratio, being the ratio of the volume of water reduced by the volume of water attached to soil at infinite suction). The ideas of Marinho (1994) has been investigated further by Harrison and Blight (2000). Recently Marinho (2005) found some empirical connection between the value of suction capacity C, liquid limit, plastic limit, normalised water content and water retention curve and provided a relevant set of graphs for simple water retention curve identification.

Unfortunately, thus far there is relatively little understanding of the physical reasons why the water retention curves should merge when plotted in modified space. It is also not clear what are the effects of multiple cycles of wetting and drying on the water retention behaviour and whether the effect of such cycles is similar to the effects of the mechanical loading.

2.1.3. Shear strength

A change in suction has a strong influence on the shear strength of soil. It is generally agreed that an increase of suction leads to an increase of the shear strength (as shown in Fig. 2.7.). Increase in suction results both in increase of the shear angle and cohesion of soil (Vaunat et al. 2007). However, some contrary evidence exists. Nishimura and Toyota (2002) report that, in the case of silty soil they tested, the shear strength is not always increasing with increasing suction. Instead it peaks for some value of suction and further drying may lead to a decrease in the shear strength from that peak value (see Fig. 2.10.). Similar results have been obtained by Vesga and Vallejo (2006) (Fig. 2.11) who tested unsaturated kaolinite clay. They found that the shear strength peaks at suction between 1 and 10 MPa which corresponds to water contents of a little over 10%. Further increase of suction over 10 MPa led to reductions in shear and tensile strengths. They suggested that this decrease in both shear and tensile strengths at high suction is due to a reduction of capillary forces between soil particles as the amount of water in soil is insufficient.
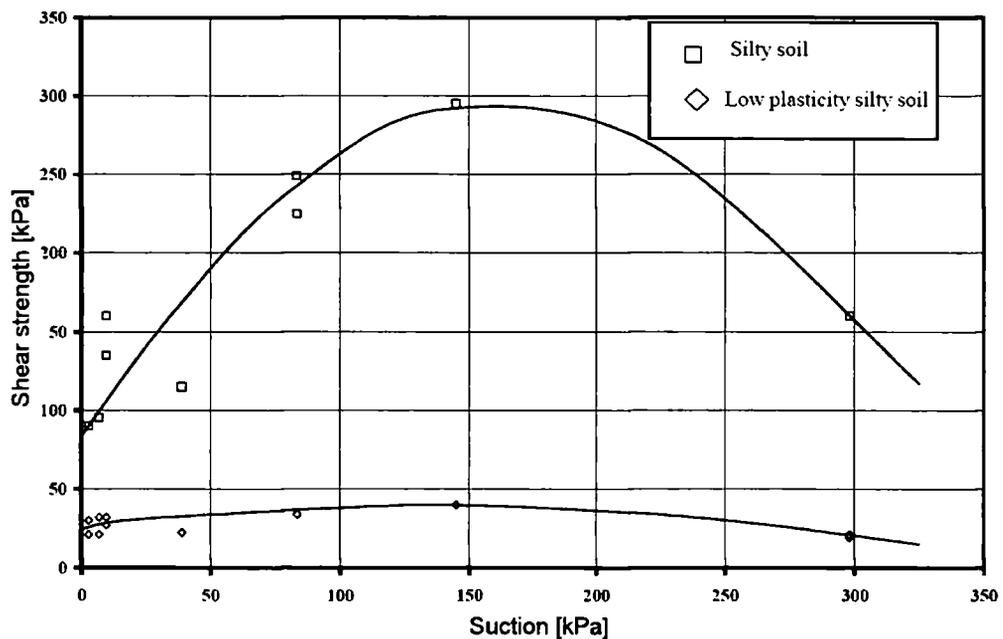
Figure 2.10. Shear strength of silty/ low plasticity silty soil (after Monroy 2005, data from Nishimura and Toyota 2002).
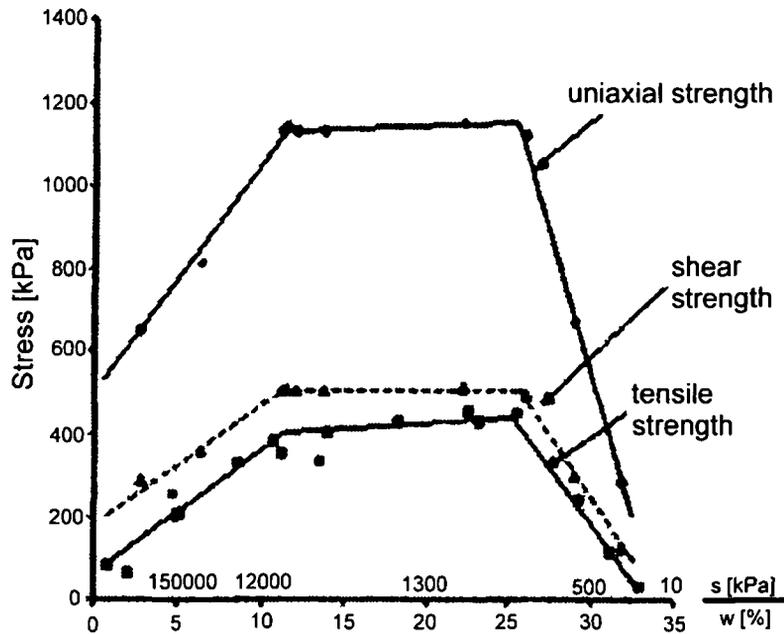
Figure 2.11. Shear strength and tensile strength of kaolinite clay with varying water content/suction. Suction values approximate (after Vesga and Vallejo 2006).
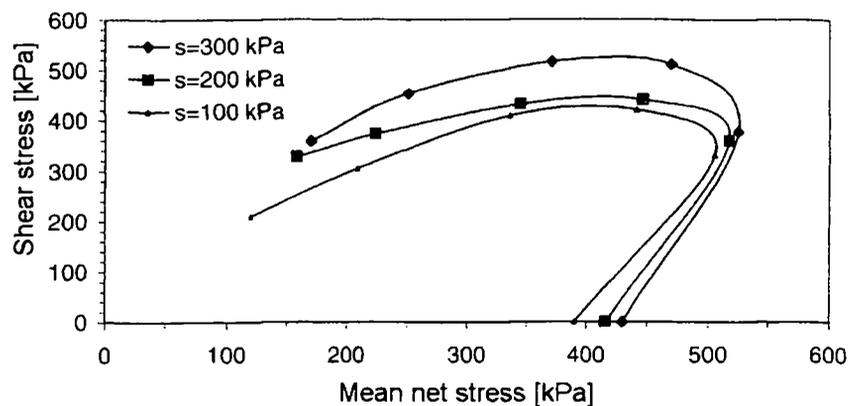
Figure 2.12. Yield locus shape for increasing suction (after Estabargh and Javadi 2005).

Finally, the shear strength is heavily influenced by anisotropy (Cui 1993, Cui and Delage 1996). It seems that the yield surface in the mean net stress - shear stress (p – q) space should rather have the shape of a rotated or sheared ellipse which is dependent on the soil history. The laboratory data from Estabargh and Javadi (2005) confirms that such a yield surface should be used in conjunction with a non-associated flow rule, perhaps additionally depending on the suction value (see Figs 2.12, 2.13).

37
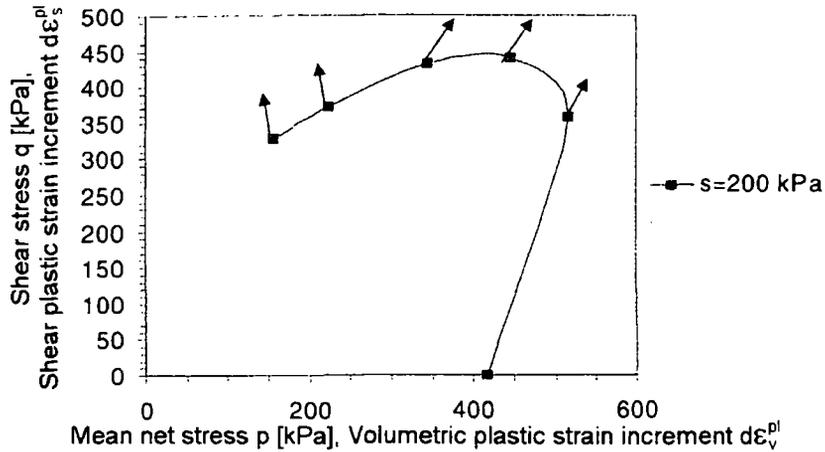
Figure 2.13. Plastic strain increment directions (after Estabargh and Javadi 2005).

In engineering analyses the shear strength is most often assessed by extending the Mohr-Coulomb criterion into unsaturated states (see Fredlund and Rahardjo 1993). The extended criterion is

$$\tau = c' + (\sigma_\perp - u_a)\tan\phi^a + s\tan\phi^b \tag{2.1}$$

where c' is the cohesion at zero matric suction and zero net normal stress, $\sigma_\perp - u_a$ is the net normal stress at failure, ϕ^a is the internal friction angle associated with net normal stress and ϕ^b is the internal friction angle associated with suction. This criterion has often been modified and is used with the Bishop stress (see Bishop 1954, 1959)

$$\tau = c' + (\sigma_\perp - u_a + \chi s)\tan\phi' \tag{2.2}$$

where χ is the effective stress parameter. It has been suggested (e.g. Houlsby 1997) that the effective stress parameter χ should be equal to degree of saturation S_r

$$\sigma_{ij} = \sigma_{ij} - (S_r u_w + (1-S_r)u_a)\delta_{ij} = \sigma_{ij} - (u_a - S_r s)\delta_{ij} \tag{2.3}$$

The same equation has been arrived at by e.g. Hutter et al. (1999) (who used the framework of mixture theory, Hassanizadeh and Gray 1990) and Li (2007).

It will be shown in chapter 3 that this stress definition is, allowing for some simplifying assumption, equal to the average skeleton stress in soil.

2.2. On the way to understand unsaturated soil

The structure (that is the configuration of the grains or fabric) and structure evolution within unsaturated soils has its importance acknowledged for a long time (e.g. Alonso et

38

al. 1987). As a consequence of the recent research into unsaturated soil microstructure it is now possible to offer an explanation of some of the phenomena seen on the macroscopic level based on changes in the microstructure. Unfortunately there is still not enough evidence about the changes in microstructure of unsaturated soils, thus much of this section is speculative, based on the laboratory data available. Future research may render this obsolete.

2.2.1. Laboratory tests revealing soil microstructure

There are several ways to examine the soil microstructure. The most direct is to observe the fabric using Scanning Electron Microscopy (SEM). This technique was described by Gillot (1973) and perfected e.g. by Delage et al. (1982, 1984). The sample for SEM observation initially needed to be frozen and then freeze-dried. With introduction of Environmental SEM (ESEM) freezing is not always required. The SEM images of unsaturated soils may be found in many recent publications, e.g. Delage (1996), Romero (1999), Barrera (2002), Zhang et al. (2003), Jafari and Shafiee (2004), Monroy (2005) and Thom et al. (2007). However, due to the very nature of SEM images they do not provide 'hard evidence' of soil behaviour as they can just offer an insight into the local structure of fabric. To the best of the author's knowledge they have not been used to calibrate a constitutive model.

In general, the SEM images usually show that the smallest clay platelets tend to be organised into larger entities which are typically referred to as aggregates. The presence of those aggregates seems to be connected with method of preparation of the soil. The reconstituted saturated soil does not seem to have particles organised in aggregates (Monroy 2005).

The other source of information about soil microstructure is via mercury intrusion porosimetry (MIP). The samples for MIP are prepared similarly as for the SEM; they are frozen and then vacuum freeze-dried (see e.g. Romero 1999). The prepared sample is inserted into a probe, then the air is pumped out and mercury intruded. Because of the negative value of contact angle and high surface tension of mercury the pressure required to fill the pores of the sample is quite high and easy to measure. Knowing the pressure and the contact angle of mercury, it is possible (using the Jurin – Young – Laplace equation) to calculate the smallest radius of a pore that is currently filled with mercury. Unfortunately, the injection of the mercury may change the structure of the part of the sample that is not yet filled with mercury. Also, it is arguable what value of

contact angle should be used. In summary, the MIP tests offer only an approximation of the pore size structure of a given soil.

The MIP reveals that many unsaturated soils exhibit two maximums on the pore size distribution curve – one corresponding to the large, intra-aggregate pores and the other corresponding to the small inter-aggregate pores. This confirms the findings from the SEM images that two levels of structure exist in the fabric. The pores between the aggregates correspond to the macroporosity revealed by the MIP, whereas the microporosity is porosity within aggregates, between the clay platelets. MIP data may be found e.g. in Cuisinier and Laloui (2004), Monroy (2005) and Thom et al. (2007).

MIP data also show that in some cases the unsaturated soil does not exhibit double structure. This may happen when the soil is dried from the mould, without the crushing and compacting stage. Such unsaturated soil may have different properties and generally is not considered in this work. Some data on such soil can be found in Barrera (2002) and Gasprarre (2005). The requirements for creation of double structured or single structured soil upon drying from remoulded state are, however, unclear.

It should be recognised that the soil microstructure is sensitive to certain chemical species in the pore water. Such soil, although dried from the mould, is likely to develop a double structure (Wang and Siu 2006a,b , Wang and Xu 2007, Dolinar and Trauner 2007, see also Fig. 2.19). Similarly, the introduction of some stabilisers like lime, changes the soil microstructure, greatly increasing the volume of the smallest pores and reducing the overall porosity (Russo et al. 2007).

The double structured soil required for laboratory tests is usually obtained from remoulded soil. Such remoulded soil is (i) initially dried (in a dryer), then (ii) grinded or sieved and (iii) compacted. Before sieving and/or upon compaction a small quantity of water is added. Soil is usually compacted dynamically in Proctor machine (e.g. Sharma 1998, Monroy 2005), though a static compaction under isotropic pressure is also possible (e.g. Barrera 2002). The water content of soil during Proctor compaction usually corresponds to dry of optimum or optimum water content. Toll (2000) suggests that soils compacted with degree of saturation below 90% are likely to be aggregated. This has been partially confirmed by Toll & Ong (2003) where samples compacted with water content wet of optimum (at water content 15.6% vs. optimum 14.2%, soil with plastic limit of 22% and liquid limit of 36%) exhibit double structure.

Schematically the process of creation of double structured soil is given in Fig. 2.14 and a description of a typical sample preparation (for tests performed by Sharma, see Sharma 1998) is given in section 5.2.3.

Such prepared and compacted soil exhibits double structure and results in a high initial value of suction. Thus to reach a required value of suction for a given test, some amount of water is added before the test.

remoulded   dried soil   grinding /   compaction   double
soil   sieving   structured
                                                        soil
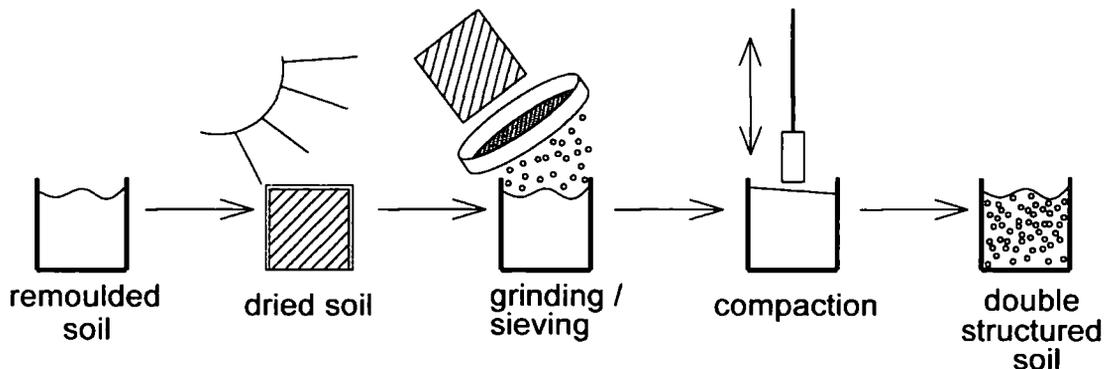
Figure 2.14. Typical sample preparation for unsaturated soil testing resulting in double structured soil.

2.2.2. Loading and unloading under constant suction

During the mechanical loading of soil, with a mean net stress exceeding the maximum historical stress experienced by the soil fabric, the pores between aggregates decrease in volume and radius substantially. However, the small pore volume (corresponding to the intra-aggregate porosity) is reduced only by a small percentage (see Cuisinier and Laloui 2004, tests on silt, Fig. 2.15) or virtually unaffected (Miao et al. 2007). A small change in the intra-aggregate porosity is also observed by Monroy (2005), see Fig. 2.9, though in this test the suction varied as water content was kept constant. It appears likely that the external stress mostly affects the way the aggregates are positioned against each other. The aggregates may also change their shape, but this is not accompanied by significant changes in their volume. The larger pores become smaller thus the porosity curve may shifts slightly in the direction of smaller pores as observed by Cuisinier and Laloui (2004). It is apparent that during loading the largest pores are most affected; they are the first to disappear (Fig. 2.15).

When the soil is subsequently unloaded, fewer large pores are recovered, though the porosity curve shifts slightly in the direction of larger pores. If soil is now loaded again to the value of mean net stress experienced previously, then the reduction of volume is much smaller. Again, upon further unloading not the whole volume of macropores is recovered. Macroscopically, such loading corresponds to cycles of isotropic

compression and unloading. The experiments confirm that the volume of voids in soil fabric will decrease with each cycle (e.g. Ferber et al. 2006). It also appears that the higher the suction is, the smaller is the volume change in the macropores. This is likely to be an effect of the aggregates being much stiffer and more resistant to stress resulting in smaller changes of aggregate shape.

From a physical point of view, it may be that the plastic change of volume in soil corresponds to the inelastic shape changes of aggregates. Then the elastic changes in volume would be a result of bending the clay platelets between and within aggregates. During cyclic loading, the elasto-plastic effect would be inevitable as in each cycle of loading and unloading the clay particles generally would not only bend but also slip, which would result in a plastic change of volume.
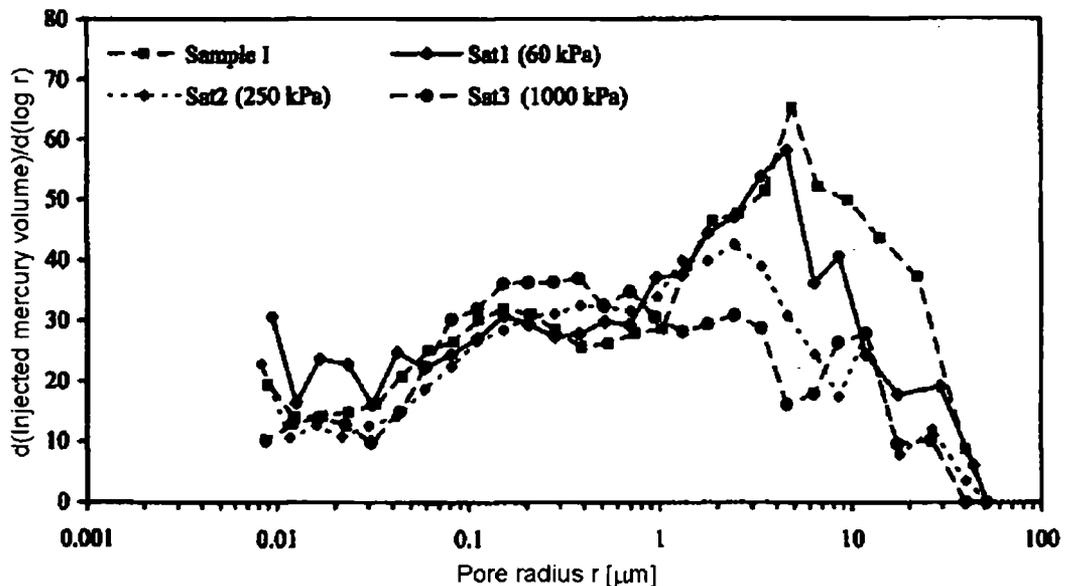
Figure 2.15. Evolution of soil fabric under mechanical loading in saturated state. Values in brackets indicate maximum mean stress applied (after Cuisinier and Laloui 2004)

2.2.3. Effects of suction changes on soil microstructure

The wetting and drying of soil lead to a highly complex interaction between micro- and macrostructure of soil fabric. The reader should be aware that some of the results given in this section may be soil specific, so more research would be required to reach any definite conclusion.

Assuming an initial double structured soil with high suction, wetting under low mean net stress should lead to swelling. Once the soil is allowed to swell without changing the

load, its double porosity reduces and the porosity curve exhibit the peak in the range of mesopores and smaller peak in the range of macropores (Monroy 2005, tests on London Clay). When the London Clay is wetted, while the volume is kept constant, the peak in large pores is less pronounced and the volume of meso and macro pores is reduced (Monroy 2005, Fig. 2.16.).

On the other hand, Cuisinier and Laloui (2004) report that the double porosity is recovered when the silt they tested (and which had double structure initially) is dried from the saturated state (Fig. 2.17). They noted that when drying from a fully saturated state the volume of micro and macropores rises. This suggests that the soil particles become organised into aggregates (Fig. 2.18).

Such findings may not be universal – some research suggests that in some soils the dried soil with a single peak of porosity may just shrink uniformly and no double structure may be created (Koliji 2008), especially when the drying is performed on a heavily loaded soil. Such soil behaviour, with hypothetical requirements for double structure creation is schematically presented in Fig 2.20.

Ferber et al (2006) found that upon cyclic drying and wetting, the inter-aggregate volume seems to systematically decrease. This could be explained by the clay platelets inside the aggregates rearranging (optimising) their position in the aggregates during each cycle of wetting and drying, adding plastic deformation.

The effects of shearing on the soil microstructure are little known. However, the research of Vaunat et al. (2007), Fig. 2.7, implies that the higher the suction is and the stiffer the aggregates are, then more shear resistance is exhibited and the greater dilation observed. This may suggest that the behaviour of dry soil with aggregates tend to resemble the behaviour of soil composed of larger soil grains (coarser grained soils have higher shear angle and dilate more), as suggested Toll (1990). On the other hand, Vesga and Vallejo (2006) suggest that at low water content the amount of water in soil may be not sufficient to connect all the aggregates and thus drying above some value of suction may actually lead to a reduction of the shear strength from the peak value.
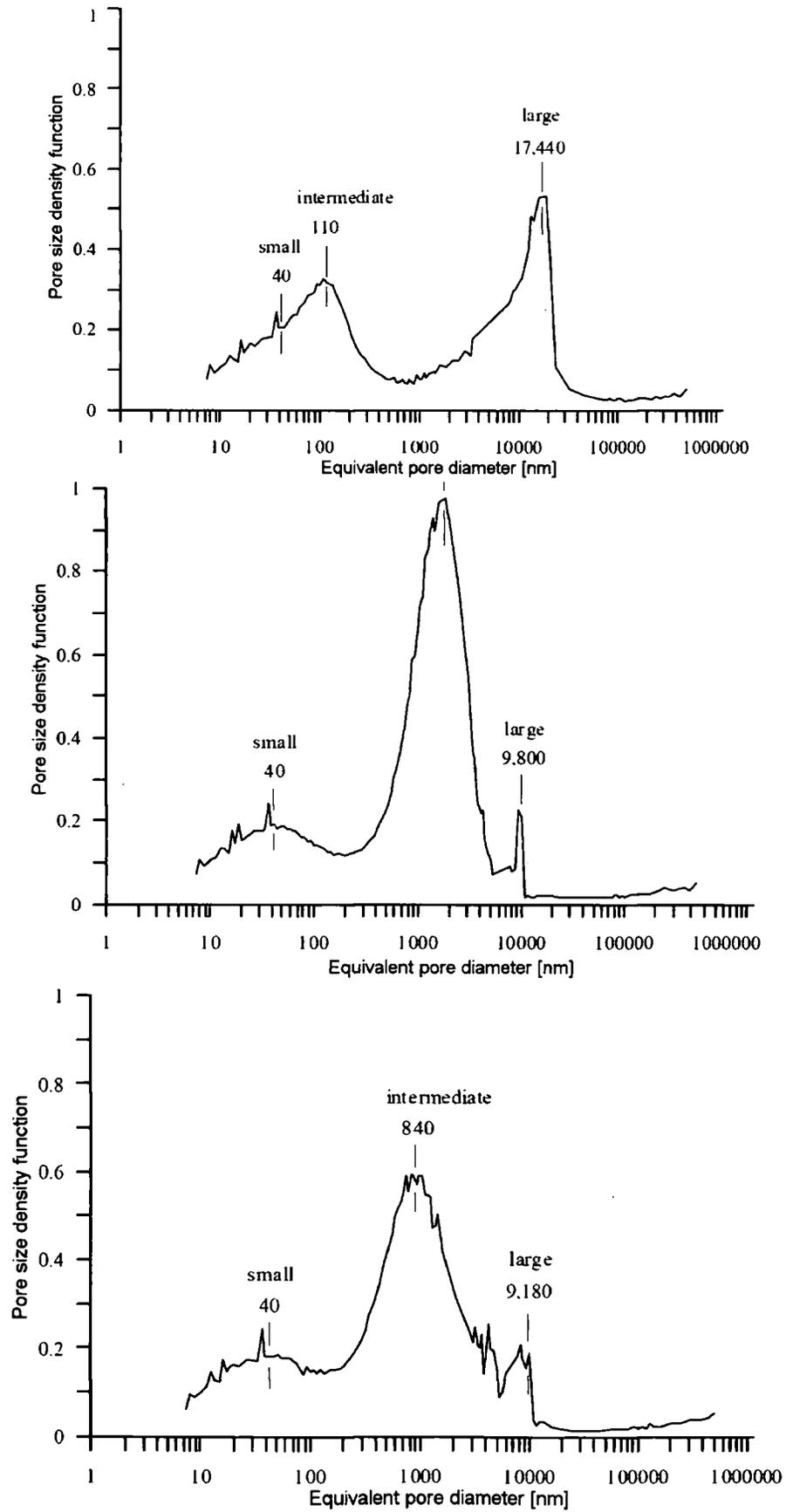
Figure 2.16. Fabric evolution during wetting: pore structure after compaction (top), after free swelling (middle) and after swelling under constant volume (bottom), after Monroy (2006).
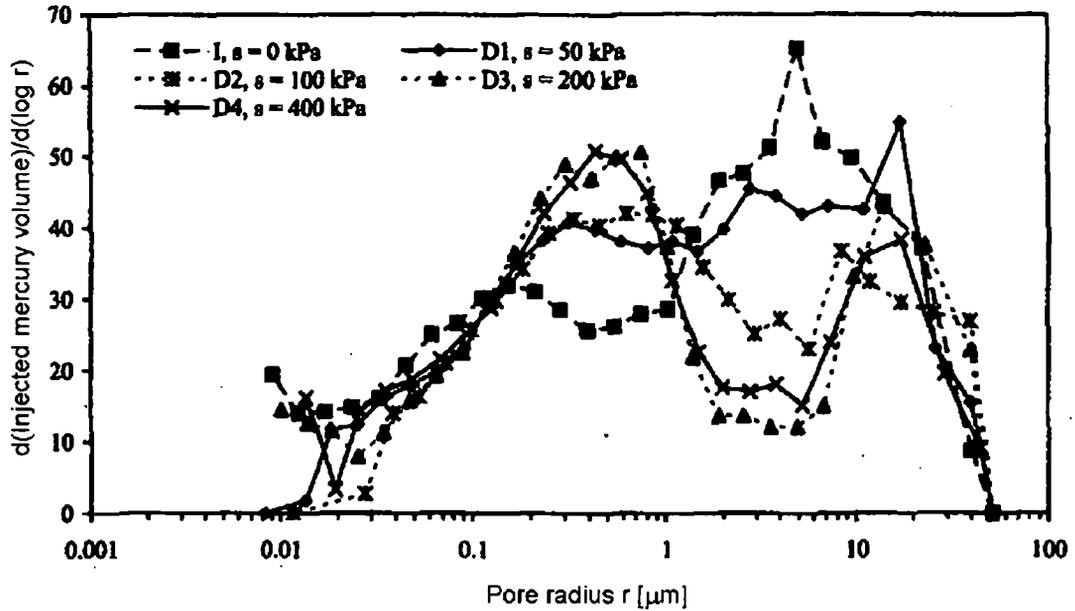
Figure 2.17. Fabric evolution during drying with suction increas from 0 up to 400 kPa (after Cuisinier and Laloui 2004).
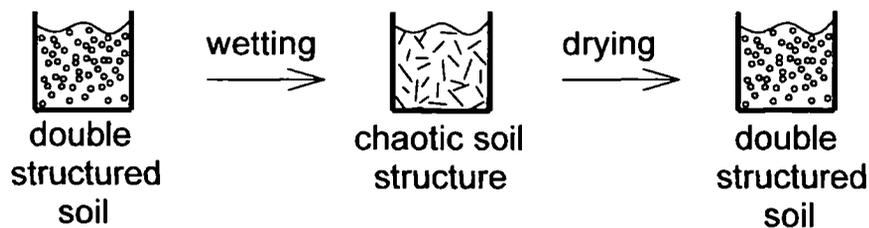
Figure 2.18. Recovery of double structure after wetting and drying

2.2.4. Interaction between soil microstructure and water retention behaviour

This is one of the least understood phenomena in unsaturated soils but it is area of interest not only of geotechnics but also agriculture (e.g. Stange and Horn 2005). The size of the largest pores influences the air entry value (AEV). The larger those pores are, the lower the AEV is. Using a Fisher equation (Fisher 1926) it is possible to calculate a theoretical value of suction for a given degree of saturation and given pore size distribution (e.g. Cui 1993). Unfortunately this approach is both laborious and inaccurate. Some other models exists, see e.g. Chan and Govindaraju (2004).

2.2.5. Possible way of creating a double porosity structure in natural soil

There are many uncertainties in the way the micro- and macrostructure interacts with each other. It is also not well explained how the double structure may be created in

45

natural unsaturated soils. Only some hypotheses of the double structure creation process can be given. One hypothesis suggests that the pore fluid in water had not always been chemically neutral and at some point it had caused aggregation (during similar process as one reported e.g. by Wang and Siu 2006a,b , Wang and Xu 2007 or Dolinar and Trauner 2007). Then, during each drying phase this aggregation has been recovered resulting in an aggregated soil (Fig. 2.19).
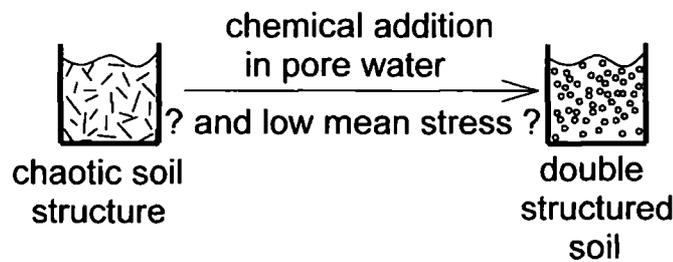
Figure 2.19. Creation of double structured soil due to chemical effects.

The other possibility is that the soil will naturally develop aggregation if it experiences enough cycles of wetting and drying. The process for an initially remoulded, fully saturated soil may be as follows. Upon drying, until reaching the Air Entry Value (AEV), the soil is uniformly compressed with additional stress equal to the suction value; hence there are no reasons for a double structure to emerge. However, after reaching the AEV, the wet regions in soil are compressed with the suction value whereas the just dried regions are not (the menisci water is neglected here). This should lead to double structure, as the dry regions (contrary to the wet regions), should not shrink. As it is confirmed that the soil shrinks little overall after reaching AEV, the pores between the wet and dry regions will become larger, resulting in the overall volume of pores being fairly constant. Thus, upon several cycles of wetting and drying a double structure will emerge (Fig. 2.20). However, this is a hypothesis that needs testing and scientific evaluation.
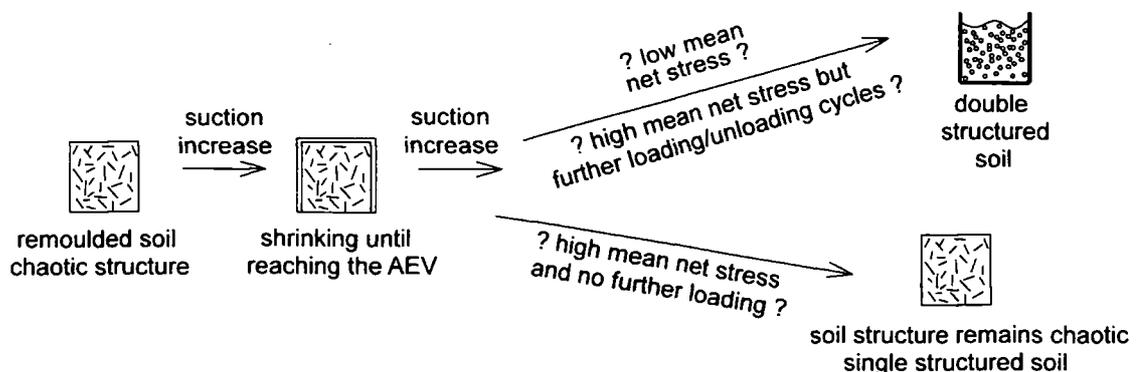
Figure 2.20. Hypothetical requirements for creation of double structured soil from remoulded state.

3. Microscale theory of unsaturated soils

This chapter considers those forces which appear on the microscopic level (that is mainly forces between aggregates, not the forces between clay platelets as described by diffuse double layer theory) and are a consequence of water presence in soil. The forces considered include surface tension and pore pressure.

One possible way to model behaviour of unsaturated soils is through a micro- to macro-approach. Once all the forces acting on soil particle in unsaturated soil are known and modelled, then the macroscopic stresses can be fairly easily derived. Currently, a not overly simplified solution of this problem remains unknown. However, some rough estimates of unsaturated soil behaviour are possible. It is unlikely that such estimates would properly predict all aspects of the soil behaviour, but they may be able to provide some insight into mechanisms present in unsaturated soil and enhance the understanding of this material.

Research on the microscale modelling of the unsaturated soils has been conducted for some time. The first results were obtained by Fisher (1926). Recently findings by Cho (2001), Cho and Santamarina (2001), Lu and Likos (2004), Likos and Lu (2004), Lu and Likos (2006) and Lechman and Lu (2008) increased the understanding of this area. One of more interesting result has been obtained by Lechman et al. (2006) who presented a solution of cyclic wetting and drying of a medium created from disk-shaped particles. They found that such a material does exhibit a hysteretic behaviour during cyclic drying and wetting and that this behaviour may be obtained using a thermodynamic free energy approach and thermodynamic energy stability concept. To obtain the hysteresis, no explicit involvement of contact angles and ink-bottle hysteresis was used. Lechman et al. (2006) additionally confirmed that the smaller the particle size is, the higher the capillary stress is and the higher the degree of saturation is when the hysteresis occurs.

3.1. Skeleton stress in menisci area of unsaturated soil

The forces resulting from a connection by water of the two equally sized spheres were assessed by Fisher (1926). This solution is briefly restated below. Having two speheres connected by menisci, the compressive force between the spheres is the sum of forces resulting from surface tension T and suction s (see Fig. 3.1 for definition of all the symbols). This force F, in case of equally sized grains is

$$F = \pi r_1 \left(s \cdot r_1 + 2T \right) \tag{3.1}$$

In this solution a simplifying assumptions of contact angle equal to zero and menisci radius being constant has been made.

The Laplace-Young law states that the additional pressure due to surface tension within the bubble of radii r_1 and r_2 is

$$\Delta p_{st} = T \left(\frac{1}{r_1} + \frac{1}{r_2} \right) \tag{3.2}$$

In the case shown on Fig. 3.1 the surface tension acting along the curvature of radius r_1 will cause increase of pressure, whereas the surface tension acting along the curvature of radius r_2 will decrease the pressure in the meniscus. As suction is taken positive when the pressure inside the meniscus is decreased, hence suction is

$$s = T \left(\frac{1}{r_2} - \frac{1}{r_1} \right) \tag{3.3}$$

Note that equations above can often be found written with double amount of surface tension (i.e. 2T) instead. Such an equation is a solution for an air filled bubble, where a bubble surface is in contact with air from two sides of the water film which doubles the amount of pressure inside (for a more detailed explanation see e.g. Mei 2004).

The approximate volume of a single meniscus can be computed as

$$V_m = \underbrace{\pi h_1 (r_1 + h_2)^2}_{\text{Volume of a cylinder}} - \underbrace{2 \cdot \frac{\pi}{6} \left(3(r_1 + h_2)^2 + \frac{h_1^2}{4} \right) \frac{h_1}{2}}_{\text{two volumes of 'cap' from soil grains}} - \underbrace{A_m \cdot 2\pi r_1}_{\text{Volume missing from the cylinder due to } r_2 \text{ radius}} \tag{3.4}$$

where the unknown r_1, r_2, h_1, h_2, A_m and θ are obtained from equations:

$r^2 + (r_1 + r_2)^2 = (r + r_2)^2$ (Pytaghoras theorem, triangle vertex is grain centre)

$r^2 = (r - 0.5h_1)^2 + (r_1 + h_2)^2$ (Pythagoras theorem, triangle vertex is the edge of meniscus)

$r_2^2 = 0.25h_1^2 + (r_2 - h_2)^2$ (Pythagoras theorem, triangle with hypotenuse r_2)

$A_m = \theta r_2^2 - \frac{h_1}{2}(r_2 - h_2)$ (the area of small circle segment less the area of triangle)

$\theta = \arcsin \frac{h_1}{2r_2}$

and equation (3.3) for a full solution for given suction value.
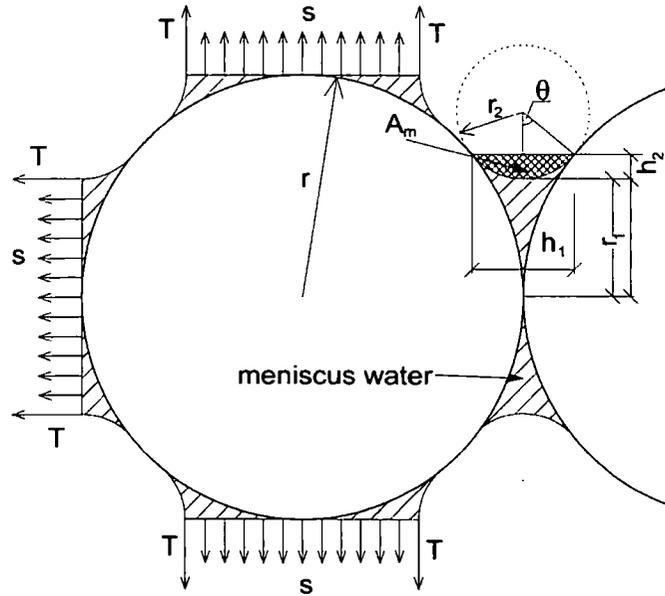
Figure 3.1. Forces acting on a soil grain in a simple cubic packing

The force determined using (3.1) and the volume using (3.4) has been used to create Figs 3.3 and 3.4. Similar solutions may be found in Lu and Likos (2004, 2006).

In equilibrium conditions menisci between soil grains that touch each other are always present, as the suction in meniscus may be arbitrary high. However, as suction increases, the radius r_1 reduces, thus the overall force is fairly constant (see Fig. 3.3). Nevertheless, generally speaking, the force between any two grains due to a meniscus is small. This can be balanced by the number of grains; the smaller the grains are, the more menisci are present in a unit volume. Thus the overall pressure may be significant. Assuming a simple cubic packing (a packing where each sphere is touching its 6 immediate neighbours, Fig. 3.2) the increase in stress is as presented in Fig. 3.3. and corresponding degree of saturation in Fig. 3.4. The mean net stress due to menisci is computed as

$$p_{men} = \frac{F}{4r^2}$$ (3.5)

and the degree of saturation S_r is equal to

$$S_r = \frac{V_{water}}{V_{water} + V_{air}} \overset{\text{simple cubic packing}}{\underset{\text{menisci region}}{=}} \frac{3V_m}{V - V_{grain}} = \frac{3V_m}{r^3(8 - 4/3\pi)}$$ (3.6)

and in the menisci part of soil is generally low or very low.

49
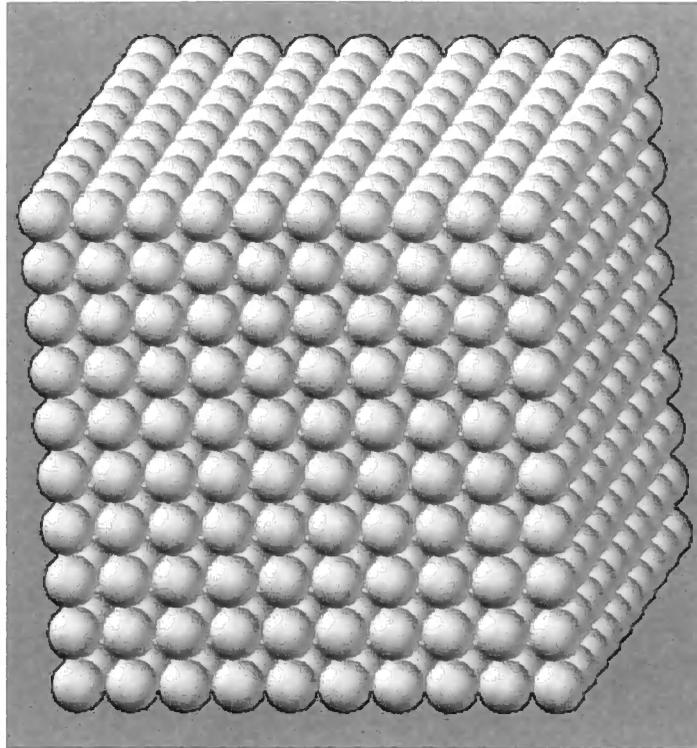
Figure 3.2. Simple cubic packing of aggregates
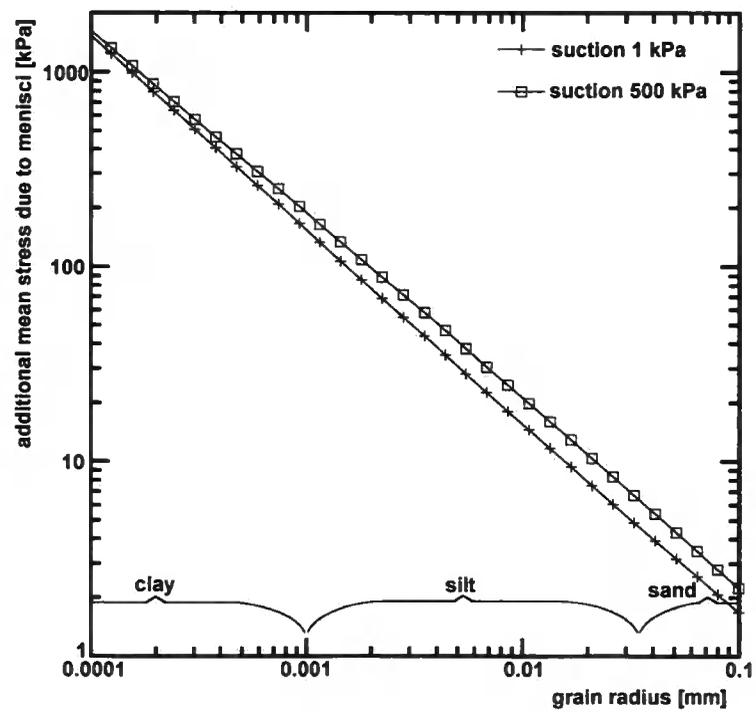
Figure 3.3. Mean net stress in menisci part of soil due to menisci forces. Simple cubic packing assumed

50
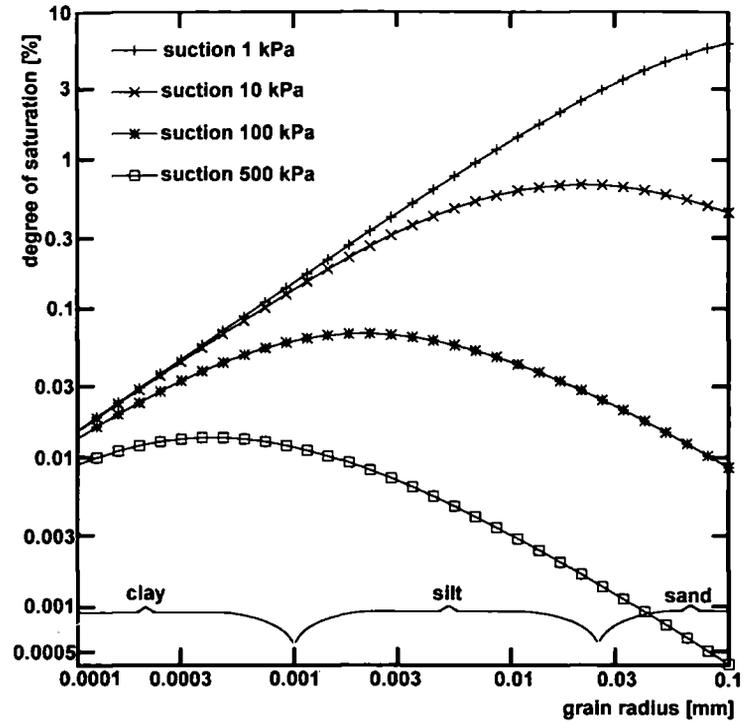
Figure 3.4. Degree of saturation due to menisci. Simple cubic packing assumed

The simple packing (Fig. 3.2) assumed in the results presented in Figs 3.3 and 3.4 is not a good approximation of a soil structure built from clay or silt particles. Such particles are instead gathered together creating aggregates. However, perhaps the aggregates may be assumed to be ordered in a simple cubic packing. Then, assuming an aggregate radius of $5\,\mu m$, the realistic additional mean net stress due to menisci is in range of tens of kPa and is fairly constant, largely independent of the suction value. Still, even for aggregates, Figs 3.3 and 3.4 give just an approximation of the forces present in real soil. Despite this, the additional stress due to menisci is likely to stay in the computed range independent of the actual packing structure of aggregates in soil. As unsaturated soils exhibit two regions (one with menisci and the one with bulk water), the following section will deal with the bulk water area.

3.2. Skeleton stress in bulk water region of unsaturated soil

The bulk water area of soil is the part of soil that is completely flooded with water. Those regions, combined with the regions where only menisci water is present cover the whole volume of soil. In the bulk water, the additional pressure on soil grains is equal to

51

the suction. Additionally, on the boundary of the bulk water region there are surface tension forces acting, increasing the overall stability of such regions.

3.2.1. Bulk water within aggregates

It is often assumed that the bulk water regions are restricted to those regions within the aggregates. Thus, the aggregates remain fully saturated, and connected by menisci, whereas the larger pores between aggregates are not filled with water. Hence the total mean stress within aggregates would be

$$
\underbrace{p_{agg}}_{} = \underbrace{p}_{\text{external mean net stress}} + \underbrace{s}_{\text{suction}} + \underbrace{p_{men}}_{\substack{\text{mean stress due to menisci} \\ \text{connecting the aggregates}}} + \underbrace{p_{st}}_{\substack{\text{mean stress due} \\ \text{to surface tension}}} \tag{3.7}
$$

where p_{men} is the mean stress due to menisci forces and p_{st} is the additional mean stress due to surface tension. The suction component is due to decrease in pore water pressure within the aggregate. It is difficult to exactly assess, how much influence on the stress have the last two components of the equation (3.7). The p_{men} can be approximated using equations from section 3.1. Assuming simple cubic packing of the aggregates and estimating aggregate radius to be $5\mu m$, the p_{men} is likely to be in the range of tens of kPa (as shown in Fig. 3.3). The component due to surface tension, p_{st} is directly influenced by the aggregate radius.
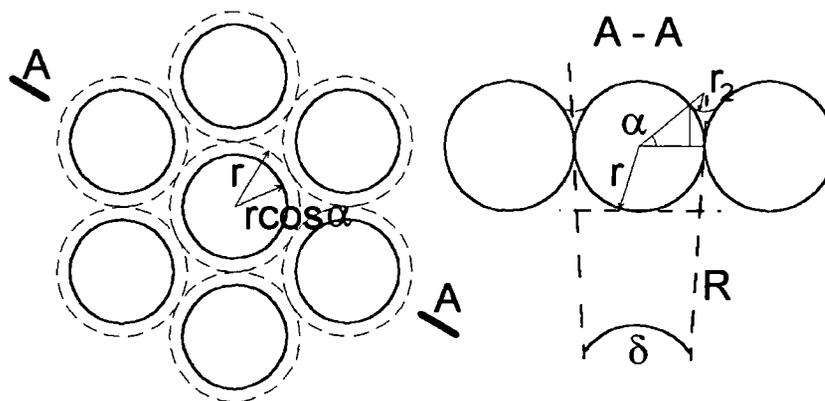
Figure 3.5. Fragment of surface and fragment of a cross-section of a spherical aggregate of radius R from Fig. 3.2 created from spherical grains of radius r.

Let's assume an idealised spherical aggregate of radius R created from spherical grains of radius r, where R>>r. An approximate hexagonal tessellation of the sphere surface of the aggregate (see Fig. 3.5.) is assumed such as that each soil grain on the surface

corresponds to one hexagon. Such a hexagon has the perimeter equal to $4\sqrt{3}r$ and area of $2\sqrt{3}r^2$. Along this perimeter are acting the surface tension forces which contribute to the p_{st} term. The radial component of the surface tension force is approximately equal to $T4\sqrt{3}r\sin\delta$ which may be further simplified as $T4\sqrt{3}\dfrac{r^2}{R}$. This leads to a stress value $p_{st} = \dfrac{2T}{R}$ as the mean stress is averaged over the whole area. Note that this stress component, partially because the simplified assumption used, is independent of suction but linearly dependent on the radius of aggregate. Assuming an aggregate radius of $5\mu m$ leads to additional mean stress

$$p_{st} = \frac{1000 \cdot 2 \cdot 0.073}{5} = 29.2 \text{kPa} \tag{3.8}$$

This simple solution is valid only for spherical aggregates built from spherical grains and thus is a gross simplification. Yet it gives valuable insight into the nature of forces within an unsaturated soil.

In the case of a higher degree of saturation, the bulk water areas become larger, as there is more water than can be accommodated by the swollen aggregates. In such cases the p_{men} and p_{st} stresses would likely become smaller than those calculated above.

Finally, it is possible to calculate an average stress in unsaturated soils. This stress is

$$p_{av} = p + (1 - \chi)p_{men} + \chi(p_{men} + p_{st} + s) \tag{3.9}$$

where χ is a parameter describing the relative volume of bulk water region. When it is assumed that all the water within soil is the bulk water (as the menisci degree of saturation is very small for majority of suctions, see Fig. 3.4) χ becomes equal to degree of saturation S_r. When additionally the stress due to menisci forces and the stress due to surface tension is disregarded, the average stress becomes

$$\sigma_{ij}^{av} = \sigma_{ij} + \delta_{ij}S_r s \tag{3.}$$

which is the form of stress, sometimes dubbed as the effective stress, given in (2.3). Such a stress measure has been used in some constitutive models, e.g. by Wheeler et al. (2003). However, to the best knowledge of the author, no constitutive model for unsaturated soils explicitly includes any stress correction corresponding to stresses due to menisci p_{men} and surface tension p_{st}.

4. Constitutive modelling of unsaturated soils

To model the macroscopic behaviour of unsaturated soils, the elastic and inelastic response due to mechanical loading and drying and wetting need to be addressed. Usually a separate constitutive model for water retention and mechanical behaviour is adopted. In such circumstances the mechanical model can be used with any model for water retention behaviour. Recently, as in the models of Wheeler et al. (2003) and Sheng et al. (2008), the model for water retention behaviour has become an integral part of the formulation describing the soil behaviour.

The most widely known constitutive model for unsaturated soil is that proposed by Alonso et al. (1990), commonly referred to as the Barcelona Basic Model (BBM). This model and its modification have the leading position in the field of unsaturated soil. However, there are numerous constitutive models for unsaturated soils that have different origins from the BBM. These include those proposed by Blatz and Graham (2003), Bolzon et al. (1996), Cui et al. (1995), Fredlund and Pham (2006), Gallipoli et al. (2003a), Georgiadis et al. (2005), Ghorbel and Leroueil (2006), Kohler and Hofstetter (2008), Loret and Khalili (2002), Mašin and Khalili (2008), Nuth and Laloui (2008) [see also Laloui et al. 2008], Rampino et al. (2000), Russel and Khalili (2006), Sheng (2003a, b), Sheng et al. (2008), Stropeit et al. (2008), Sun et al (2007a), Thu et al. (2007), Tamagnini (2004), Wheeler et al. (2003). The Barcelona Basic Model and the model by Wheeler et al. (2003) have been singled-out here to be described in greater detail below.

Many of the above-mentioned models are currently used only by the research group they were created in. This is usually due to their complexity: they require a significant time investment before one can properly assess the model quality and its fitness for any given problem. This is necessary, as some of the models do not appear to be substantially better in many practical cases than the BBM is spite of requiring more parameters. Other may seem to be able to model the behaviour of unsaturated soils well, but the number of parameters is prohibitive and thus their use is restricted to those engineering problems which must be solved as accurately as possible. The number of parameters is important, as to properly calibrate the model, more laboratory tests are required. Conducting those tests requires special equipment, can be costly and time-consuming. Because of this, the most complex problems are usually tackled by

specialised research groups such as the groups at UPC in Barcelona or at ENPC in Paris where a constitutive model is often enhanced to suit the specific problem requirements.

4.1. Barcelona Basic Model

The Barcelona Basic Model was first proposed by Alonso et al. in 1990. This model is now as the benchmark against which all the more recently proposed constitutive models are tested. The BBM is an extension of the Modified Cam Clay (MCC) model (Roscoe and Burland 1968) into the area of unsaturated soils. It operates in the triaxial stress space p-q where p is the net mean stress (total stress reduced by the value of air pressure) and q is the shear stress. Similar to the MCC, the model assumes linear relationships in void ratio e (or specific volume v) versus logarithm of mean net stress [e-ln(p)] space. Different stiffness (line slopes) for elastic states within yield locus and elasto-plastic loading are used, as in the MCC. However, in the BBM the slope of the elasto-plastic virgin compression line depends additionally on the current value of suction. The BBM uses the MCC constants: λ – slope of the virgin compression line in the log (p) – v graph, κ – slope of the elastic loading – unloading line in the log (p) – v plot, M – slope of the critical state line in the p – q space, G – shear modulus and N – specific volume for virgin compressed soil reached reference mean stress p^c. The additional constants required are κ_s – slope of the elastic loading – unloading line in the log (s) – v plot, k – parameter describing the increase in cohesion with suction at atmospheric pressure p_{atm}, r – parameter defining the maximum soil stiffness and β – parameter controlling the rate of increase of soil stiffness with suction. Finally, the MCC allows for the reference mean stress p^c to be taken as arbitrary, as long as the corresponding value of N is used, whereas in the BBM p^c is a unique mean stress value at which the yield locus size remains constant when the soil is dried or wetted.

4.1.1. Capabilities of the BBM

The BBM has been developed as an extension of the Modified Cam Clay (MCC) for partially saturated soils. It has been designed, similarly to the MCC, in a p-q space with suction being an additional parameter. The most important single feature of the BBM is probably its ability to model collapse (see section 2.1).

Barcelona Basic Model assumes that the yield locus expands when suction increases and contract when suction decreases. Thus, partially saturated soil behaves elastically until reaching higher mean net stress comparing to the fully saturated soil with the same

hardening parameter p_0^*. While the soil is wetted, the yield locus decreases its size and, if mean net stress is high enough, large plastic deformations occur leading to the simulation of collapse.

Apart from the model constants, the size of the BBM yield locus (Fig. 4.1) is determined by the preconsolidation stress for saturated conditions p_0^* and suction. The yield function equation is

$$F = q^2 - M^2(p + ks)(p_0 - p) = q^2 - M^2(p + ks)\left(p^c \left[\frac{p_0^*}{p^c} \right]^{\frac{\lambda(0)-\kappa}{\lambda(0)\left((1-r)e^{-\beta s}+r\right)-\kappa}} - p \right) = 0 \qquad (4.1)$$

Although, the shape of the yield locus is the same as in the MCC – an ellipse, equation (4.1) shows that during an increase in suction, the yield locus not only changes its size, but also its centre moves. Thus the BBM belongs to the family of models that exhibit both isotropic and kinematic hardening. The shift of the yield locus is governed by the value of k – parameter describing the increase in cohesion with suction at atmospheric pressure.
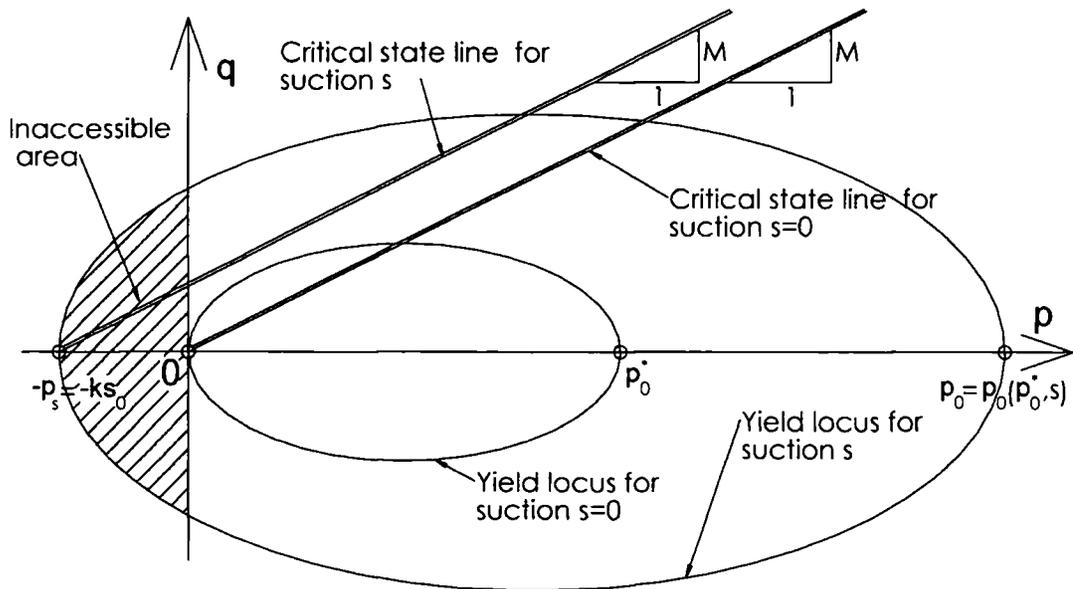
Figure 4.1. BBM yield locus. Note that the part of the yield locus left to the shear stress q axis is not accessible.

It is generally perceived that an elliptic yield locus, does not predict the shear behaviour of soil very well (compare Fig. 2.13). Unfortunately such an elliptic yield locus has been assumed in the BBM, similarly to the MCC. Thus, probably in an attempt to

increase the accuracy of the model predictions on paths that include shearing, a non-associated flow rule and a shift in the yield locus due to suction has been introduced. The flow rules in the BBM are:

$$d\varepsilon_v^p = \Lambda \cdot \left(M^2(2p + ks - p_0)\right)$$

(4.2)

$$d\varepsilon_s^p = \Lambda \cdot 2q \frac{M(M-9)(M-3)}{9(6-M)} \frac{1}{1 - \frac{\kappa}{\lambda(0)}}$$

(4.3)

where Λ is a non-negative scalar plastic multiplier. This non-associated flow rule has been chosen such that on an oedometric stress path where the horizontal stresses are calculated using Jaky's equation, the lateral strains are equal to zero. However, due to some decrease in numerical stability and theoretical considerations regarding thermodynamical correctness of using a non-associated flow rule, the BBM is sometimes used with an associated flow rule. In such case the plastic shear strain is

$$d\varepsilon_s^p = \Lambda \cdot 2q$$

(4.4)

The shift of the yield locus also describes the increase of strength of soil at zero mean stress – i.e. dry soil has some capabilities for bearing the tensile stress. Unfortunately, due to using linear relationship between void ratio and logarithm of mean net stress, the mean net stress must stay positive. Thus, the shift in the yield locus leads only to different yield locus size and shape, while the part of the ellipse corresponding to the negative mean net stress may as well not exist (see Fig. 4.1).

The original formulation of the BBM, makes use of an additional yield locus corresponding to the highest suction value experienced in soil history. Thus, when the suction is below the value of the highest suction experienced by soil, the volume changes due to suction should be elastic (plus a possible additional plastic change due to the existing stress state as a consequence of the decrease of the yield locus size during wetting). When suction reaches its maximum historical value, on further increasing of the suction, the deformations becomes elasto-plastic and the suction yield locus expands. This feature of the BBM is most often dropped and usually the implementation of the BBM in FE codes does not allow for the suction yield locus. The usual reasons for omitting the suction yield locus are the increase of algorithmic complexity and theoretical difficulties in calibration – most unsaturated soils experienced a very high suction value in its lifetime meaning that the suction yield locus should not be reached

(the latter is also true for most of laboratory experiments during which the soil dried completely before wetting it to the value of suction required for the experiment).

A stress path illustrating the capabilities of the BBM is presented on Figure 4.2. In this diagram it is initially assumed that the soil is (i) fully saturated, (ii) in a isotropic stress state and that (iii) it has never in history been loaded over the value of p^c (point A). At that point the mean net stress is increased until reaching point B. Over the A–B path, the predicted soil behaviour is the same as that given by the Modified Cam Clay. At B the soil is dried and suction increases from zero to s_0. During drying the soil shrinks and reaches point C. Note that the amount of shrinkage is independent of the stress state the soil experiences at the moment of drying. At C the mean net stress is increased again. The BBM predicts an elastic behaviour until F. At point F the soil will start behaving elasto-plastically once more.

Point F may be reached as a result of following other stress paths. For example, if the soil is at A until suction reaches s_0 and then loaded, the loading would be elasto-plastic from the very beginning and would follow the virgin compression line G–F with the slope of $\lambda(s_0)$, finally reaching the same point F.

Figure 4.2. Behaviour of soil on isotropic stress paths, as predicted by the BBM.

In the situation where the sample is wetted, the yield locus will decrease in size that may result in collapse. Generally collapse will occur, when the specific volume (or mean net stress) is large enough when soil is wetted. Then, after a hypothetical expansion of the sample due to decrease in suction, the specific volume would lie above the virgin compression line corresponding to the reduced suction. Such a high specific volume is not permitted and will be corrected to the value lying on the virgin compression line corresponding to the reduced suction, resulting in collapse. If we wet the sample while the state lies on the virgin compression line corresponding to given value of suction (e.g. at point E), collapse will occur independent on the amount of wetting (but the amount of collapse will be dependent on the suction decrease). After reducing the suction to zero, the specific volume will reach that state on the virgin compression line corresponding to zero suction, matching the current mean stress (point E_1). If we wet the soil while being in the elastic region (e.g. at point D), the soil will initially expand, until reaching the virgin compression line for reduced suction (point D_1), and then collapse, finally reaching point D_2 on the virgin compression line for fully saturated soil. Finally, if the soil is wetted while being substantially unloaded (i.e. left from the point C in the Fig. 4.2), the soil will only elastically expand, but no collapse will be observed.

4.1.2. Evaluation of Barcelona Basic Model

The Barcelona Basic Model, albeit because of its similarity to the popular Modified Cam Clay Model is fairly easy to understand, has several shortcomings that hinder its application in both engineering and research analyses.

From a theoretical point of view the BBM inherited most of the flaws of the MCC model. Note that the MCC model has been described as a 'pedagogic model' (Muir Wood 1990) and as such should not be considered as a model suitable for the prediction of advanced soil behaviour (at least without some extensions). The well known weaknesses of the MCC lie mainly in the prediction of soil response under shear loading and lack of proper modelling of the elastic behaviour, especially under cyclic loading.

The shear behaviour has been corrected by use of the non-associated flow rule. However, this correction relies on Jaky's solution of the K_0 line, which is a rather crude approximation. Thus, the effects of shear are often not substantially better predicted than in the case of the MCC.

Some of the problems in the model are due to the way the unsaturated state behaviour is predicted. Wheeler et al. (2002) points out that assumption of no change in the size of yield locus due to suction value at reference stress p^c is "unlikely to be true in practice". Indeed, such an assumption has little theoretical justification – a suggestion that at some external net stress p^c the suction becomes irrelevant to soil behaviour finds little justification both in laboratory testing and from theoretical standpoint.

In the same paper Wheeler et al. (2002) points out that the load-collapse (LC) curve, corresponding to the increase of yield locus size due to suction for some selection of BBM parameters, is non-convex. The issue of non-convexity raises problems in the numerical implementation of the BBM, as the usual assumption taken is that the yield locus, constructed in the mean net stress – shear stress – suction (p–q–s) space, is convex.

Another weakness of the BBM stems from the fact that it only macroscopically describes unsaturated soil. However, depending on the microstructure of soil (the pore sizes distribution) the unsaturated soil may behave quite differently. Thus, the BBM is not likely to predict correctly the behaviour of soil that involves multiple wetting and drying cycles, as during such cycles (especially full wetting) the distribution of soil pore sizes is likely to be affected. Similarly, several cycles of loading and unloading in the elastic region of the yield locus will have some effect on the soil pore structure. Effectively, cyclic loading (even with low number of cycles), both due to changes in stress state and wetting and drying of soil, changes the soil fabric thus the soil is likely to behave in other way than before. Evidence of such behaviour is given e.g. by Day (1994), Barrera (2002), Jafari and Shafiee (2004), Hong et al (2006) and Ferber et al. (2006). Changes in suction alone lead to change in the microstructure of the soil fabric too. Such changes in structure are possible even at constant void ratio (e.g. Cuisinier and Laloui 2004).

Finally, the BBM assumes a linear relationship between the natural logarithm of mean net stress p and void ratio e. This relationship is inappropriate both in the region of low and very high stresses. At high stresses the soil behaviour may be better described by a line in a ln(p) – ln(e) space (as in the formulation of the BBM the void ratio can become negative which is obviously wrong). Such a relationship (proposed by Butterfield 1979) is also easier to justify in a thermodynamical framework (see e.g. Houlsby 1981). On the other hand, at low stresses it would be advisable to allow for a small amount of tension before failure of a soil with high suction, as it is confirmed by laboratory tests.

Note, however, that the BBM (used with properly calibrated parameters) predictions generally stay on the safe side in both regions, overestimating the deformations both in high and low stress ranges. The other reason why the BBM does not allow for modelling the soil over the full range of stresses may be that the slope of the virgin compression lines corresponding to a given suction is constant whereas the laboratory evidence suggests that it is changing depending on the value of mean net stress (compare Fig. 2.4).

In engineering practice the BBM has not been used too often, though probably more than any other constitutive model for unsaturated soils. This is likely to be due to a combination of factors such as: (i) the BBM seems to be significantly more complex than the commonly used constitutive models, (ii) the amount of time and tests (and thus cost) required for calibration of the model constants is high, (iii) the BBM is rarely a part of commercially available Finite Element codes (probably only implemented in CODE_BRIGHT) and (iv) there is a relative lack of expertise available, associated with unsaturated soils in general and the BBM in particular. As a result only few practical analyses have been performed up to date. Those were mostly performed by universities who have resources and expertise to introduce the BBM into their own Finite Element codes.

To sum up, the use of the BBM is currently constrained to fairly special cases where a more advanced analysis is required. Such analysis is usually performed by specialised university research groups. However, as it has been pointed out, sometimes the BBM does not offer the quality of prediction required for a very advanced analysis. This will be shown below on example of choosing the model constants to the data provided by Barrera (2002). This fitting was performed as part of the MUSE research program.

4.1.3. Parameter estimation for BBM

The determination of the BBM constants using a given set of laboratory data is a difficult task. Such a task was one of the benchmark activities within MUSE research training network. All the participants received the same set of laboratory data and their task was to choose the BBM material parameters that provided the best-fit to the data.

The experimental data provided by Barrera (2002) were chosen for this purpose. For the parameter estimation, only those data from tests performed in a high quality triaxial cell were considered. These comprised: oedometric test EDO-1, saturated isotropic test SAT-1, triaxial isotropic test with controlled suction TISO-1 (see Fig. 2.6) and triaxial

tests involving shearing: IS-OC-03, IS-NC-06, IS-NC-12, IS-OC-06, IWS-OC-01 and IWS-NC-02. For details of the tests see Barrera (2002) or D'Onza et al. (2007).

Several approaches for parameter estimation are possible however they can lead to significantly different values of parameters (see D'Onza et al. 2007). The approach adopted was to estimate all the saturated material constants, i.e. $\lambda(0)$, κ, $N(0)$, and the initial value of the hardening parameter p_0^* from the saturated test SAT-1 (Fig. 4.3 left). Subsequently the value of elastic stiffness parameter for changes in suction, κ_s, was computed based on test TISO-1 under assumption that the atmospheric pressure p_{atm} is equal to 100 kPa.

The values of the unsaturated material constants r, β and p^c were obtained based on the unsaturated triaxial tests. The value of reference stress p^c was estimated based on the slope of unsaturated virgin compression lines $\lambda(s)$. This was done for the IS-NC-12 and IS-OC-06 tests (see Barrera 2002, D'Onza et al. 2007) where initial loading is isotropic, suction is constant and both elastic and elasto-plastic deformations are present. Thus, the preconsolidation (yield) stress p_0 can be estimated from the graph. This stress corresponds to the previously obtained hardening parameter p_0^*. As $\lambda(0)$ and κ values are already known, the value of the reference stress p^c can be calculated as

$$p^c = \left(\frac{\left(p_0^* \right)^{\frac{\lambda(0)-\kappa}{\lambda(s)-\kappa}}}{p_0} \right)^{\frac{\lambda(s)-\kappa}{\lambda(0)-\lambda(s)}} \tag{4.5}$$

A rounded average value from the two estimates corresponding to IS-NC-12 and IS-OC-06 tests was taken as the final value of the reference stress p^c.

In tests TISO-1 (Fig. 2.6), IWS-OC-01 and IWS-OC-02, collapsible behaviour of soil is observed. After collapse, the value of p_0 is known (this is the value of current mean net stress). As the specific volume of soil is also known, one can calculate the corresponding value of hardening parameter p_0^* using

$$v = N(0) - \lambda(0)\ln\frac{p_0^*}{p^c} - \kappa_s \ln\frac{s + p_{at}}{p_{at}} - \kappa\ln\frac{p_0}{p_0^*} \tag{4.6}$$

Then, for tests TISO-1, IWS-OC-01 and IWS-OC-02 the value of $\lambda(s)$, corresponding to suction in soil after collapse may be determined using (4.5). Additional values of $\lambda(s)$ that may be used are those from tests IS-NC-12 and IS-OC-06. Having calculated

λ(s) for a given value of suction, it is possible to fit the parameters r and β using e.g. the least squares method from

$$\lambda(s) = \lambda(0)\left((1 - r)e^{-\beta s} + r\right) \qquad (4.7)$$

The critical state line slope M, the parameter describing the increase in cohesion with suction k and shear modulus G were estimated based on data from tests IS-OC-03, IS-NC-06, IS-NC-12, IS-OC-06 IWS-OC-01 and IWS-NC-02 (for the tests details see Barrera 2002 or D'Onza et al 2007). In those tests the specific volume corresponding to the critical state was identified. Then, as suction is known, the values of the hardening parameter p_0^* and preconsolidation pressure p_0 corresponding to this specific volume can be computed. The mean net stress p^{crit} and the shear stress q^{crit} corresponding to the stress in the critical state are

$$p^{crit} = 0.5(ks + p_0) \qquad (4.8)$$

$$q^{crit} = 0.5M(ks + p_0) \qquad (4.9)$$

, which allows for calculation of M and k.

The final set of parameters estimated by Solowski and Toll is given in Table 4.1. Selection of BBM prediction with these initial parameters compared with the experimental data is given in Figures 4.3 and 4.4. Note that a set of parameters that approximate a single given test is not so difficult to find, however, a set of BBM material constants that give a close approximation to all the laboratory tests may not exist.

The usual way of plotting the comparison of model prediction against experimental data is to use the model as being stress driven, where strains are predicted. Another possibility exists, i.e. instead of stresses one can prescribe strains and find the stress response of the model. If the laboratory data were ideally matched, then the predictions will agree (a situation close to this is shown in Fig. 4.3 left, where the saturated test is simulated). However in the case where model response only approximates the laboratory data, the difference can be significant (Fig. 4.3 right).

When the parameters have been estimated by initially fitting the response of the soil under isotropic stress conditions, then the oedometric and shear tests are predicted poorly (as in Fig. 4.4). Yet, when an emphasis is put on first fitting the unsaturated tests, then prediction of the saturated test was even worse. Thus it is possible to fix the

model constants so that the error in the unsaturated isotropic test (Fig. 4.3. right) is minimised, but the saturated test simulation then becomes unsatisfactory. An intermediate choice of the parameters values is also possible. This observation was also revealed by other MUSE members who undertook the same exercise. It appears that the general procedure followed was usually similar to the ones described above. This led to saturated material constants being similar to the one described. Also the values of M and k were very similar for all the groups. However, the choice of initial hardening parameter and the unsaturated parameters varied significantly across different research groups (d'Onza et al 2008). Thus the predictions of a hypothetical new test based on parameters estimated by different research groups were rather inconsistent.

Despite the limitations described above, the BBM still remains the most popular model for unsaturated soils, perhaps because it strives for a balance between complexity and capability of prediction in practical engineering problems.

Table 4.1. BBM material constants for data by Barrera (2002)

Parameter description	Value
G – shear modulus	150 MPa
κ – elastic stiffness parameter for changes in mean net stress	0.012
λ (0) – stiffness parameter for changes in mean net stress for virgin states of the soil with suction s=0	0.074
M – critical state line slope	1.14
p_c – reference stress	0.5 kPa
N(0) – specific volume at zero suction for mean net stress equal to reference stress p_c	2
p_{atm} – atmospheric pressure	100 kPa
κ_s – elastic stiffness parameter for changes in suction	0.001
k – parameter describing the increase in cohesion with suction	0.46
β – parameter defining the maximum increase of soil stiffness with suction	0.125 kPa^{-1}
r – parameter defining the maximum soil stiffness	0.8
p_0^* – initial value of hardening parameter	85 kPa
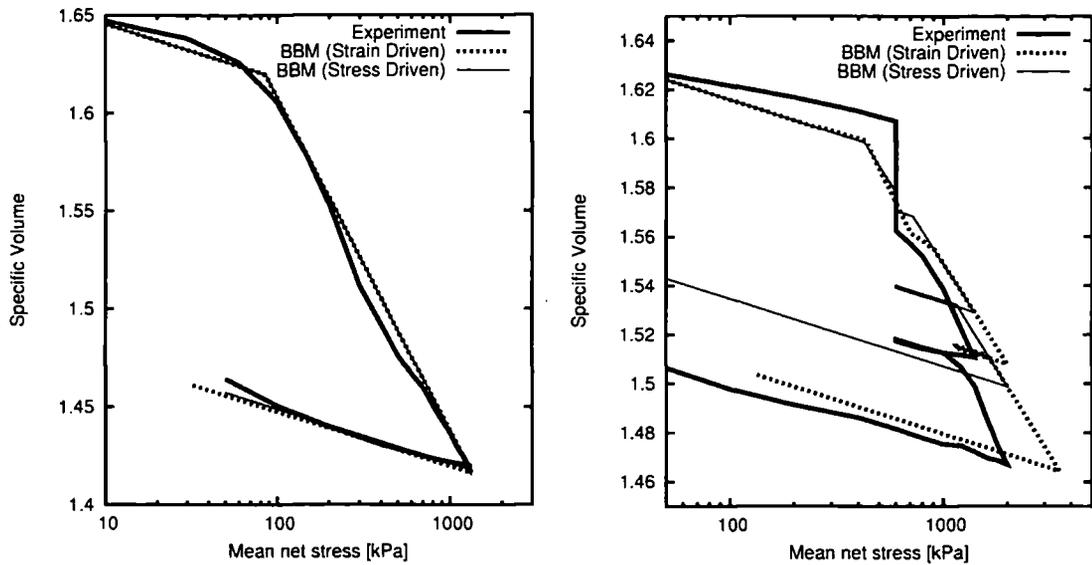
Figure 4.3. Comparison for the saturated SAT-1 (left) and unsaturated TISO-1 (right) isotropic tests. In the figure laboratory data and predictions of the BBM (both strain and stress driven) are given.
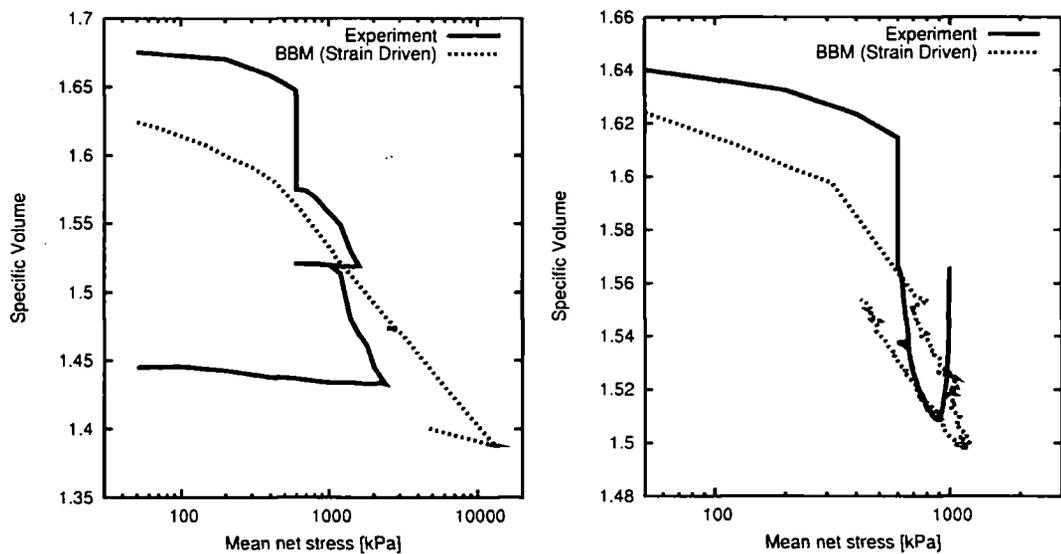
Figure 4.4. Simulation of an oedometric test EDO-1 (left), and shear test IWS-NC-02 (right). Only strain driven simulation is presented.

4.1.4. Common modifications to the BBM

A number of extensions to the Barcelona Basic Model exists. As mentioned before, the most usual and quite universally accepted modification is to dismiss the suction increase SI yield locus and treat all suction increments as purely elastic. Often the shear modulus G is taken not constant, as in Alonso et al (1990); the value of Poisson ratio is set

constant instead. Such an approach has been used e.g. by Gallipoli (2000) and in benchmark C5 of the MUSE project (Vaunat 2007).

Additionally, in the benchmark C5 (Vaunat 2007) it has been proposed that the bulk modulus K is given by $K = \dfrac{p}{\kappa}$ instead of $K = \dfrac{p \cdot v}{\kappa}$, including specific volume, as in Alonso et al. (1990). This modification effectively lead to a model in which the elastic behaviour is linear in the log (specific volume) – log (mean net stress) place, as compared to specific volume – log (mean net stress) plane proposed by Alonso et al. (1990).

The changes described above are amongst the most common. Other modifications are possible and lead to constitutive models for soil that closely follow the BBM. Currently the BBM model is being extended under guidance of its authors in the research group at the UPC resulting in double structure formulations. Such models are given e.g. by Alonso et al. (1999) and Sánchez et al. (2005).

The model of Sánchez et al. (2005) is placed within the framework proposed by Gens and Alonso (1992) and then Alonso et al. (1999). Sánchez et al. (2005) double structure model is based on the assumption that two levels of material structure should be considered, being related to the micro- and the macrostructure of soil. It is further assumed that the inelastic behaviour associated with hydraulic loading is a result of interaction between the two structural levels (the micro- and the macrostructure of the soil). The macrostructure is modelled with the Barcelona Basic Model (Alonso et al. 1990), which has been enhanced to deal with the additional effects of temperature change. The microstructure behaviour is treated as being fully reversible and isotropic (no preferential orientation of microstructure is present). The interaction between micro- and macrostructure is fairly simple and achieved by interaction functions. The two interaction functions correspond to microstructural contraction and microstructural swelling. The function values depend on the ratio between mean net stress and preconsolidation stress. The interaction functions bind the strain increments in microstructure to the plastic strain increments of macrostructure. Thus the total macroscopic plastic strain is a sum of the plastic strain arising from microstructural reversible strain and the plastic strain computed from the BBM. It seems that such double structure models are able to predict the behaviour of unsaturated soils quite well. However, they are more complex and more difficult to calibrate than the models proposed by Alonso et al. (1990) or Wheeler et al. (2003).

4.2. Models for water retention behaviour

As mentioned in the introduction, many models, including the BBM, operate in the mean net stress – suction space. Such models need coupling with a water retention model in order to be implemented into a Finite Element code, as the suction is not known and cannot be calculated. The FE deals with general laws for water flow and thus are able to predict the amount of water in given finite element. Then, using a water retention model, the suction in the element can be computed, which is required by the constitutive model for unsaturated soil. Not surprisingly, there are many models describing the water retention behaviour of soils.

4.2.1. Van Genuchten Model

One of the most popular approaches to describe the water retention behaviour is the van Genuchten model (1980). This requires at least three parameters to calibrate. It does not allow either for (i) modelling the difference between wetting and drying paths of the water retention behaviour or (ii) the difference in the water retention curves due to mechanical stress state and soil history. Nevertheless, with this model a good fit of the laboratory data for the great majority of soils is possible. It is also relatively simple to calibrate (this issue was addressed by van Genuchten 1980). Additionally, due to popularity and longevity of the model a considerable body of experience for its calibration exists. Because of these advantages, the van Genuchten (1980) model for water retention behaviour is the benchmark in the field and one of the most popular models currently used for the relationship between the suction and degree of saturation (Imre et al. 2006).

The lack of advance features (like ability to model the difference between wetting and drying paths) of the van Genuchten model is probably, maybe surprisingly, one of its strengths. It is rare that the difference between wetting and drying paths (and the difference in the water retention due to mechanical load) is important in engineering analyses. If it is important then an expensive testing program is required, which makes the more advanced models less commonly used in practical engineering.

Van Genuchten (1980) equation of the water retention curve is

$$w = w_r + \frac{w_s - w_r}{\left(1 + \left(\frac{s}{a}\right)^n\right)^m} \tag{4.10}$$

67

where a, n and m are model constants, w_r is the residual volumetric water content of the fully dried sample and w_s is the volumetric water content at full saturation. The equation may be rewritten differently as

$$S_r = \frac{1}{\left(1+\left(\frac{s}{a}\right)^n\right)^m}$$

(4.11)

, where it was assumed that the residual volumetric water content w_r is equal to zero, or, in other words, that at degree of saturation equal to one and zero the suction is zero and infinite, respectively. A model for the water retention curve offering comparable accuracy and used in similar problems is that of Fredlund and Xing (1994) which has the following equation

$$w = w_r + \frac{w_s - w_r}{\left(\ln\left[e+\left(\frac{s}{a}\right)^n\right]\right)^m}$$

(4.12)

This may be simplified, using the same assumption as above, to

$$S_r = \frac{1}{\left(\ln\left[e+\left(\frac{s}{a}\right)^n\right]\right)^m}$$

(4.13)

Recently a constitutive model for water retention behaviour has been given by Pham and Fredlund (2008). The authors claim that their model allows for modelling of water retention curve accurately across the whole range of water contents. The model parameters have a clear graphical interpretation thus a graphical calibration of the model is possible. However, the equation used is, unfortunately, rather complex. Because of this the authors proposed also a simplified expression where not all the parameters have such a transparent graphical interpretation. It is unclear whether the simplified model has advantages over the van Genuchten model.

4.2.2. Model of Gallipoli et al. (2003)

One of the problems with the van Genuchten (1980) model (and similar formulations) is that its parameters are independent from soil history. The model of Gallipoli et al. 2003) modifies the van Genuchten model so that some influence of the soil history (given in

68

the form of the void ratio) on the water retention behaviour appears. This influence is obtained by choosing the 'a' parameter of the van Genuchten (1980) model as

$$a = \frac{1}{\phi(v-1)^{\psi}}$$ (4.14)

resulting in an equation for the degree of saturation

$$S_r = \frac{1}{\left(1 + \left[\phi(v-1)^{\psi} s\right]^n\right)^m}$$ (4.15)

with parameters ϕ and ψ instead of van Genuchten's parameter 'a'. Such a choice of function has been justified by Gallipoli et al. (2003) by showing a good fit to experimental data. Unfortunately the new parameters do not have any clear physical meaning. Gallipoli et al. (2003) do not suggest, however, any simple method of choosing the parameters. In the calculated examples shown in the paper the model constants were chosen according to a least squares fitting procedure.

4.2.3. Model by Marinho (2005)

Marinho (1994) suggested that the soil water retention curve is unique during drying and wetting when normalised with respect to suction capacity C, defined as $\delta w / \delta \log s$. This concept has been expanded in Marinho (2005, 2006) where an algorithm to approximately construct the water retention curve has been given. The accuracy of prediction is not very high, but it is likely to be adequate in engineering practice. The strongest point of this model is that to obtain the water retention behaviour it is only necessary to know (i) the Atterberg limits for the soil, (ii) one value of suction at a known water content. Then tables given by Marinho (2005) allow for estimation of water retention curve. It is clear that if this method proves to be accurate enough for wide range of soils, then it should be highly successful in engineering practice. The only difficulty lies in having the one suction value at a given water content. This suction value can be obtained immediately if a tensiometer is available or in around a week time when the filter paper technique is used. The former is useful when time is pressing, which is usually the case in most engineering applications. If, on the other hand, the suction needs to be measured using filter paper, this test can be performed even in the most basic of soil mechanics laboratories which might have no specialised equipment

69

for unsaturated soils. The latter allows introduction of the unsaturated soil mechanics into everyday practice.

4.2.4. Other models describing water retention behaviour

The above models for water retention behaviour are all relatively simple. Sometimes it is required to obtain the solutions which are very accurate and thus the modelling of the water retention behaviour must properly include the hysteretic effects and scanning curves (compare Fig. 2.8). Such models are generally more complex and their application has been limited to relatively few cases. A review of hysteresis models for water retention curves is given in Pham et al. (2005).

4.3. Wheeler et al. model (2003) – framework and general description

The next generations of constitutive models for unsaturated soils do not only model the mechanical, but also the water retention behaviour of soil. An example of such model is that proposed by Wheeler et al. (2003). Other models of this type exist, for example Sheng et al. (2008).

The model described by Wheeler et al. (2003) introduces the stress measure named average skeleton stress (σ_{ij}^{*}). This stress is defined as a sum of the net stress (the difference between total stress and air pressure, as in BBM) and the product of the suction and degree of saturation:

$$\sigma_{ij}^{*} = \sigma_{ij} - \chi s = \sigma_{ij} - S_r s \delta_{ij} = \sigma_{ij} - [S_r u_w + (1 - S_r) u_a] \delta_{ij} \tag{4.16}$$

Such stress variables correspond to the stress variable suggested by Houlsby (1997) and Bishop stress (1959) taken with the value of weighting factor χ equal to the degree of saturation S_r. This form of a stress variable has been used beforehand e.g. in the Bolzon et al. (1996) model. The Wheeler et al. (2003) model employs also a modified suction s^{*} variable which is suction multiplied by the value of porosity n ($s^{*} = ns$). This measure of suction was suggested by Houlsby (1997). As mentioned previously a water retention curve is incorporated which may be regarded as an advantage over the BBM.

The Wheeler et al. (2003) constitutive model has been proposed for isotropic stress states only. Its material constants are parameters are: λ, κ, λ_s, κ_s, k_1, k_2, and

hardening parameters are: p_0^*, s_I^*, s_D^*. It also requires a value of the specific volume for the initial conditions.

The stress hardening parameter p_0^* defines the maximum skeleton stress experienced by the soil. The suction hardening parameters, s_I^* and s_D^* define upper and lower bounds for plastic suction increment. Suction increments between s_I^* and s_D^* are elastic.

λ and κ parameters have similar meaning as in the MCC, however instead of the mean net stress, the mean skeleton stress in used. λ_s and κ_s describe the water retention curve in the degree of saturation – log (modified suction) space. The plastic lines have a slope of λ_s and the elastic lines have a slope of κ_s. The model yield locus and water retention description is given in Fig. 4.2.1. Finally, the parameters k_1 and k_2 describe coupling between the mean stress and suction yield loci.
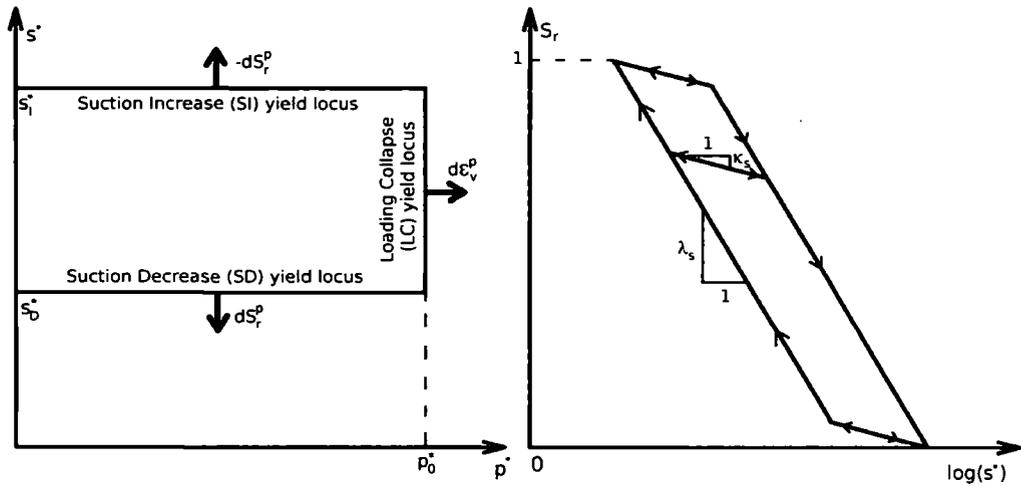
Figure 4.5. Yield locus and water retention behaviour of the Wheeler et al. (2003) model.

The relationship between hardening parameters, plastic volumetric strain increment and plastic change of degree of saturation are given as

$$d\varepsilon_v^{pl} = \frac{(\lambda - \kappa)}{v(1 - k_1 k_2)} \left(\frac{dp_0^*}{p_0^*} - k_1 \frac{ds_D^*}{s_D^*} \right) \qquad (4.17)$$

$$dS_r^{pl} = \frac{-(\lambda_s - \kappa_s)}{v(1 - k_1 k_2)} \left(\frac{ds_D^*}{s_D^*} - k_2 \frac{dp_0^*}{p_0^*} \right) \qquad (4.18)$$

71

The model has relatively few model constants (less than the BBM when taken with the calibration of the water retention curve). On the other hand, the authors suggest that "*the modelling of water retention behaviour (...) is relatively crude and future refinement may be desirable*" which would likely imply the addition of extra parameters to calibrate. According to Wheeler et al. (2003) the "*use of the stress variables σ_{ij}^* and s^* results in several important advantages. These include strain increment variables that are integrable, decoupling of elastic behaviour, very simple shapes for the LC, SI and SD yield curves, and a relatively small number of soil constants (given the capabilities). These advantages justify the use of stress variables that are more complex than the conventional choice of net stresses and suction.*" Recently the model has been amended to include bounding surface plasticity with just one additional parameter. More information can be found in Raveendiraraj (2008).

Note that the stress σ_{ij}^* has a quite straightforward physical interpretation. σ_{ij}^* is an average skeleton stress when the effect of menisci are disregarded (see chapter 3 for details). Assuming initially that suction acts on the volume of voids, the modified suction s^* can be interpreted as suction averaged over the whole volume of soil as

$$s^* = \frac{e}{e+1}s = ns \qquad (4.19)$$

where e and n are the void ratio and porosity respectively.

It is disputable whether the introduction of the new stress and strain variables is a step in the right direction, especially without a proper thermodynamical derivation of the model. Once the model is expanded to describe the shear states and the water retention behaviour is captured more accurately, the number of required model constants to calibrate will increase. It is likely that the total number of parameters will be equal or exceed those for the BBM. In such a case, the model, having stress variables more difficult to understand by practicing engineers, is not that likely to be employed in engineering practice unless it will provide significantly better results than the BBM. This may be difficult, as it seems that the major weakness of the BBM lies not in the description of the isotropic states but rather in prediction of soil behaviour in non-isotropic states. Also, the anisotropy of soil may sometimes play a role. In such cases a simple "pedagogic" model of Ghorbel and Leroueil (2006) may be a better choice. Despite the critique above, the model proposed by Wheeler et al. (2003) is attractive as

its framework is quite appealing, with the choice of stress and suction variables inspired by thermodynamics. It would be an additional advantage of the model if it could be derived within the thermodynamical framework. However, it must be noted here that, as for today, the model does not seem to offer significant improvements either in the prediction of unsaturated soil behaviour or in the correctness of derivation, as compared to the BBM.

4.4. Summary

There are a number of constitutive models designed to predict the behaviour of unsaturated soil under certain conditions. The quality of the prediction depends on the problem the model is used to analyse. Generally, the more advanced the model is and the more material constants the model has, the wider the range of soils can be covered and the more accurate the simulations can become. None of the described models is, however, able to accurately predict behaviour of unsaturated soil under complicated loading that e.g. include many cycles of wetting and drying and several cycles of loading. It is likely that the major shortcoming of many existing models is their drive towards a greater number of constants (essentially a consequence of curve fitting exercise) that are difficult to obtain from the laboratory tests. This leads to models expensive to use, not only in terms of cost of the laboratory tests required, but also in terms of knowledge necessary to successfully choose the model constants and use it within finite element code.

Additionally, the majority of the models are created without respect to both the laws of thermodynamics and the evolution of the soil fabric microstructure. The ideal model should provide insights in the evolution of soil microstructure, as only then can the macroscopic model be truly versatile (one step in this direction are models of soil microstructure evolution proposed by Koliji et al. 2006 and Ferber et al. 2006). It would also be advisable if such a model were thermodynamically consistent, as otherwise its usability would have to be limited to certain stress paths. A model which would provide correct predictions of soil behaviour in great majority of cases and give insights into micro- and macrostructure of unsaturated soils seems to be, however, quite far away.

In the next chapter some ideas that allow for enhancing the response of soil without increasing the number of model constants required are presented.

5. Multi-cell enhancement to constitutive models

In this chapter some modifications to the constitutive models are proposed. They should enhance the ability of the models to approximate the behaviour of unsaturated soils, especially during the transition from elastic to elasto-plastic behaviour. The described idea is introduced into BBM and examples of its performance given. Finally some ideas for future development of constitutive models for unsaturated soils are suggested.

5.1. Concept of multi-cell enhancement

The idea of the proposed multi-cell enhancement for the constitutive models stems from examination of the microstructure and water retention in unsaturated soils. Most constitutive models (with the exception of models using a double structure framework, such as developed by Gens and Alonso 1992) ignore important aspects of microscopic soil fabric and thus assume a homogeneous medium, simply extending the continuum constitutive frameworks developed for fully saturated soils. However, as described in section 2.2 fine grained unsaturated soil can have a much more complex fabric at the microscopic level than saturated soil. The clay platelets combine together creating larger clusters, commonly referred to as aggregates (as pointed out already by Alonso et al. 1987). The pores between the aggregates (macropores) are larger than within the aggregates (micropores) which leads to a double porosity structure. Such a structure can be seen in environmental scanning electron microscopy (ESEM) images and is confirmed by mercury intrusion porosimetry (MIP) tests (see e.g. Monroy 2005).

The non-homogeneous microstructure of unsaturated soil is also indirectly confirmed by the water retention curve. This curve describes the relationship between the suction and the water content for a given soil. The amount of water retained under a given suction is related to the pore size distribution of the soil according to the Young-Laplace equation. Therefore, the water retention curve can be used to calculate the radius of the largest pores filled with water at a given suction. As the water content of soil is known, the volume of pores with a smaller radius than this can also be estimated (Romero 1999).

Such an estimation of pore sizes in unsaturated soil via the water retention curve is helpful but imperfect, as the drying/wetting of the soil leads to changes in its structure. The soil structure (skeleton) may change irreversibly as the wet portion of soil is drawn together or undergoes swelling due to the spatial variation of suction. So, while the

water retention curve can be used to estimate the pore size distribution, the outcome will not be entirely representative for the soil given the non-uniqueness of the relationship between suction and water content caused by both irreversible strains and hydraulic hysteresis. This dependence of water retention behaviour on the soil deformation history has indeed been observed during experiments and partially incorporated in recent models for water retention behaviour (e.g. Gallipoli et al 2003b).

Despite the shortcomings mentioned above, the water retention curve carries useful information about the microstructural behaviour of unsaturated soil. It is thus appropriate to use this information in constitutive modelling. To keep the modification as simple as possible, it is assumed that a unique water retention curve (independent from the deformation and wetting/drying history of soil) exists.

Such a water retention curve can be expressed as a direct relationship between suction and degree of saturation. Given this relationship, it is straightforward to determine what percentage of soil has experienced a maximum given value of suction – it is the corresponding value of degree of saturation S_r read from the water retention curve. It follows that at a given value of suction, the average mean stress acting on the soil skeleton is equal to the sum of the external stress p and the current suction multiplied by the corresponding degree of saturation sS_r as described in chapter 2 and 3.

Such an average stress does not account, however, for the history of soil, i.e. it does not take into account that the parts of soil which are currently dry, previously experienced suction. Here, an assumption has been made that the dried part of soil behaves 'as though' the suction value that it has recently experienced is still acting. Thus the partially saturated soil can be divided into two parts. In the wet part current value of suction is acting. The soil in the dry part is modelled with the most recently experienced value of suction. This results in a continuous distribution of suction for modelling purposes in the dry part. This continuous distribution is approximated by dividing the whole soil volume into cells, where the number of cells is controlled by the user. In each cell the most recently experienced suction is stored. Of course, in the cells corresponding to the wet part of soil volume, which is S_r percent of cells, the most recently experienced suction is the current suction.

Having the suction distribution for all the cells, in each cell a separate instance of the constitutive model is run. Thus, during the analysis each cell experiences the same mean stress, but has its own separate hardening parameter value and suction. The assumption

of equal stress means that the strains in each cell may be different. Thus, after the computations, the final deformation is an average of all the cells deformations.

As a separate instance of constitutive model is run for each cell, this may be expensive in term of calculation time. Because of this, the number of cells, n, must be chosen to provide balance between satisfying computational efficiency and realism.

5.2. Multi – cell Barcelona Basic Model

The multi-cell concept, as described above, has been implemented in the BBM.

It is convenient to assume that in the initial state the material is saturated, so that the initial value of suction in all cells is set equal to zero. The other assumption made at the beginning of the simulation is that the hardening parameter p_0^* (BBM preconsolidation stress for saturated conditions) in all cells is identical. Once suction is applied, the values of current preconsolidation pressure p_0 in each cell are dependent on the value of hardening parameter p_0^* and the most recently experienced suction s

$$p_0 = p_0(p_0^*,s) = p^c \left(\frac{p_0^*}{p^c} \right)^{\frac{\lambda(0)-\kappa}{\lambda(s)-\kappa}} \tag{5.1}$$

where p^c is the value of the reference stress and $\lambda(s)$ is the slope of the virgin compression line at suction s. This slope is calculated as

$$\lambda(s) = \lambda(0)\left[(1-r)e^{-\beta s} + r\right] \tag{5.2}$$

where $\lambda(0)$ is the slope of the virgin compression line for the fully saturated soil, r and β are BBM constants. In every cell a separate instance of the BBM is used and, subsequently, the values of deformations from all cells are averaged.

5.2.1. Example

In this section an illustrative example is given. To keep the example as simple as possible it was decided to use 5 cells (n=5). The water retention curve is given in Figure 5.2. Initially (Fig. 5.1, point A) the soil is fully saturated, with a mean net stress p of 10 kPa which is also the value used for the reference pressure p^c in BBM. The soil is normally consolidated, so the hardening parameter p_0^* is equal to 10 kPa. The other BBM parameters used were: elastic stiffness parameter for changes in net mean stress κ=0.02, elastic stiffness parameter for changes in suction κ_s=0.05, atmospheric pressure

76

p_{atm}=100 kPa, stiffness parameter for changes in net mean stress for virgin states of the soil (with suction s=0) $\lambda(0)$=0.2, parameter defining the maximum increase of soil stiffness with suction β=0.01 1/kPa and parameter defining the maximum soil stiffness r=0.75. The initial specific volume at the reference pressure p^c is set to 2.6. The initial soil state is given in Table 5.1.

The stress path and corresponding values of the specific volume of soil are summarised in Figure 5.1. First, the soil is isotropic loaded until p=100 kPa (Fig. 5.1, path A-B). The state of soil after such loading is given in Table 5.2.

Table 5.1. Initial condition of soil (Fig. 5.1, point A)

Cell (i)	1	2	3	4	5
Hard. par. p_0^* [kPa]	10	10	10	10	10
Suction [kPa]	0	0	0	0	0
Specific Vol. N(0)*	2.6	2.6	2.6	2.6	2.6

*N(0) is the specific volume at the reference pressure p^c
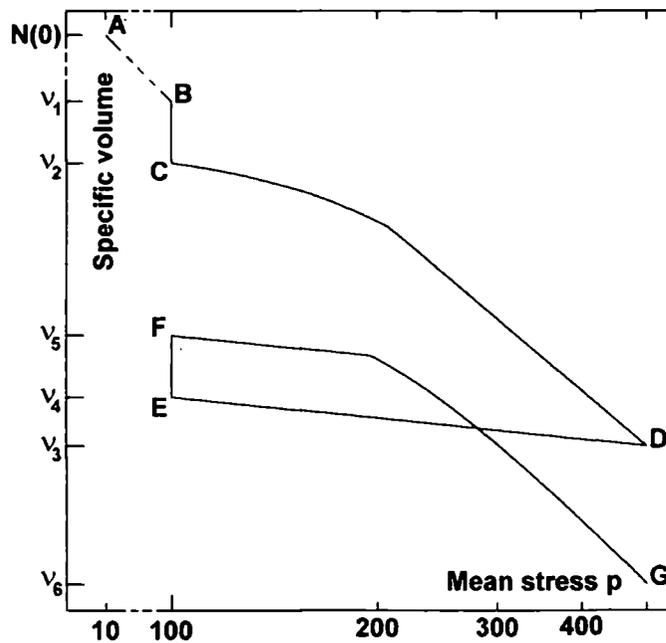
Figure 5.1. Stress path, as calculated in the example

Table 5.2. Soil state at p=100 kPa (Fig. 5.1, point B)

Cell (i)	1	2	3	4	5
Hard. par. p_0^* [kPa]	100	100	100	100	100
Suction [kPa]	0	0	0	0	0
Specific Volume v_1^i	2.139	2.139	2.139	2.139	2.139

At this stage (Fig. 5.1, point B) the values of specific volume for each cell v_1^i in Table 2 are equal and calculated as

$$v_1^i = N(0) - \lambda(0)\ln\frac{p_0^{*,i}}{p^c} \quad , i=1..5$$

(5.3)

The average specific volume is

$$v_1 = \frac{1}{n}\sum_{i=1}^{n} v_1^i = \frac{v_1^1 + v_1^2 + v_1^3 + v_1^4 + v_1^5}{5} = 2.139$$

(5.4)

where n is the number of cells used.

The soil is then dried until suction reaches 200 kPa (Fig. 5.1, B-C). The values of suction corresponding to S_r equal to 0.9, 0.7, 0.5 and 0.47 are 30 kPa, 100 kPa, 180 kPa and 200 kPa respectively (see Fig. 5.2). The cells are dried in a sequence, assuming that the cell is becoming dry when more then 50% of the cell is dried. This assumption leads to drying the cells once the degree of saturation reaches 0.9, 0.7, 0.5 which correspond to 30 kPa, 100 kPa and 180 kPa suction respectively (see Fig. 5.2). As at final suction 200 kPa the corresponding degree of saturation is 0.47>0.3, so the cells 4 and 5 remain wet. The evolution of cell suction is given by Table 5.3, where $s(S_r)$ denotes suction corresponding to the value of degree of saturation as given by the water retention curve (Figs 5.2 and 5.3).
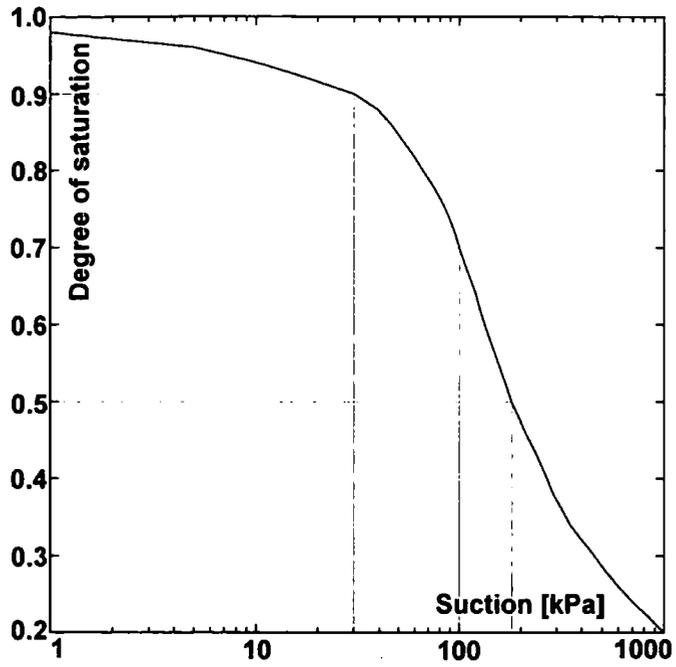
Figure 5.2. Water retention curve
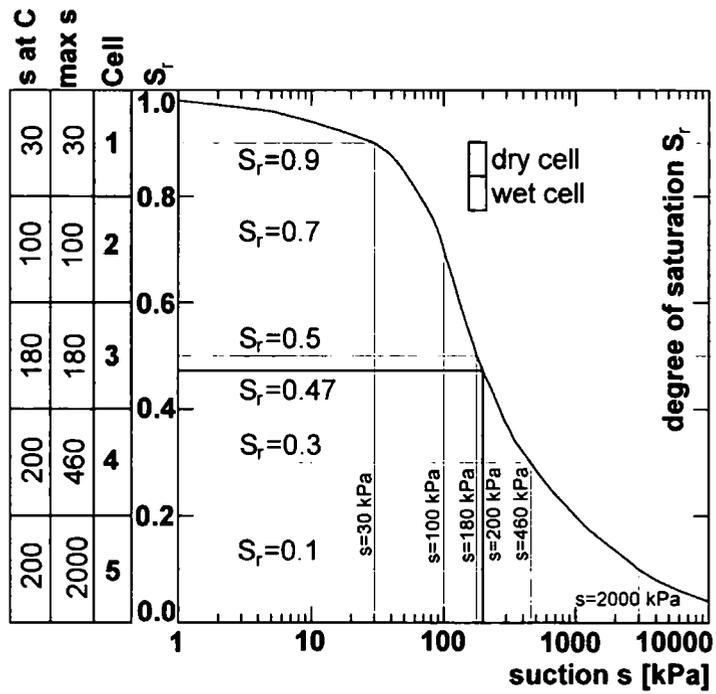
Figure 5.3. Illustration of suction distribution within cells after drying to s=200 kPa (Fig. 5.1, point C). A cell is assumed to be dry when its S_r <0.5.

Table 5.3. Evolution of suction during drying

Cell (i)	Suction Value [kPa]				
	1	2	3	4	5
$S_r > 0.9$	$s(S_r)$	$s(S_r)$	$s(S_r)$	$s(S_r)$	$s(S_r)$
$S_r = 0.9$	30	30	30	30	30
$0.9 > S_r > 0.7$	30	$s(S_r)$	$s(S_r)$	$s(S_r)$	$s(S_r)$
$Sr = 0.7$	30	100	100	100	100
$0.7 > S_r > 0.5$	30	100	$s(S_r)$	$s(S_r)$	$s(S_r)$
$S_r = 0.5$	30	100	180	180	180
$0.5 > S_r > 0.3$	30	100	180	$s(S_r)$	$s(S_r)$
$S_r = 0.47$	30	100	180	200	200

Table 5.4. Soil state after drying to s=200 kPa (Fig. 5.1, point C)

Cell (i)	1	2	3	4	5
Hard. par. p_0^* [kPa]	100	100	100	100	100
Suction [kPa]	30	100	180	200	200
Specific Volume v_2^i	2.126	2.104	2.088	2.084	2.084
Precons. pres. p_0^i [kPa]	119.6	163.3	200.4	207.1	207.1

Table 5.5. Evolution of hardening during loading

Cell (i)	Loading e – elastic		ep – elasto-plastic		
	1	2	3	4	5
$p < p_0^1$	e	e	e	e	e
$p_0^1 < p < p_0^2$	ep	e	e	e	e
$p_0^2 < p < p_0^3$	ep	ep	e	e	e
$p_0^3 < p < p_0^4$	ep	ep	ep	e	e
$p > p_0^4 = p_0^5$	ep	ep	ep	ep	ep

The soil state after drying is summarized in Table 5.4. The specific volume for each cell v_2^i and preconsolidation pressure p_0^i in Table 5.4 are calculated using

$$v_2^i = v_1^i - \kappa_s \ln \frac{s^i + p_{atm}}{p_{atm}} \quad , \; i = 1..5$$

(5.5)

$$p_0^i = p_0(p_0^{*,i}, s^i) = p^c \left(\frac{p_0^{*,i}}{p^c} \right)^{\frac{\lambda(0)-\kappa}{\lambda(s^i)-\kappa}} \quad , i=1..5 \tag{5.6}$$

where $p_{atm} = 100$ kPa is atmospheric pressure. The average specific volume is, similarly to equation (5.4), given by

$$v_2 = \frac{1}{n} \sum_{i=1}^{n} v_2^i = \frac{v_2^1 + v_2^2 + v_2^3 + v_2^4 + v_2^5}{5} = 2.097 \tag{5.7}$$

After drying, the soil is isotropically loaded to p=500 kPa (Fig. 5.1, C-D). This final value of mean net stress is higher than the value of the preconsolidation pressure p_0^5 given in Table 4, so all the cells will be at stress states on the yield locus. The evolution of elastic and elasto-plastic loading is given in Table 5.5. The soil state after loading to 500 kPa is given in Table 5.6. Note that after loading the cell hardening parameters are different

$$p_0^{*,1} > p_0^{*,2} > p_0^{*,3} > p_0^{*,4} = p_0^{*,5} \quad ,$$

whereas the preconsolidation pressure p_0 is the same for each cell. This is because the values of suction are different for cells 1, 2, 3 and 4.

As the cells do not yield at the same mean net stress (compare Table 5.5) the transition between elastic and elasto-plastic regime appears smoother than in the original BBM. The greater the number of cells used in the model, the smoother the transition.

Table 5.6. Soil state at p=500 kPa (Fig. 5.1, point D)

Cell (i)	1	2	3	4	5
Hard. par. $p_0^{*,i}$ [kPa]	377.3	253.6	202.6	195.4	195.4
Suction [kPa]	30	100	180	200	200
Specific Volume v_3^i	1.855	1.906	1.929	1.932	1.932
Precons. pres. p_0 [kPa]	500	500	500	500	500

The value of hardening parameters $p_0^{*,i}$ and specific volumes v_3^i in Table 6 are calculated using

$$p_0^{*,j} = p^c \left(\frac{p_0^i}{p^c} \right)^{\frac{\lambda(s^i)-\kappa}{\lambda(0)-\kappa}} \quad , i=1..5 \tag{5.8}$$

$$v_3^i = N(0) - \lambda(s^i)\ln\frac{p_0}{p^c} - \kappa_s \ln\frac{s^i + p_{atm}}{p_{atm}} \ , \ i=1..5 \tag{5.9}$$

The average specific volume is

$$v_3 = \frac{1}{n}\sum_{i=1}^{n}v_3^i = \frac{v_3^1 + v_3^2 + v_3^3 + v_3^4 + v_3^5}{5} = 1.911 \tag{5.10}$$

In the next stage, the soil is unloaded until it reaches the mean stress of 100 kPa (Fig. 5.1, D-E). The specific volume for each cell is then

$$v_4^i = v_3^i - \kappa\ln\frac{p}{p_0} \ , \ i=1..5 \tag{5.11}$$

The average specific volume is calculated similarly as before (see e.g. 5.4).

At this stage the sample is wetted until fully saturated (Fig. 1, E-F). The evolution of suction during wetting is given in Table 5.7 and the soil state after wetting is identified in Table 5.8. After saturation, the hardening parameters are unchanged and the value of preconsolidation pressure in each cell is equal to the value of hardening parameter in this cell.

Table 5.7. Evolution of suction during wetting [kPa]

Cell (i)	Loading e – elastic		ep – elasto-plastic		
	1	2	3	4	5
S_r=0.47	30	100	180	200	200
S_r<0.5	30	100	180	$s(S_r)$	$s(S_r)$
S_r=0.5	30	100	180	180	180
0.5<S_r<0.7	30	100	$s(S_r)$	$s(S_r)$	$s(S_r)$
S_r=0.7	30	100	100	100	100
0.7<S_r<0.9	30	$s(S_r)$	$s(S_r)$	$s(S_r)$	$s(S_r)$
S_r=0.9	30	30	30	30	30
S_r>0.9	$s(S_r)$	$s(S_r)$	$s(S_r)$	$s(S_r)$	$s(S_r)$

Table 5.8. Soil state after wetting (s=0 kPa) (Fig. 5.1, point F)

Cell (i)	1	2	3	4	5
Hard. par. $p_0^{*,i}$ [kPa]	377.3	253.6	202.6	195.4	195.4
Suction [kPa]	0	0	0	0	0
Specific Volume v_s^i	1.900	1.972	2.012	2.019	2.019
Precons. pres. p_0^i [kPa]	377.3	253.6	202.6	195.4	195.4

Table 5.9. Evolution of hardening during loading

Loading	e – elastic		ep – elasto-plastic		
Cell(i)	1	2	3	4	5
$p < p_0^{*,1}$	e	e	e	e	e
$p_0^{*,1} < p < p_0^{*,2}$	ep	e	e	e	e
$p_0^{*,2} < p < p_0^{*,3}$	ep	ep	e	e	e
$p_0^{*,3} < p < p_0^{*,4}$	ep	ep	ep	e	e
$p > p_0^{*,4} = p_0^{*,5}$	ep	ep	ep	ep	ep

Figure 5.4. Influence of number of cells used in simulation: comparison between simulation with 2 and 100 cells
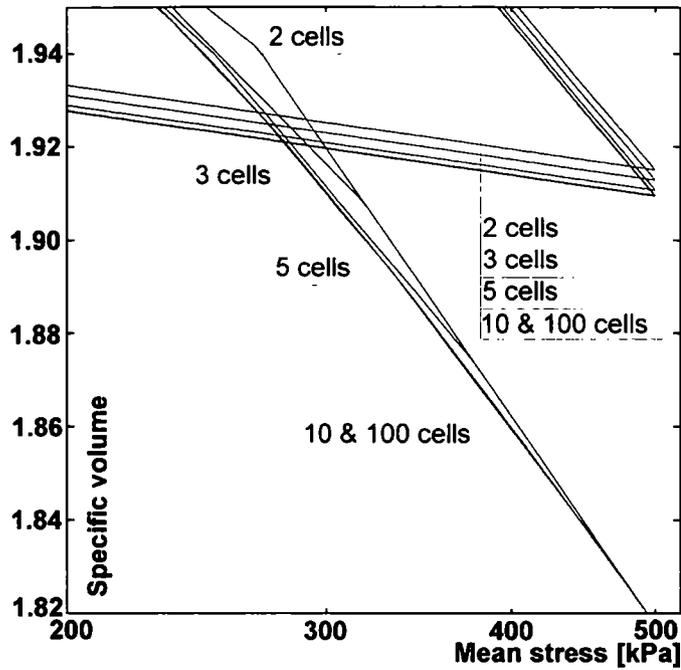
Figure 5.5. Influence of number of cells used in simulation – enlarged detail from Figure 5.4. Comparison between simulations using 2, 3, 5, 10 and 100 cells.

The specific volume in Table 5.8 is calculated as

$$v_5^i = v_4^i + \kappa_s \ln \frac{p + p_{atm}}{p_{atm}} , i=1..5 \tag{5.12}$$

The average specific volume is the mean of the specific volumes calculated in each cell (see 5.4).

Finally, the soil is loaded until the mean net stress p reaches a value of 500 kPa (Fig. 5.1, F-G). The loading is initially elastic, but as the mean stress increases, so the cells yield. The evolution of hardening during this loading is given in Table 5.9, and the final soil state is given in Table 5.10.

The value of specific volume for each cell is then calculated as in (5.3) and the average specific volume as in (5.4). Note that the plastic behaviour will start gradually, with some yielding of the material before reaching the virgin compression line. This gradual transition will be better approximated when more cells are used. The influence of the number of cells used is illustrated in the Figures 5.4 and 5.5.

Table 5.10. Soil state at p=500 kPa (final, Figure 5.1, point G)

Cell (i)	1	2	3	4	5
Hard. par. p_0^* [kPa]	500	500	500	500	500
Suction [kPa]	0	0	0	0	0
Specific Volume v_6^i	1.818	1.818	1.818	1.818	1.818
Precons. pres. p_0 [kPa]	500	500	500	500	500

5.2.2. Comparison with the original BBM

The comparison has been made using a problem given in section 5.2.1. All the parameters used for the BBM were the same as in the previous example. The test began with a mean net stress p=10 kPa on a saturated virgin compressed soil and the water retention curve is as depicted in Figure 5.2.

The comparison of the modified model prediction with the original BBM prediction (Fig. 5.6) reveals the differences. The slopes of the unsaturated compression lines are slightly different. This is to be expected, as the modified model effectively averages the specific volume and a range of suctions are operating within the material, whereas the original BBM uses only the current value of suction. The model can be calibrated, however, such that the fully yielded behaviour is similar. The other noticeable difference is the amount of elastic shrinking and swelling predicted by the models. This occurs because in the original formulation the shrinking depends on the final value of suction whereas in the modified form it is averaged over different changes in suction across the cells. As the shrinking and swelling behaviour are different, and the slope of the unsaturated compression line $\lambda(s)$ is steeper in the case of the modified model, the amount of collapse predicted by the original model is larger.

Finally, it is evident that the modified model predicts a smoother transition between the elastic and elasto-plastic regions. This smooth transition occurs also in the case of loading a fully saturated soil when it has previously been in an unsaturated state and was loaded beyond the yield point (of any of cells).
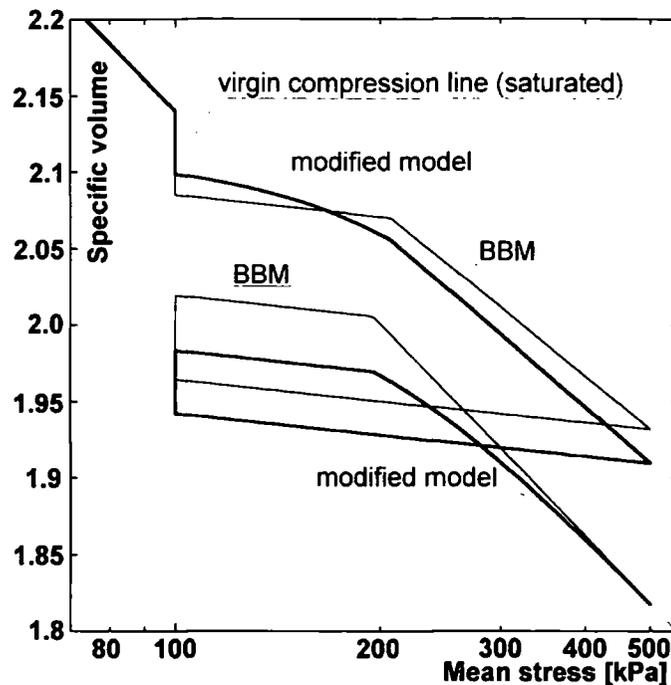
Fig. 5.6. Comparison of the modified BBM with the original formulation (for the same parameter set).

5.2.3. Comparison with experimental data

Although the concept of the multi-cell enhancement may look promising, only after comparing its performance against laboratory data can it be judged. In this section such a comparison has been made. The predictions of the BBM and the multi-cell enhanced BBM has been compared with data from Sharma (1998).

Sharma (1998) investigated 1:9 Wyoming sodium bentonite:speswhite kaolin mixture. This soil had liquid and plastic limits of 93% and 33% respectively. To prepare the soil for the test, it was initially powdered and dried at 105°C. Then water was added to reach 25% water content, which is on the dry side of optimum compaction. After mixing, the soil was sieved (using a 1.18 mm sieve). The remains on the sieve were grinded and sieved again, until all the whole mass of soil passed the 1.18 mm sieve. The soil was then stored keeping the water content constant for a week. The soil was mixed again before compaction which were performed using the standard Proctor procedure (simial to the scheme given in Fig. 2.14). After compaction, but before beginning of the main test, the soil samples were wetted in the triaxial cell under a given mean net stress until reaching the desired value of suction.

The Barcelona Basic Model has been calibrated to simulate the data from isotropic compression of samples with suction equal to 100, 200 and 300 kPa. The results of this BBM simulation and the experimental findings are given in Fig. 5.7. Such a good fit is

86

usually difficult to obtain, as BBM parameters are constrained by calibration at the fully saturated state. Here there were no such constraints, as no saturated tests were given; thus the parameters have been chosen to fit optimally these three tests. The parameters chosen for the simulation were: elastic stiffness parameter for changes in net mean stress $\kappa=0.01$, elastic stiffness parameter for changes in suction $\kappa_s=0.1$, atmospheric pressure $p_{atm}=100$ kPa, stiffness parameter for changes in net mean stress for virgin states of the soil (with suction s=0) $\lambda(0)=0.28$, parameter defining the maximum increase of soil stiffness with suction $\beta=0.00913$ 1/kPa and parameter defining the maximum soil stiffness r=0.349. The initial specific volume at the reference pressure p^c is set to 2.56. The reference pressure p^c was set to 10 kPa and the hardening parameter p_0^* to 18.8 kPa.

Keeping the MCC parameters of BBM constant, as they should fit the saturated state, changing the model constants r to 0.39 and beta to 0.0109 a new fit for the multi-cell enhanced BBM has been made (Fig. 5.8). It can be seen that the enhanced model fits the experimental data better during the elastic to elasto-plastic transition. The direct comparison of BBM and multi-cell enhanced BBM is given on Figs 5.9–5.11. Note that the experimental curves for suction 200 and 200 kPa have nearly identical initial specific volume whereas the initial specific volume for curve corresponding to suction 100 kPa is substantially higher. This result may be specific for the tested soil or be a result of slightly different samples used at tests. Such behaviour is not well approximated by the BBM.
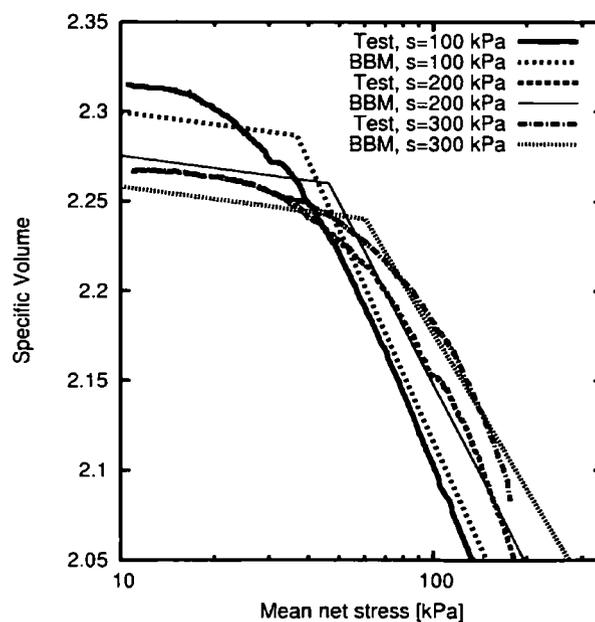
Figure 5.7. BBM approximation of experimental data. Data after Sharma (1998).
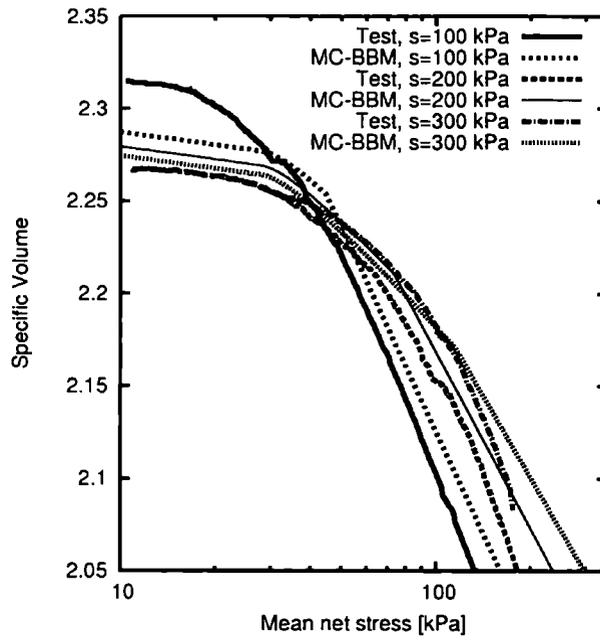
Figure 5.8. Multi-cell enhanced BBM (MC-BBM) approximation of experimental data. Data after Sharma (1998).
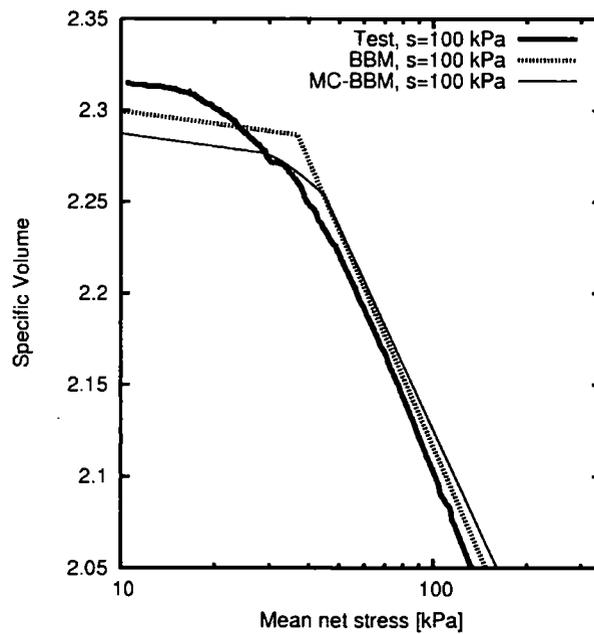
Figure 5.9. Multi-cell enhanced BBM (MC-BBM) and BBM approximation of experimental data. Data after Sharma (1998).
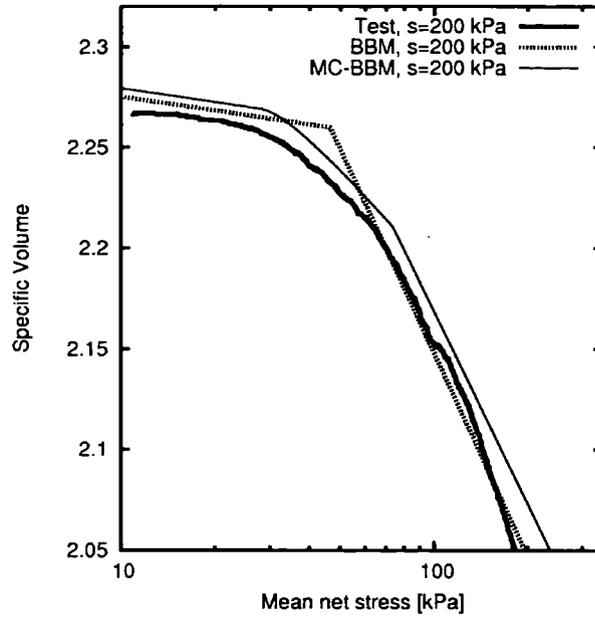
Figure 5.10. Multi-cell enhanced BBM (MC-BBM) and BBM approximation of experimental data. Data after Sharma (1998).
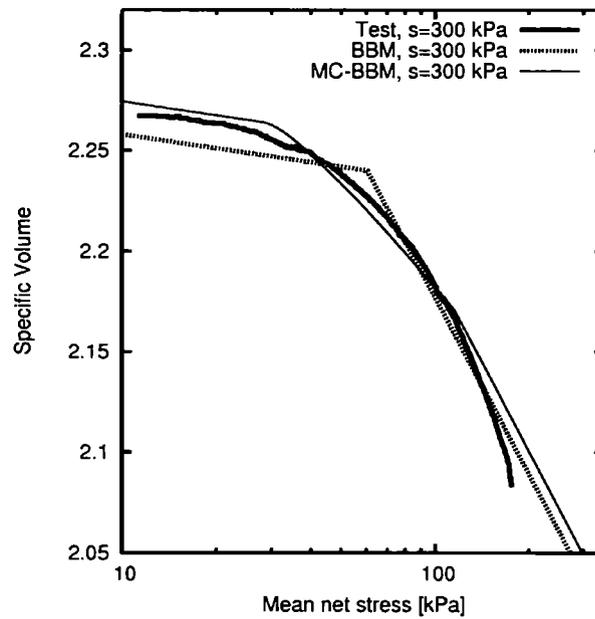
Figure 5.11. Multi-cell enhanced BBM (MC-BBM) and BBM approximation of experimental data. Data after Sharma (1998).

One can see that although the transition between elastic and elasto-plastic state is closer to the laboratory data, the general modelling ability of the multi-cell enhanced BBM is similar to the original BBM,. This is to be expected, as the multi-cell enhancement does not change the core abilities of the model. The smoothing of the response, by using the

multi-cell approach may also offer greater numerical stability in a large scale Finite Element analysis.

5.2.4. Conclusions

The proposed modifications to the BBM improve the capabilities of the model by offering a gradual change of stiffness during initial yielding. The number of parameters in the model is unchanged as the water retention curve is also a pre-requisite for the BBM. The proposed solution may be regarded as a 'partial-fix' to the model working only for unsaturated states, as no smoothing effect is present for saturated soil.

The calibration of the model requires some care, as calculations of the slope of the unsaturated compression line slope $\lambda(s)$ and amount of elastic shrinking/swelling is not so straightforward. The calibration process could employ an optimisation algorithm which would allow for automation of the process. Alternatively, the model parameters may be computed in a series of approximations. The latter approach would require an algorithm that would calculate deformations under given loading. It should be pointed out that the calibration of the model still does not require a greater number of tests than those required for the BBM. This is certainly an advantage over a model that would introduce a bounding surface plasticity framework into the BBM.

The amount of computer resources required is higher than for the BBM. However, on current machines, it is entirely feasible to perform 2D Finite Element simulations with more than 10^5 elements using the enhanced model. Given that the speed (and memory) of computers continues to increase, it is very likely that in few years 3D analyses will be almost as quick as current 2D simulations.

It is worth adding that the algorithm complexity of this enhanced model is not significantly increased compared with the original BBM, as much of the code used for each of the cells is the same.

5.3. Random enhancement of the multi-cell concept

The multi-cell concept may be enhanced to enable the model to capture hysteresis during cyclic wetting and drying. This can be achieved by randomly choosing the cell to be dried from all the wet cells (and putting it in a random place between the dry cells), instead of drying and wetting the cells always in the same order. This may result in progressively higher values of the hardening parameter in dried cells following a decrease in specific volume and in an increase of suction value stored in the dried cells.

Of course, when no drying and wetting cycles occur, then, the behaviour of the model would remain the same as the model described previously. The drawback of this approach is that to capture hysteresis in many cycles, a large number of cells is required which slows down computations.

To demonstrate capabilities of such an enhanced multi-cell BBM, a similar example has been used to the one in section 5.2.1. The soil is however instead initially dried until suction reaches 200 kPa, and then loaded to 100 kPa. At this stage, multiple cycles of drying and wetting are made during which the soil is wetted to suction 100 kPa and then dried back to suction 200 kPa. In the example one, five and fifty such cycles were simulated. Subsequently the loading in this example is the same as in section 5.2.1, that is the soil is loaded until 500 kPa mean net stress, unloaded, fully wetted and loaded again. The behaviour of the multi-cell enhanced BBM with this random sequence of cell drying (RMC-BBM) is given in Fig. 5.12 where the model is also compared to a multi-cell enhanced BBM (MC-BBM) described in section 5.2. In Fig. 5.13 the increase of specific volume during cycles of drying and wetting is shown. Finally Fig. 5.14 shows the consequence of using an increasing number of cells when modelling cyclic wetting and drying.
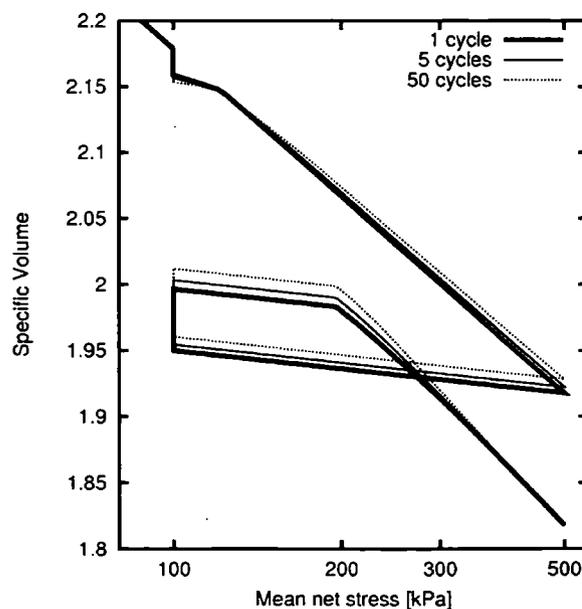
Figure 5.12. Random multi-cell enhanced BBM (RMC-BBM) with one, five and fifty wetting and drying cycles. The MC-BBM solution is equal to RMC-BBM with one cycle.
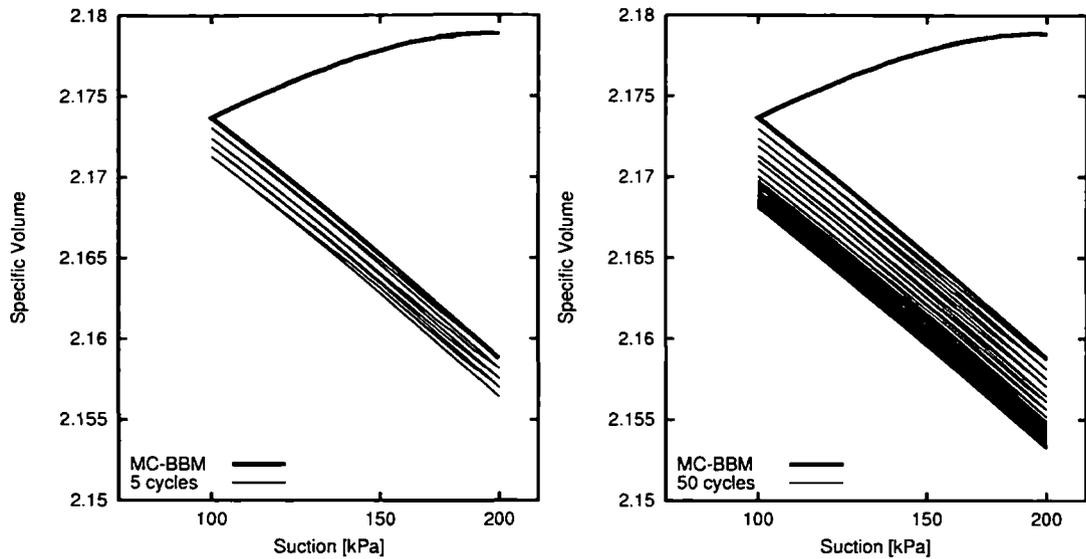
Figure 5.13. Random multi-cell enhanced BBM (RMC-BBM) with five (left) and fifty (right) wetting and drying cycles. The MC-BBM solution is equal to RMC-BBM with one cycle.
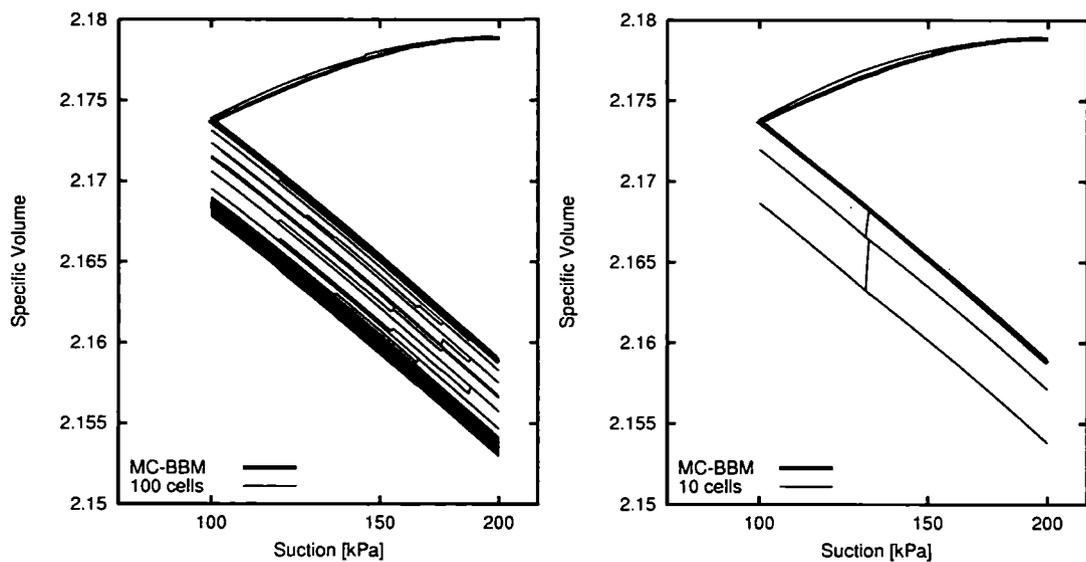
Figure 5.14. Random multi-cell enhanced BBM (RMC-BBM) modelling fifty wetting and drying cycles with 100 (left) and 10 (right) cells. The number of cells heavily influences the quality of model prediction (compare also Fig. 5.13 right). The MC-BBM solution is equal to RMC-BBM with one cycle – the difference in the figure is due to 1000 cells used in MC-BBM solution.

The effect of the decrease of specific volume during cyclic wetting and drying is a result of an initially wet cell being dried at lower suction. In such a cell, collapse may occur. The result of such process is a decrease in total specific volume. Other effect is the increase of suction in the cells which are dry during whole cycle of wetting and drying which lead to small decrease of specific volume due to shrinkage.

92

After a large number of loading cycles combined with wetting and drying, all the cells will have the hardening parameter set to the one corresponding to the lowest suction during cycles and no further influence of wetting and drying will be given by the model. How many cycles are required for such a situation to occur depends on the number of cells used and the range of suction in drying-wetting cycles. Note that due to random nature of the model, the outcome will not always be the same, especially with low number of cells used. This means that the final specific volume as given in Fig. 5.14 right may be reached not after fifty cycles, but after just five or ten cycles. Such a situation is highly unlikely when a larger number of cells is used, as the probability of wetting all the cells with lowest hardening parameter in subsequent cycles of wetting and drying is several magnitudes lower when a large number of cells is used.

5.4. Future research and conclusions

Constitutive models for unsaturated soils are still unable to predict the general soil behaviour in a convincing way. The simulation ability of the models increases with the number of model parameters. However a model with many constants is difficult and expensive to calibrate. Here a multi-cell enhancement has been proposed where no additional model constants are required. The multi-cell enhanced models are likely to offer better abilities of modelling the soil behaviour between elastic and elasto-plastic states without any decrease in overall modelling abilities. The random multi-cell enhancement also allows capturing the increase of soil deformations due to cyclic wetting and drying. This is also achieved without introduction of any additional model parameters.

It seems likely that an increased understanding of unsaturated soil behaviour will likely lead to a new generation of constitutive models. The ideal model should give insights in micro- and macrostructure changes of the unsaturated soil and be not only a good engineering tool, but also a tool that captures the underlying physics of the unsaturated soil behaviour. Ideally, the new models should have meaningful parameters which should be simple and unequivocal to calibrate. Finally, they should be constructed within a thermodynamically consistent framework – otherwise they are unlikely to be truly universal.

6. Stress integration of constitutive models for unsaturated soils: Theory

Constitutive models for unsaturated soils can be complex and for their application to cases of practical importance the aid of a digital computer is necessary. Such models idealise the behaviour at a material point, thus they need to be implemented in computer algorithms, most often Finite Element (FE) codes, to allow analysing of large-scale engineering structures.

The stress integration procedure is one of the crucial procedures in the FE approach and its proper implementation is important both for stability and efficiency of the code.

Integration algorithms are divided into two broad groups: (i) explicit algorithms where the integrated stress is obtained using the stiffness at the start of each integration step and (ii) implicit algorithms, where the stress increment is calculated using the stiffness at the end of the integration step (this requires an iterative approach as the values at the end of the step are initially unknown). Both methods are used in practice and have their own advantages and disadvantages.

A general description of implicit algorithms may be found in Simo and Hughes (1998) wherein an extensive list of references is available. Implicit algorithms for the integration of elasto-plastic models for saturated soils were developed, among others, by Borja and Lee (1990) and Borja (1991). Some novel ideas were more recently presented by Wang et al. (2004) and Foster et al. (2005). With reference to unsaturated soils, Vaunat et al. (2000) proposed an implicit integration algorithm including a return mapping scheme for the Barcelona Basic Model (BBM) of Alonso et al. (1990). Further implicit algorithms for unsaturated soil were proposed by Zhang et al. (2001) and Borja (2004).

Explicit algorithms, because of early adoption of the poorly performing Forward Euler Method, have been often considered less efficient than implicit algorithms, although they are regarded as simpler to code and more generally applicable. A new class of explicit algorithms with substepping and error control based on a local error estimate was adopted for geomechanics by Sloan (1987). Such explicit algorithms are now widely used, especially for advanced elasto-plastic constitutive models. They are significantly easier to code, while being competitive with implicit algorithms (if not better than them) in terms of computer resource usage and accuracy, especially when

high accuracy of the solution is required (see Potts and Zdravkovic 1999). Explicit algorithms using substepping have been progressively refined during past years, but only recently they have been applied to elasto-plastic models for unsaturated soils (e.g. Sheng et al. 2003a, b).

In this work, explicit stress integration schemes with substepping and error control have been adopted because of their greater flexibility and better error control than implicit algorithms. However, given that several such explicit integration schemes are available, detailed research has been performed here to find the method that is most advantageous in terms of robustness, efficiency and quality of error control. In the following sections, a number of explicit integration schemes with substepping and error control, based on different versions of the Runge-Kutta methods, as well as on a novel application of the extrapolation method, will be presented.

6.1. Description of Runge-Kutta stress integration algorithm

Runge-Kutta integration schemes have been adopted for stress integration by Sloan (1987). The general formulation of those algorithms is similar to the Runge-Kutta (RK) schemes widely used for the solution of ordinary differential equations. RK schemes with substepping and automatic error control described by Sloan (1987) include a second order Modified Euler scheme and a fifth order England scheme. Of the two algorithms, the Modified Euler has become far more popular. In this section a general description of a Runge-Kutta algorithm is given as an introduction to the novel developments proposed later in this thesis.

6.1.1. Stress integration problem

Elasto-plasticity is expressed in infinitesimal (rate) form, where the stress increment due to strain change is given by

$$\Delta\sigma = \int_{\varepsilon}^{\varepsilon+\Delta\varepsilon} \dot\sigma d\varepsilon \qquad (6.1)$$

where $\Delta\sigma$ is the stress increment to be calculated and $\Delta\varepsilon$ is the given strain increment. In general it is not possible to integrate (6.1) analytically. Thus we are restricted to approximations through numerical integration. Equation 6.1 follows from the governing infinitesimal form

$$\frac{d\sigma}{d\varepsilon} = \mathbf{D}^{ep}(\varepsilon, \sigma, \mathbf{h}) \tag{6.2}$$

where $\mathbf{D}^{ep}(\varepsilon, \sigma, \mathbf{h})$ is the elasto-plastic tangent matrix (or, in the case of elasticity, the elastic matrix) depending on the strain state ε, stress state σ and hardening parameters $\mathbf{h}$. Equation (6.2) is an ordinary differential equation of first order. Such an equation can be solved numerically in many ways (see e.g. Lambert 1973, Butcher 1987, Shampine 1994, Dormand 1996, Deuflhard and Bornemann 2002).

By reading through the broader literature covering both fields of mathematics and engineering, one can get the impression that the mathematicians and physicists seem to favour explicit methods for solving such equations whereas, in engineering, the implicit schemes are rather popular. The preference of engineers for implicit methods may be due to two main reasons: a) implicit methods, while being usually accurate enough for practical purposes, are regarded as more stable and b) implicit methods are usually used in conjunction with a consistent elasto-plastic matrix, which leads to a quadratic rate of asymptotic convergence of the Finite Element solution at global level. These often heard presumptions are not in line with some published evidence (e.g. Potts and Ganendra 1994). Thus a wide study regarding stability and accuracy of explicit stress integration has been made and will be presented in the subsequent chapter.

6.1.2. Runge – Kutta method

The simplest explicit method for the solution of equation (6.1) is the Forward Euler scheme. If this scheme is used with substepping, the strain to integrate $\Delta\varepsilon$ is divided into subincrements $\delta\varepsilon_i$ such that $\sum_i \delta\varepsilon_i = \Delta\varepsilon$. The matrix $\mathbf{D}^{ep}(\varepsilon, \sigma, \mathbf{h})$ is calculated at the beginning of each subincrement and the corresponding stress subincrement is obtained by simple multiplication of such matrix with the strain subincrement. This method, however, is inaccurate unless a very large number of subincrements is used, resulting in high computational costs.

The Runge-Kutta methods may be seen as an evolution of the Forward Euler scheme. One of the most basic Runge-Kutta approaches adopted for stress integration is the Modified Euler approach (Sloan 1987). Here each stress subincrement $\delta\sigma_i$ is calculated as an average of two stress estimates $\delta\sigma_i^{(1)}$ and $\delta\sigma_i^{(2)}$. The first stress subincrement estimate $\delta\sigma_i^{(1)}$ is computed using the elasto-plastic $\mathbf{D}^{ep}$ matrix corresponding to the

initial (i.e. at the beginning of the i-th subincrement) values of strain, stress and hardening parameters (denoted by subscript zero)

$$\delta\sigma^{(1)} = \delta\sigma^{(1)}(\varepsilon_0, \sigma_0, \mathbf{h}_0) \tag{6.3}$$

Then, for the same strain subincrement, a second stress subincrement estimate $\delta\sigma_i^{(2)}$ is calculated, this time with the $\mathbf{D}^{ep}(\varepsilon, \sigma, \mathbf{h})$ calculated for the updated quantities of strain, stress and hardening parameter

$$\delta\sigma_i^{(2)} = \delta\sigma_i^{(2)}(\varepsilon_0 + \delta\varepsilon_i, \sigma_0 + \delta\sigma_i^{(1)}, \mathbf{h}_0 + \delta\mathbf{h}_i^{(1)}) \tag{6.4}$$

where the hardening parameter estimate $\delta\mathbf{h}_i^{(1)}$ corresponds to the stress subincrement estimate $\delta\sigma_i^{(1)}$. The calculation of $\delta\mathbf{h}_i^{(1)}$ is specific to a given constitutive model. For example, when the hardening parameter depends on volumetric plastic strain only, this hardening parameter subincrement estimate can be computed as

$$\delta\mathbf{h}_i^{(1)} = \frac{\partial\mathbf{h}}{\partial\varepsilon_v^{pl}}(\delta\varepsilon_v^{pl})^{(1)} = \frac{\partial\mathbf{h}}{\partial\varepsilon_v^{pl}}\Lambda^{(1)}\frac{\partial G(\sigma, s, \overset{\bullet}{p_0})}{\partial\sigma} = \Lambda^{(1)}\frac{\partial\mathbf{h}}{\partial\varepsilon_v^{pl}}\frac{\partial G(\sigma, s, \overset{\bullet}{p_0})}{\partial\sigma} \tag{6.5}$$

where the plastic multiplier Λ is computed as part of the computations of $\mathbf{D}^{ep}$ matrix and G is the plastic potential function. Note that $\mathbf{h}$ will be a scalar measure for an isotropic elasto-plastic model where hardening depends only on the volumetric plastic strain. For further details see section 6.2.

The stress subincrement is taken as an average of these two stress estimates and the error estimate $\mathbf{E}$ is computed as half the difference between the two stress estimates.

$$\delta\sigma_i = 0.5(\delta\sigma_i^{(1)} + \delta\sigma_i^{(2)}) \qquad \mathbf{E}_i = 0.5|\delta\sigma_i^{(1)} - \delta\sigma_i^{(2)}| \tag{6.6}$$

The calculations are repeated for subsequent subincrements until the whole strain increment $\Delta\varepsilon$ is covered. The answer to the remaining question about how the strain $\Delta\varepsilon$ should be divided into subincrements $\delta\varepsilon_i$ is given in the subsequent section.

To sum up, calculation of the stress subincrements with the Modified Euler method requires two computations of the stress estimate. Thus the Modified Euler method has two stages in which $\delta\sigma^{(1)}$ and $\delta\sigma^{(2)}$ are calculated. It is also a method of second order, as it neglects only third order terms in the Taylor expansion series of the stress increment, and it has a first order error estimate, given that the solution from the Forward Euler Method is used for estimating the error.

Generally, Runge-Kutta methods can have a number of stages (NoS) larger than two and be of a high order. The order of error estimate is usually one order lower than the order of method itself. In the general formulation of Runge-Kutta methods, the stress estimate in stage 's' in a given subincrement is computed as

$$\delta\sigma^{(s)} = \delta\sigma^{(s)}\left(\varepsilon_0 + c^{(s)}\delta\varepsilon \, , \, \sigma_0 + \sum_{j=1}^{s-1} a^{(sj)}\delta\sigma^{(j)} \, , \, h_0 + \sum_{j=1}^{s-1} a^{(sj)}h^j\right) \tag{6.7}$$

The stress subincrement and error estimate are then calculated as

$$\delta\sigma = \sum_{s=1}^{NoS} b^{(s)}\delta\sigma^{(s)} \qquad E(\delta\sigma) = \sum_{s=1}^{NoS}\left(b^{(s)} - d^{(s)}\right)\delta\sigma^{(s)} = \sum_{s=1}^{NoS}\left(e^{(s)}\right)\delta\sigma^{(s)} \tag{6.8}$$

where $a^{(sj)}$ and $c^{(s)}$ are coefficients employed in the calculation of stresses in the s-th stage, $b^{(s)}$ are weighting factors allowing for the calculation of a high order solution and $d^{(s)}$ are the weighting factors for the one order lower Runge-Kutta method. The error estimate is computed as a difference between the higher and lower order solution (for values of the coefficients, see Appendix 1). Note that, in general, the values of hardening parameters also need to be calculated in similar fashion as those of stresses.

6.1.3. Error estimation and automatic subincrementation

As mentioned above, to integrate stresses with a Runge-Kutta method while maintaining a reasonable accuracy, the strain increment $\Delta\varepsilon$ has to be divided into subincrements $\delta\varepsilon_i$ (such that $\sum_i \delta\varepsilon_i = \Delta\varepsilon$). The subincrement size can be constant.

However, to make best use of computer resources, it is advisable to change the size of subincrements depending on the error made. This allows for creation of a method that is as efficient as possible while still satisfying the error criterion.

There are several ways of setting the next subincrement size. They usually rely on the error estimate in the most recently integrated subincrement (local error estimate), which is provided by all modern Runge-Kutta methods. One possibility for error correction is the Error Per Step (EPS) method where the user specifies a value below which the error in each subincrement must fall. A specific variation of the EPS error control was proposed by (Sloan 1987), where a relative value of error with respect to the value of the integrated variable must be below a specified tolerance. Finally in the Error Per Unit Step (EPUS) method the value of error in the subincrement must be below some percentage of the integrated value of the variable in this subincrement.

The EPS procedure advocated by Sloan (1987) is probably the most commonly used in engineering practice and is the method of error control used throughout the thesis. In this procedure, given the method order and the error estimate, the size χ of the next subincrement relative to the current subincrement size is calculated as

$$\chi = \xi \sqrt[m]{\frac{TOL}{\frac{\|E(\delta\sigma)\|}{\|\sigma_0 + \delta\sigma\|}}}$$

(6.9)

where TOL is the error tolerance set by the user, m is the order of the method and σ_0 is the stress value before integration of the last stress subincrement $\delta\sigma$. The coefficient ξ is a scalar safety factor, smaller than unity, used to reduce the new subincrement size to account for the fact that, during derivation of equation (6.8), the higher order terms in a Taylor series have been neglected (see Shampine 1994 for details). If the error estimate norm divided by total stress norm $\dfrac{\|E(\delta\sigma)\|}{\|\sigma_0 + \delta\sigma\|}$ is larger then the value of TOL, then the subincrement is rejected, the stress state is not updated and a new, smaller subincrement of strain is calculated using (6.9). Otherwise, the calculated value of stress subincrement is deemed accurate enough, added to the total stress and a new subincrement of size $\delta\varepsilon_{i+1} = \chi\delta\varepsilon_i$ is integrated. This error control method, in the case of strictly dissipative systems, should lead to the final error being close to the set error tolerance TOL (for a definition of strictly dissipative systems and proof see Shampine 1994).

Note that here only the error in the stresses has been considered. In practical analyses the error in the hardening parameter(s) should also be taken into account. To reduce the size volatility of the strain subincrements, it is recommended to limit the factor χ to the range of (0.1 – 10) or similar. This is essentially because the error estimate is based on a lower order embedded Runge-Kutta method and is thus inaccurate by itself. If we were to increase the step size more than 10 times, the neglected terms in the Taylor series expansion may become important (Shampine 1994).

The choice of the norm in (6.9) is important and influences the robustness and convergence of the stress integration. The norm used throughout the calculation was the maximum norm calculated for each stress component separately. Additionally error in mean net stress, shear stress and hardening parameter were computed. The largest error

from all those calculations was taken as indicative of the error made in the subincrement and used for accepting/rejecting the subincrement and in (6.9), for the calculation of the next subincrement size.

6.1.4. Drift correction

After accepting an elasto-plastic subincrement, a check on whether the computed stress state is close enough to the yield locus is performed. In case it is not, it is said that the stress state has 'drifted' from the yield locus. In such a case, a drift correction algorithm is invoked and the stress state is returned to the yield locus. The stress change due to the drift correction is added to the error estimate of the subincrement. Thus it is possible that after drift correction the subincrement will be rejected.

The drift correction follows the algorithm given in Potts and Zdravkovic (1999), which is based on the findings of Potts and Gens (1985). The need for drift correction arises when the resulting stress state after the Runge-Kutta subincrement does not lie on the yield locus (which is decided by the yield locus tolerance, see also 6.3.1). At the beginning of the subincrement the stress state corresponds to a point A on the yield surface, so the value of the yield function F for the initial value of stress and hardening parameters is equal to zero $F(\sigma_A, h_A) = 0$ (here '=0' denotes a stress state in a close proximity of the yield surface where the yield function has a value smaller than a given tolerance whereas '≠0' indicates that the yield function has an absolute value greater than the tolerance). After integrating the subincrement, the stress state and hardening parameters are updated to a new point B in stress space ($\sigma_B = \sigma_A + \delta\sigma$). If the point B does not satisfy the yield locus equation within the required tolerance, i.e. $F(\sigma_B, h_B) \neq 0$, then a correction is required to a final stress state corresponding to a point C in stress space, which satisfies the yield locus equation, i.e. $F(\sigma_C, h_C) = 0$. During the correction the total strain remains constant while changes in the elastic and plastic components of strain are equal in absolute value but opposite in sign

$$d\varepsilon_{el} = \left(D^{el}\right)^{-1}(\sigma_C - \sigma_B) \tag{6.10}$$

$$d\varepsilon_{pl} = -d\varepsilon_{el} = -\left(D^{el}\right)^{-1}(\sigma_C - \sigma_B) \tag{6.11}$$

The plastic strain is proportional to the gradient of the plastic potential G, i.e. $d\varepsilon_{pl} = \Lambda \dfrac{\partial G}{\partial \sigma}$ (the so-called flow rule) where Λ is a scalar. Thus the stress in point C is

$$\boldsymbol{\sigma}_C = \boldsymbol{\sigma}_B - \Lambda \mathbf{D}^{el} \frac{\partial G}{\partial \boldsymbol{\sigma}} \tag{6.12}$$

The change of plastic volumetric strain also triggers a change in the hardening parameter. Linearising, by differentiation, the generally non-linear equation of the hardening parameter gives the following relationship

$$d\mathbf{h} = d\mathbf{h}(d\varepsilon_{pl}) = d\mathbf{h}\left(\Lambda \frac{\partial G}{\partial \boldsymbol{\sigma}} \right) = \Lambda d\mathbf{h}(\frac{\partial G}{\partial \boldsymbol{\sigma}}) \tag{6.13}$$

The stress state at point C must also be consistent with the yield function

$$F(\boldsymbol{\sigma}_C, \mathbf{h}_C) = F\left(\boldsymbol{\sigma}_B - \Lambda \mathbf{D}^{el} \frac{\partial G}{\partial \boldsymbol{\sigma}}, \mathbf{h}_B + \Lambda d\mathbf{h}(\frac{\partial G}{\partial \boldsymbol{\sigma}}) \right) = 0 \tag{6.14}$$

Expanding equation (6.13) in a Taylor's series and neglecting terms in Λ^2 and above, after some rearrangement, gives the value of the scalar multiplier Λ

$$\Lambda = \frac{F(\boldsymbol{\sigma}_B, \mathbf{h}_B)}{\left(\frac{\partial F}{\partial \boldsymbol{\sigma}} \right)^T \mathbf{D}^{el} \frac{\partial G}{\partial \boldsymbol{\sigma}} - \left(\frac{\partial F}{\partial \mathbf{h}} \right)^T d\mathbf{h}(\frac{\partial G}{\partial \boldsymbol{\sigma}})} \tag{6.15}$$

To calculate Λ from (6.15) it would be advised to use the values of gradients and functions (thus stresses and hardening parameter) corresponding to the point C, but they are not known. Potts and Zdravkovic (1999) suggest using the values of stresses and hardening parameter at the beginning of the subincrement, i.e. at point A. They argue that, as point B lies in the illegal stress space outside the yield locus, using the values of derivatives at point B may lead to substantial errors.

Having calculated Λ the stress state at point C and the change in elastic and plastic strains are computed using (6.12), (6.10) and (6.11). In the case that the stress state is not mapped back to the yield surface after the first drift correction (which may generally happen when a strict yield locus tolerance is coupled with a loose integration tolerance), the procedure may be repeated using the new corrected stress state (which is again not on the yield locus) as the initial stress state (i.e. point B).

6.2. Advances in explicit stress integration

This section presents the developments undertaken in this work to apply explicit integration schemes with substepping and error control to elasto-plastic constitutive models for unsaturated soils and introduces a number of improvements made to existing

explicit stress integration algorithms. First it highlights the changes required for the application of existing stress integration algorithms to unsaturated soil models. Later, it describes the application of the extrapolation algorithm to the problem of stress integration. The extrapolation algorithm is well known to mathematicians and physicists but has never been used for stress integration. The section finishes with a description of the EPUS error control method, which also has not been previously tested in stress integration.

6.2.1. Stress integration of unsaturated soil constitutive models

Constitutive models for unsaturated soils are usually formulated by using additional stress variables compared to the saturated case. Stress integration for unsaturated soils must therefore accommodate the use of other variables in addition to the conventional stress and strain measures. All stress integration algorithms developed and tested in this work have been developed and tested with specific reference to the Barcelona Basic Model (BBM), arguably the best known of the elasto-plastic constitutive models for unsaturated soils. With respect to the saturated case, the BBM requires one additional scalar parameter: soil suction. In the stress integration algorithms presented in this work, suction is treated as an additional strain-like quantity but there is no stress corresponding to suction. This leads to non-square elastic $\mathbf{D}^{el}$ and elasto-plastic $\mathbf{D}^{ep}$ matrices, and an incremental stress-strain relationship where the six stress components are computed using seven strain increments, i.e. six mechanical strains plus suction.

$$\boldsymbol{\sigma} = \left\{\sigma_{11}, \sigma_{22}, \sigma_{33}, \sigma_{12}, \sigma_{13}, \sigma_{23}\right\} = \mathbf{D}^{el/ep} \cdot \left\{\varepsilon_{11}, \varepsilon_{22}, \varepsilon_{33}, \varepsilon_{12}, \varepsilon_{13}, \varepsilon_{23}, s\right\}^{T} \tag{6.16}$$

Details about the tangent elastic $\mathbf{D}^{el}$ and elasto-plastic $\mathbf{D}^{ep}$ matrices are given in section 6.3 describing the implementation of the stress integration algorithm for the specific case of the BBM.

6.2.2. Studied Runge-Kutta methods

For stress integration, two Runge-Kutta methods have been commonly used – the Modified Euler and the England method. In this study several other Runge-Kutta algorithms of different order have been developed and their performances compared. The Runge-Kutta algorithms coded in this work were:

(i)   Modified Euler method (Sloan 1987) - a second order scheme with embedded first order solution

(ii) two third order schemes with embedded second order solution and coefficients proposed by Nystrom (Gear 1971 and Lee and Schiesser 2003) and Bogacki-Shampine (Bogacki and Shampine 1996)

(iii) a fourth order scheme with embedded third order solution (Lee and Schiesser 2003)

(iv) four fifth order schemes with embedded fourth order solution and coefficients proposed by England (Sloan 1987 and Lee and Schiesser 2003), Cash and Karp (Press et al. 2002 and Lee and Schiesser 2003), Dormand and Prince (Dormand 1996) and Bogacki and Shampine (Bogacki and Shampine 1996)

Good performance had been expected from the relatively recent Bogacki-Shampine Runge-Kutta methods, as they have found a considerable acclaim among applied mathematicians (which resulted in implementation of Bogacki-Shampine schemes into several free libraries and codes containing solvers for ordinary differential equations, e.g. into Matlab; see also Bogacki and Shampine 1996). Unfortunately tests here show that, in the case of stress integration for the Barcelona Basic Model, this scheme seems to have no advantage over other Runge-Kutta schemes of the same order.

The relevant coefficients for the above Runge-Kutta methods are given in the Appendix.

6.2.3. Extrapolation method

The extrapolation method has its origin in the works of Richardson (see e.g. Gear 1971). It was first used for the solution of differential equations by Gragg (1965) and is well described by Lambert (1973). Since then, the extrapolation method has been refined, most importantly by Stoer and Bulirsch (2002), who present all the important concepts of the method. The extrapolation method has been praised for its robustness, stability and efficiency (e.g. Press et al. 2002). The method has never been used for stress integration and this work aims at exploring its efficiency and robustness with specific reference to the case of the integration of elasto-plastic constitutive models for unsaturated soils.

Contrary to the Runge-Kutta method that assesses the global error based on the local error estimate, the accuracy of the integration is assessed in the extrapolation method by directly using the global error estimate. This method is also much more stable than similar Runge-Kutta methods, as the strain to integrate is always divided into equally sized subincrements and the results obtained from the integration with a different number of subincrements are 'extrapolated' to calculate the final result. This

extrapolated result is significantly more accurate than any of the computed results for equally sized subincrements. Furthermore, the method should not be worse than a constant subincrement Midpoint method using the same number of subincrements as used in the last computation for extrapolation. The idea of the extrapolation method is shown in Fig. 6.1. To obtain the extrapolated result, stress was first integrated twice with the Midpoint method with two and four subincrements. Stress at the end of each of the subincrements is shown. The extrapolation method allows the stress to be calculated only at the final state (at the end of integration).
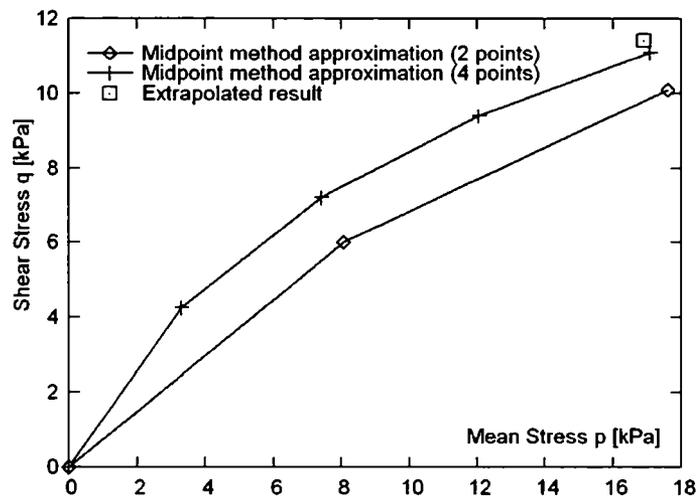
Figure 6.1. Extrapolation method: stress integrated with twice with constant subincrement size Midpoint method (with two and four subincrements) and the extrapolated result. Results obtained for error per step (EPS) error control.

In the extrapolation method an initial approximation of the stress increment $\Delta\sigma_0^{(0)}$ is calculated by dividing the corresponding strain increment $\Delta\varepsilon$ in a number N_0 of equal sub-increments $\delta\varepsilon_0 = \Delta\varepsilon/N_0$ and by using an explicit scheme to integrate stresses over each of these sub-increments. Subsequently a second approximation of the stress increment $\Delta\sigma_1^{(0)}$ over the same increment $\Delta\varepsilon$ is calculated by using a number of sub-increments $N_1 > N_0$. The linear combination of these two approximations yields a more accurate extrapolated approximation $\Delta\sigma_1^{(1)}$ (i.e. an approximation whose error series has a leading term of higher order than $\Delta\sigma_0^{(0)}$ and $\Delta\sigma_1^{(0)}$). The error estimate of such an extrapolated approximation is then computed and, if such error is acceptable, the calculations are terminated. Otherwise, another approximation of the stress increment $\Delta\sigma_2^{(0)}$ is calculated with a number of sub-increments $N_2 > N_1$. Similarly as above, the linear combination of $\Delta\sigma_2^{(0)}$ and $\Delta\sigma_1^{(0)}$ yields the extrapolated approximation $\Delta\sigma_2^{(1)}$,

which is then combined again with the previous extrapolated approximation $\Delta\sigma_1^{(1)}$ to give an even more accurate extrapolated approximation $\Delta\sigma_2^{(2)}$. If the error estimate is acceptable at this stage, calculations are terminated. Otherwise, a new approximation of the stress increment $\Delta\sigma_i^{(0)}$ is calculated by using a larger number of sub-increments $N_i > N_{i-1}$ and this approximation is used for calculating further extrapolated values. Such a process continues until the error estimate becomes smaller than the set tolerance.

The scheme is summarized in the following table

$$
\begin{array}{llllll}
N_0 & \Delta\sigma_0^{(0)} & & & & \\
N_1 & \Delta\sigma_1^{(0)} & \Delta\sigma_1^{(1)} & & & \\
N_2 & \Delta\sigma_2^{(0)} & \Delta\sigma_2^{(1)} & \Delta\sigma_2^{(2)} & & \\
N_3 & \Delta\sigma_3^{(0)} & \Delta\sigma_3^{(1)} & \Delta\sigma_3^{(2)} & \Delta\sigma_3^{(3)} & \\
\cdots & \cdots & \cdots & \cdots & \cdots & \cdots \\
N_i & \Delta\sigma_i^{(0)} & \Delta\sigma_i^{(1)} & \Delta\sigma_i^{(2)} & \Delta\sigma_i^{(3)} & \cdots \quad \Delta\sigma_i^{(m)}
\end{array}
\tag{6.17}
$$

The first column of stresses in table (6.17) show the non-extrapolated approximation $\Delta\sigma_i^{(0)}$ calculated by using an explicit integration scheme over N_i equal sized sub-increments $\delta\varepsilon_i$ (i.e. $\delta\varepsilon_i = \Delta\varepsilon/N_i$).

The other columns of table (6.17) contain the extrapolated approximation $\Delta\sigma_i^{(m)}$ (with $m>0$), which can be calculated as a linear combination of the approximations $\Delta\sigma_i^{(m-1)}$ and $\Delta\sigma_{i-1}^{(m-1)}$ according to the following two alternative rules

$$
\Delta\sigma_i^{(m)} = \Delta\sigma_i^{(m-1)} + \frac{\Delta\sigma_i^{(m-1)} - \Delta\sigma_{i-1}^{(m-1)}}{\left(\dfrac{N_i}{N_{i-m}}\right)^2 - 1}
\tag{6.18}
$$

where i,m=1,2,3,… or

$$
\Delta\sigma_i^{(m)} = \Delta\sigma_i^{(m-1)} + \frac{\Delta\sigma_i^{(m-1)} - \Delta\sigma_{i-1}^{(m-1)}}{\left(\dfrac{N_i}{N_{i-m}}\right) - 1}
\tag{6.19}
$$

where i,m=1,2,3,…

It can be shown that equations (6.18) and (6.19) provide extrapolated approximations whose error expansion series have leading terms of progressively higher order and therefore converge towards the true solution (see, for example, Gragg 1965). The

extrapolation rule of equation (6.18) is used when the error expansion series of the approximation $\Delta\sigma_i^{(0)}$ contains only even power terms such as

$$\Delta\sigma = \Delta\sigma_i^{(0)} + a_1\left(\frac{\Delta\varepsilon}{N_i}\right)^2 + a_2\left(\frac{\Delta\varepsilon}{N_i}\right)^4 + a_3\left(\frac{\Delta\varepsilon}{N_i}\right)^6 + \dots \tag{6.20}$$

Equation (6.19) is instead used when the error expansion series of the approximation $\Delta\sigma_i^{(0)}$ contains both odd and even power terms such as

$$\Delta\sigma = \Delta\sigma_i^{(0)} + a_1\left(\frac{\Delta\varepsilon}{N_i}\right)^1 + a_2\left(\frac{\Delta\varepsilon}{N_i}\right)^2 + a_3\left(\frac{\Delta\varepsilon}{N_i}\right)^3 + \dots \tag{6.21}$$

If the error expansion of the approximation $\Delta\sigma_i^{(0)}$ has the form of equation (6.20) (so equation 6.18 applies), then the algorithm converges faster as each subsequent extrapolation increases (by two) the order of the error of the leading term in the series.

Note that the superscript $^{(m)}$ in the approximation $\Delta\sigma_i^{(m)}$ refers to the number of subsequent extrapolations used to calculate that particular approximation. Thus those approximations with the same superscript $^{(m)}$ have leading terms of the error series of the same order. The subscript $_i$ in the approximation $\Delta\sigma_i^{(m)}$ identifies instead those approximations that belong to the same sequence of extrapolations (i.e. those approximations that are on the same row of table 6.17).

Different sequences of sub-increment N_i can be used in (6.17). It is only required that (i) all the numbers are even and (ii) each subsequent value of N is higher than the one before (for all $i>0$ $N_i<N_{i+1}$). The most common sequences are:

$$N_i = 2(i+1) \Rightarrow N = \{2, 4, 6, 8, 10, 12, 14,\dots\} \tag{6.22}$$

(Deuflhard 1983, 2002)

$$N_i = 2N_{i-2} \Rightarrow N = \{2, 4, 6, 8, 12, 16, 24, 32, 48, 64,\dots\} \tag{6.23}$$

(Stoer and Bulirch 2002, Lambert 1973)

$$N_i = 2^{i+1} \Rightarrow N = \{2, 4, 8, 16, 32, 64, 128,\dots\} \tag{6.24}$$

(Lambert 1973)

In the calculations the following sequence was used

$$N = \{32, 48, 64, 96, 128, 160, 192, 256, 320, 384, 448, 512, 608, 736, 992\} \tag{6.25}$$

This sequence performed best for the fairly large strain increments $\Delta\varepsilon$ used in this work (see section 7.2.1), although for smaller increments the sequences given in (6.22) or (6.23) are advantageous. It was also observed that the choice of the sequence of sub-increments may seriously influence the quality of the results and the computational time required for integration.

The extrapolation method does not have a fixed order as, for example, Runge-Kutta schemes. In the extrapolation method the order of the approximation depends on the number of subsequent extrapolations, i.e. on the number of columns in table (6.17). Each subsequent column has another term eliminated in the error series and thus gives a higher order approximation.

Graphical interpretation of the extrapolation method stages is given in Fig. 6.2. First stress increments were integrated three times, resulting in stress increments $\Delta\sigma_0^{(0)}$, $\Delta\sigma_1^{(0)}$ and $\Delta\sigma_2^{(0)}$. Those results are second order accurate. The extrapolation method initially calculates extrapolated results basing on integration with two and four subincrements resulting in $\Delta\sigma_1^{(1)}$ (Fig. 6.2, first magnification). Similar computation is done for stresses obtained from four and six subincrements which gives stress $\Delta\sigma_2^{(1)}$. Stresses $\Delta\sigma_1^{(1)}$ and $\Delta\sigma_2^{(1)}$ are fourth order accurate (under assumption of 6.20). Final stress $\Delta\sigma_2^{(2)}$ (sixth order accurate) is computed based on $\Delta\sigma_1^{(1)}$ and $\Delta\sigma_2^{(1)}$ (Fig. 6.2, second magnification).

An estimate of the integration error E over the strain increment $\Delta\varepsilon$ is obtained as (see Deuflhard and Bornemann 2002, Stoer and Bulirsch 2002)

$$E = \left\| \Delta\sigma_i^{(m)} - \Delta\sigma_i^{(m-1)} \right\| \tag{6.26}$$

In equation (6.26) $\Delta\sigma_i^{(m)}$ denotes the most accurate value in the extrapolation table (6.17) and $\Delta\sigma_i^{(m-1)}$ the second most accurate value on the same row.

In this work the extrapolation method has been implemented by using a constant subincrement Runge-Kutta Midpoint method (see Appendix) which has been employed for calculation of the approximate results for each stage of the extrapolation method.

107
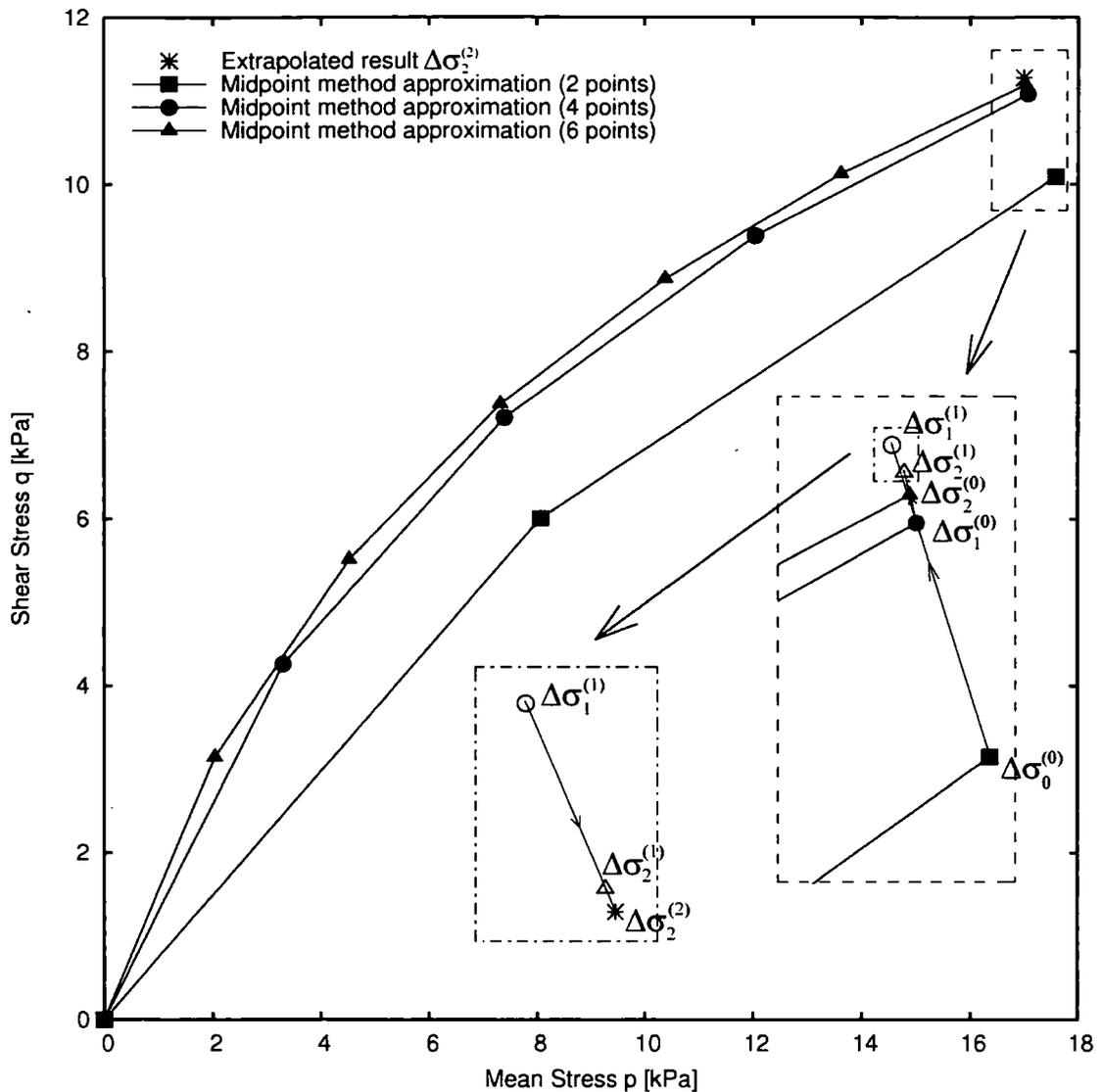
Figure 6.2. Extrapolation method: stress increments integrated with 2, 4 and 6 subincrements ($\Delta\sigma_0^{(0)}$, $\Delta\sigma_1^{(0)}$ and $\Delta\sigma_2^{(0)}$) are extrapolated to obtain $\Delta\sigma_1^{(1)}$ and $\Delta\sigma_2^{(1)}$. Those stress increments are used to obtain final, most accurate stress increment $\Delta\sigma_2^{(2)}$.

The Runge-Kutta Midpoint method has been chosen instead of the Modified Midpoint method (which is the method of choice as advised in Lambert 1973, Deuflhard and Bornemann 2002, Stoer and Bulirsch 2002) due to convergency problems with the Modified Midpoint method. However, the use of the Modified Midpoint method is advisable whenever it is possible, as it is theoretically more correct (the Runge-Kutta midpoint method only approximately satisfies the requirements for 6.18 whereas the Modified Midpoint method has the error expansion in the form of 6.20, see Deuflhard and Bornemann 2002 for a proof) and its rate of convergence should be higher. Despite

that, the Runge-Kutta Midpoint method has been successfully used with rule (6.18), exactly as the Modified Midpoint method would be used.

6.2.4. Error control methods

The accuracy of the stress integration algorithm is pivotal for the performance of reliable finite element simulations. As such, it is advantageous to identify an error control method that would guarantee that the numerical stress integration will always be within the accuracy set by the user. Such a method seems to be the Error per Unit Step (EPUS) error control method (e.g. Shampine 1994). In this approach the error estimate of a quantity must be below the percentage of this quantity integrated in the same substep. In the case of stress integration, to accept the result of Runge-Kutta integration, it is required that in a given subincrement

$$\|E(\delta\sigma)\| \leq TOL \cdot \|\delta\sigma\| \tag{6.27}$$

where $E(\delta\sigma)$ is the error estimate, TOL is the user defined tolerance and $\delta\sigma$ is the integrated stress subincrement (due to the strain subincrement $\delta\varepsilon$). If the error norm is too large, similarly as in the method described in Sloan (1987), the result is rejected and the subincrement size reduced. Otherwise the stress subincrement is deemed correct and added to the total stress. In each case the size of the new subincrement is calculated as (Shampine 1994)

$$\chi = \xi \sqrt[m-1]{\frac{TOL}{\frac{\|E(\delta\sigma)\|}{\|\sigma_0 + \delta\sigma\|}}} \tag{6.28}$$

Note that equation (6.28) is similar to equation (6.9). One difference lies in the order of the root, which is equal to the order of the Runge-Kutta method reduced by one. This is why, for the EPUS error control method, a Runge-Kutta method of higher order than two (preferably fifth order) is advisable.

Additionally, in some cases the stress subincrement corresponding to the strain subincrement may be very small. Then, due to possible division by zero, calculation of the substep size from (6.28) is ineffective and may lead to an infinite loop and general instability of the algorithm. A way of dealing with this problem must be included in the stress integration procedure.

109

A comparison of the efficiency and accuracy of the Runge-Kutta methods and the extrapolation method, when coupled either with EPS or EPUS error control is given in chapter 7.

6.3. Stress integration for the BBM

As mentioned in the section 6.2.1, the development of a stress-strain integration algorithm for the Barcelona Basic Model (BBM) requires creation of non square 6x7 elastic and elasto-plastic matrices due to the introduction of soil suction. It is possible to condense the non square 6x7 matrix to a square 6x6 matrix, just by introducing a dependence of the bulk modulus K on suction or by modifying the input strains. Such a solution is, however, not so clear and elegant, given that the dependency on soil suction is hidden among mechanical strains.

Note that the Barcelona Basic Model is formulated using mean net stress p. In this model the stresses referred to are the net stresses yet here they are often described simply as stresses.

6.3.1. Elastic procedure

Calculation of a stress increment resulting from a purely elastic strain increment requires a different algorithm with respect to the integration of an elasto-plastic strain increment. The application of Runge–Kutta schemes and the extrapolation method is limited in this work to the integration of elasto-plastic increments, as the solution in the elastic domain can be obtained in a closed form. The algorithms for the Runge-Kutta schemes and extrapolation method proposed in this work assume therefore that the initial stress state satisfies the yield locus equation. Thus, if the initial stress state lies inside the yield surface or initial elastic unloading occurs, then the elastic portion of the stress increment needs to be calculated first.

The elastic procedure created for the Barcelona Basic Model is similar to the one described by Sheng et al. (2000). Initially, a normalised yield locus needs to be derived to allow for a definition of a constant yield surface tolerance. The BBM mean net stress p and shear stress q are normalised by dividing it by (p_0+ks) a sum of preconsolidation stress and a shift of the yield locus due to suction (see also Fig. 4.1) to obtain the normalised stresses p' and q'. The normalised yield locus thus reads as

110

$$F_n = \left(\frac{q}{p_0 + ks}\right)^2 - M^2 \left(\frac{p + ks}{p_0 + ks}\right)\left(\frac{p_0 - p}{p_0 + ks}\right) = (q')^2 - M^2(p')(1 - p') = 0 \qquad (6.29)$$

This corresponds to an ellipse with a major and minor axis being unity and half M respectively. On such a modified yield locus, a single value of tolerance has been used. Thus, throughout the algorithm it is assumed that the stress state is on the yield locus. That is, the absolute value of function F_n for given stress state and hardening parameters is smaller than a user specified tolerance.

Following the approach by Sheng et al. (2000), a procedure that uses a closed form solution has been designed to calculate the elastic stress increment. The procedure involves the determination of a secant elasto-plastic matrix which, after multiplication by the strain, gives the correct (elastic) stress increment. This secant elasto-plastic matrix may either be square, where suction is incorporated into the strain increment used for stress computation, or has a rectangular shape, where suction will lead to a computation of corrections to the stresses.

As the stress integration algorithm operates in full stress space, it is necessary to extend the BBM formulation from the p-q space into full six dimensional stress space. In general net stress space, the shear stress q is proportional (by a factor of $\sqrt{3}$) to the second invariant J_{2D} of net stresses

$$
\begin{aligned}
q &= \sqrt{\frac{1}{2}\left((\sigma_{11} - \sigma_{22})^2 + (\sigma_{11} - \sigma_{33})^2 + (\sigma_{22} - \sigma_{33})^2 + 6(\sigma_{12}^2 + \sigma_{13}^2 + \sigma_{23}^2)\right)} = \\
&= \sqrt{\frac{3}{2}(\sigma_{ij} - \delta_{ij}p)(\sigma_{ij} - \delta_{ij}p)} = \sqrt{3} \cdot J_{2D} \qquad i, j = 1,2,3
\end{aligned}
\qquad (6.30)
$$

where δ_{ij} is the Kronecker delta. Similarly, the mean net stress p is is proportional (by a factor of a third) to the first invariant of net stresses J_1

$$p = \frac{1}{3}(\sigma_{11} + \sigma_{22} + \sigma_{33}) = \frac{1}{3}J_1 \qquad (6.31)$$

In the algorithm, a circular cross section in a plane perpendicular to the mean net stress axis of the yield locus has been assumed. Such a cross section is inferior to the surface proposed by Nakai or Mohr-Coulomb. The decision to use a circular cross-section in the deviatoric plane was adopted to simplify the algorithm.

In the BBM, the elastic change of specific volume Δv_s due to suction is computed as

$$\Delta v_s = \kappa_s \ln \frac{s + p_{at} + \Delta s}{s + p_{at}}$$

where p_{at} is the atmospheric pressure, κ_s is the elastic stiffness parameter associated with changes in suction, s is the initial value of suction and Δs is the suction increment. The suction change is therefore related to the elastic volumetric strain through

$$\Delta\varepsilon_{v,s} = -\int \frac{dv_s}{v} = -\ln \frac{v + \Delta v_s}{v} = -\ln \left(1 + \frac{\kappa_s \ln \frac{s + p_{at} + \Delta s}{s + p_{at}}}{v} \right)$$

which for small changes in specific volume Δv_s reduces to

$$\Delta\varepsilon_{v,s} = -\frac{\kappa_s}{v} \ln \frac{s + p_{at} + \Delta s}{s + p_{at}} \tag{6.32}$$

where v denotes the initial specific volume. Such an approximation to the small change of the specific volume is acceptable in most engineering applications and often assumed (Borja 1992, Sheng et al. 2000).

Having computed the part of the elastic volumetric strain due to suction, this elastic strain needs to be deducted from the given volumetric strain (6.34). Having made this deduction, we are left with the volumetric strain needed for the calculation of the stress increments. Because the effect of suction is assumed to be the same in all directions, the strain components $\varepsilon_{11}, \varepsilon_{22}, \varepsilon_{33}$ associated with a change of stress are computed by subtracting a third of the volumetric strain due to suction from the corresponding total strain components which leads to (6.37). The alternative approach involves leaving the strain components unchanged, but changing the terms within the matrix so they depend on the change of suction, which leads to (6.38).

Finally one can calculate a correction to the stress state obtained using just strain by a component using suction. For such a calculation suction is treated as an additional strain component. The terms in the matrix corresponding to the suction have some dependence on the other matrix terms, in particular the bulk modulus, which leads to (6.39). The derivation of (6.37) - (6.39). is shown in detail below.

The total change in volumetric strain is defined as a sum of changes of volumetric strains due to suction and mean net stress

$$\Delta\varepsilon_v = \Delta\varepsilon_{v,p} + \Delta\varepsilon_{v,s} = -\frac{\kappa}{v}\ln\frac{p+\Delta p}{p} - \frac{\kappa_s}{v}\ln\frac{s+\Delta s+p_{at}}{s+p_{at}}$$ (6.33)

To calculate the change of the mean net stress Δp, the part of strains corresponding to mechanical loading is computed as

$$\Delta\varepsilon_{v,p} = \Delta\varepsilon_v - \Delta\varepsilon_{v,s}$$ (6.34)

The change of mean net stress Δp is then equal to

$$\Delta p = p\left(e^{-\frac{v}{\kappa}d\varepsilon_{v,p}} - 1\right)$$ (6.35)

and the secant bulk modulus is therefore defined as

$$K_p = \frac{\Delta p}{\Delta\varepsilon_{v,p}} = -\frac{p\left(e^{-\frac{v}{\kappa}d\varepsilon_{v,p}} - 1\right)}{\Delta\varepsilon_{v,p}} \quad \text{or} \quad K = \frac{\Delta p}{\Delta\varepsilon_v} = -\frac{p\left(e^{-\frac{v}{\kappa}d\varepsilon_{v,p}} - 1\right)}{\Delta\varepsilon_v}$$ (6.36)

Now the stress increment may be calculated as

$$\Delta\sigma = \frac{1}{3}\begin{bmatrix} 3K_p+4G & 3K_p-2G & 3K_p-2G & 0 & 0 & 0 \\ 3K_p-2G & 3K_p+4G & 3K_p-2G & 0 & 0 & 0 \\ 3K_p-2G & 3K_p-2G & 3K_p+4G & 0 & 0 & 0 \\ 0 & 0 & 0 & 3G & 0 & 0 \\ 0 & 0 & 0 & 0 & 3G & 0 \\ 0 & 0 & 0 & 0 & 0 & 3G \end{bmatrix} \cdot \begin{Bmatrix} \Delta\varepsilon_{11,p} \\ \Delta\varepsilon_{22,p} \\ \Delta\varepsilon_{33,p} \\ \Delta\varepsilon_{12} \\ \Delta\varepsilon_{13} \\ \Delta\varepsilon_{23} \end{Bmatrix}$$ (6.37)

where the $\varepsilon_{ii,p}$ are the given value of strain to integrate, reduced by a third of the strain caused by the suction change. The same stress increment may be computed as

$$\Delta\sigma = \frac{1}{3}\begin{bmatrix} 3K+4G & 3K-2G & 3K-2G & 0 & 0 & 0 \\ 3K-2G & 3K+4G & 3K-2G & 0 & 0 & 0 \\ 3K-2G & 3K-2G & 3K+4G & 0 & 0 & 0 \\ 0 & 0 & 0 & 3G & 0 & 0 \\ 0 & 0 & 0 & 0 & 3G & 0 \\ 0 & 0 & 0 & 0 & 0 & 3G \end{bmatrix} \cdot \begin{Bmatrix} \Delta\varepsilon_{11} \\ \Delta\varepsilon_{22} \\ \Delta\varepsilon_{33} \\ \Delta\varepsilon_{12} \\ \Delta\varepsilon_{13} \\ \Delta\varepsilon_{23} \end{Bmatrix}$$ (6.38)

Finally, one can reformulate equation (6.37) above and instead of manipulating strains, add suction as an extra component in the strain vector and a further column in the matrix.

$$\Delta\sigma = \frac{1}{3}\begin{bmatrix} 3K_p+4G & 3K_p-2G & 3K_p-2G & 0 & 0 & 0 & -\dfrac{9\cdot K_p}{K_s} \\[2mm] 3K_p-2G & 3K_p+4G & 3K_p-2G & 0 & 0 & 0 & -\dfrac{9\cdot K_p}{K_s} \\[2mm] 3K_p-2G & 3K_p-2G & 3K_p+4G & 0 & 0 & 0 & -\dfrac{9\cdot K_p}{K_s} \\[2mm] 0 & 0 & 0 & 2G & 0 & 0 & 0 \\[1mm] 0 & 0 & 0 & 0 & 2G & 0 & 0 \\[1mm] 0 & 0 & 0 & 0 & 0 & 2G & 0 \end{bmatrix}\cdot\begin{Bmatrix} \Delta\varepsilon_{11} \\ \Delta\varepsilon_{22} \\ \Delta\varepsilon_{33} \\ \Delta\varepsilon_{12} \\ \Delta\varepsilon_{13} \\ \Delta\varepsilon_{23} \\ \Delta s \end{Bmatrix} \quad (6.39)$$

where

$$K_s = \frac{\Delta s}{\Delta\varepsilon_v^s} = \frac{\Delta s}{\Delta\varepsilon_v^s} = \frac{\Delta s}{\dfrac{\kappa_s}{\nu}\ln\left(\dfrac{s_0 + p_{at} + \Delta s}{s_0 + p_{at}}\right)} \quad (6.40)$$

The result of calculations is clearly the same in all three cases. Equation (6.39) can be written used an enhanced strain vector $\Delta\varepsilon^{enh} = \{\Delta\varepsilon_{11}, \Delta\varepsilon_{22}, \Delta\varepsilon_{33}, \Delta\varepsilon_{12}, \Delta\varepsilon_{13}, \Delta\varepsilon_{23}, s\}^T$ as

$$\Delta\sigma = D_{sec}\Delta\varepsilon^{enh} \quad (6.41)$$

To compute the elasto-plastic part of the strain increment with an explicit integration method, it is first necessary to calculate the purely elastic part for each strain increment. This task is achieved here by using the Pegasus algorithm modified to suit the needs of the BBM. The Pegasus algorithm was initially proposed by Dowell and Jarratt (1972) and then used for similar tasks by e.g. Potts and Zdravkovic (1999) and Sloan et al. (2001). The Pegasus algorithm is employed to solve the problem of finding the parameter α such that that the elastic portion of the strain increment is defined as $\Delta\varepsilon_{el} = \alpha\Delta\varepsilon^{enh}$. This approach leads to an elasto-plastic stress increment starting from the updated stress state σ_α on the yield surface, for which the yield function is equal to zero, i.e. $F(\sigma_\alpha)=0$.

The Pegasus algorithm is used only when part of the step is elasto-plastic. Thus, the value of α is in range $0 = \alpha_0 \le \alpha \le \alpha_1 = 1$.

If the yield function were linear, then the correct value of α would be

$$\alpha = \frac{F(\sigma_0)}{F(\sigma_0) - F(\sigma_0 + \Delta\sigma)} = \frac{F_0}{F_0 - F_1} \quad (6.42)$$

where $F(\boldsymbol{\sigma}_0)$ is the value of the yield function corresponding to the initial stress ($\alpha = 0$) and $F(\boldsymbol{\sigma}_0 + \Delta\boldsymbol{\sigma}) = F(\boldsymbol{\sigma}_0 + \mathbf{D}_{sec}\Delta\boldsymbol{\varepsilon}^{enh})$ is the value of the yield function corresponding to $\alpha = 1$. However, in the BBM, the yield function is not linear (and appears not to be solvable in a closed form), yet (6.42) may be used as an approximation of the solution. Then the stress state for the computed α is calculated and new lower or upper bound are set, depending on the value of the yield function. The value of the new bound for α is computed as

if $F\left(\boldsymbol{\sigma}_0 + [\alpha_0 + \alpha(\alpha_1 - \alpha_0)]\mathbf{D}_{sec}\Delta\boldsymbol{\varepsilon}^{enh}\right) > 0$

then $F_1 = F\left(\boldsymbol{\sigma}_0 + [\alpha_0 + \alpha(\alpha_1 - \alpha_0)]\mathbf{D}_{sec}\Delta\boldsymbol{\varepsilon}^{enh}\right)$ and $\alpha_{1,new} = \alpha_0 + \alpha(\alpha_1 - \alpha_0)$

if $F\left(\boldsymbol{\sigma}_0 + [\alpha_0 + \alpha(\alpha_1 - \alpha_0)]\mathbf{D}_{sec}\Delta\boldsymbol{\varepsilon}^{enh}\right) < 0$

then $F_0 = F\left(\boldsymbol{\sigma}_0 + [\alpha_0 + \alpha(\alpha_1 - \alpha_0)]\mathbf{D}_{sec}\Delta\boldsymbol{\varepsilon}^{enh}\right)$ and $\alpha_{0,new} = \alpha_0 + \alpha(\alpha_1 - \alpha_0)$

The next step of the algorithm is performed exactly in the same way, with the value of α_0 or α_1 being substituted by $\alpha_{0,new}$ or $\alpha_{1,new}$ respectively. The value of the elastic portion of strain is assumed to have been found once the calculated value of the yield function F lies within a required tolerance. This algorithm is unconditionally stable as only one cross-section with the yield locus is possible (the effect of a non-convex yield locus as mentioned by Wheeler et al (2002) is not accounted for; though the warning of the choice of parameters resulting in such a yield locus is given by the algorithm).

The above algorithm tends to slow down in the case of a large strain increment. In such situations only one bound (usually α_0) is modified during interations while the other remains unchanged (see Fig. 6.3 which shows the first two iterations of the Pegasus algorithm).
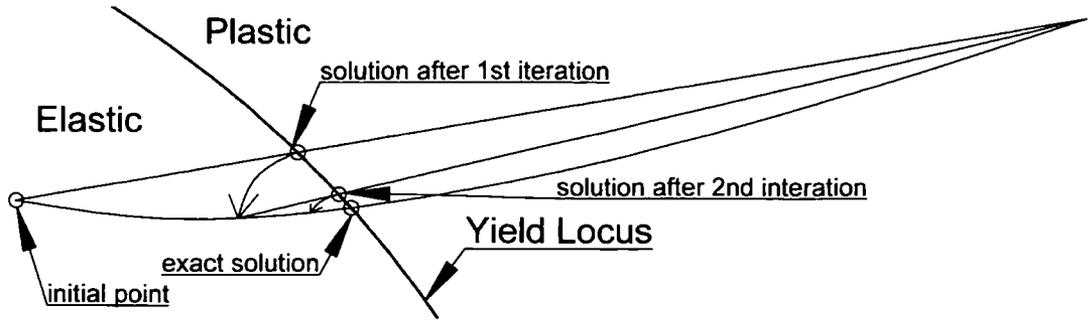
Figure 6.3. Graphical illustration of the first two iterations of Pegasus algorithm

To improve the efficiency of the algorithm an additional check on the value of α is made. If the current guess for α is smaller than 0.01 or larger than 0.99, then an additional correction to the alpha is made: 0.05 is added or subtracted respectively. It has been found that such a check greatly improves the rate of convergence.

The final problem involves catering for the strain increments initiated for the stress state on the yield locus leading to initial elastic unloading and further elasto-plastic loading of soil. This situation is indicated by the tangent stress increment pointing inwards the yield locus. It is easy to check for this, as the scalar product of the tangent stress increment (obtained by multiplying the tangent elastic matrix by the strain increment) and yield surface gradient will be negative.

$$\text{if } \quad \frac{\partial F}{\partial \sigma} \mathbf{D}_{el} \Delta \varepsilon^{enh} < 0 \rightarrow \text{ elastic unloading present} \qquad (6.43)$$

where $\mathbf{D}_{el}$ is the tangent elastic matrix. The tangent elastic matrix is similar to the matrix given by (6.39), but is computed with bulk moduli K and K_s

$$K = \frac{pv}{\kappa_p} \qquad K_s = p \frac{\kappa_s v^2}{\kappa_p (s + p_{at})}$$

so

$$\frac{K_s}{K_p} = \frac{v(s + p_{at})}{\kappa_s} \qquad (6.44)$$

In the equations above, the values of mean net stress and suction correspond to the initial values of those quantities.

For finding the intersection with the yield locus during these unloading-loading cases, the same Pegasus algorithm was used. However, the problem to overcome is that the algorithm would report initial convergence, as the initial stress state is on the yield locus

116

within tolerance. This has been solved by initially setting the yield locus tolerance to a smaller value, so the initial state does not lie on the yield locus anymore. However, this solution works only when the initial state lies on the inside of the yield locus (see Fig. 6.4, top) In case the initial stress state lies outside of the yield locus, the tolerance is set to a smaller value and a small quantity is subtracted from the value of the yield function (so that the value of yield function corresponds to the function inside the yield locus). The subtracted quantity and temporary tolerance is such that the final value of the yield function will lead to a stress state being on the yield locus within the original tolerance (see Fig. 6.4, bottom).
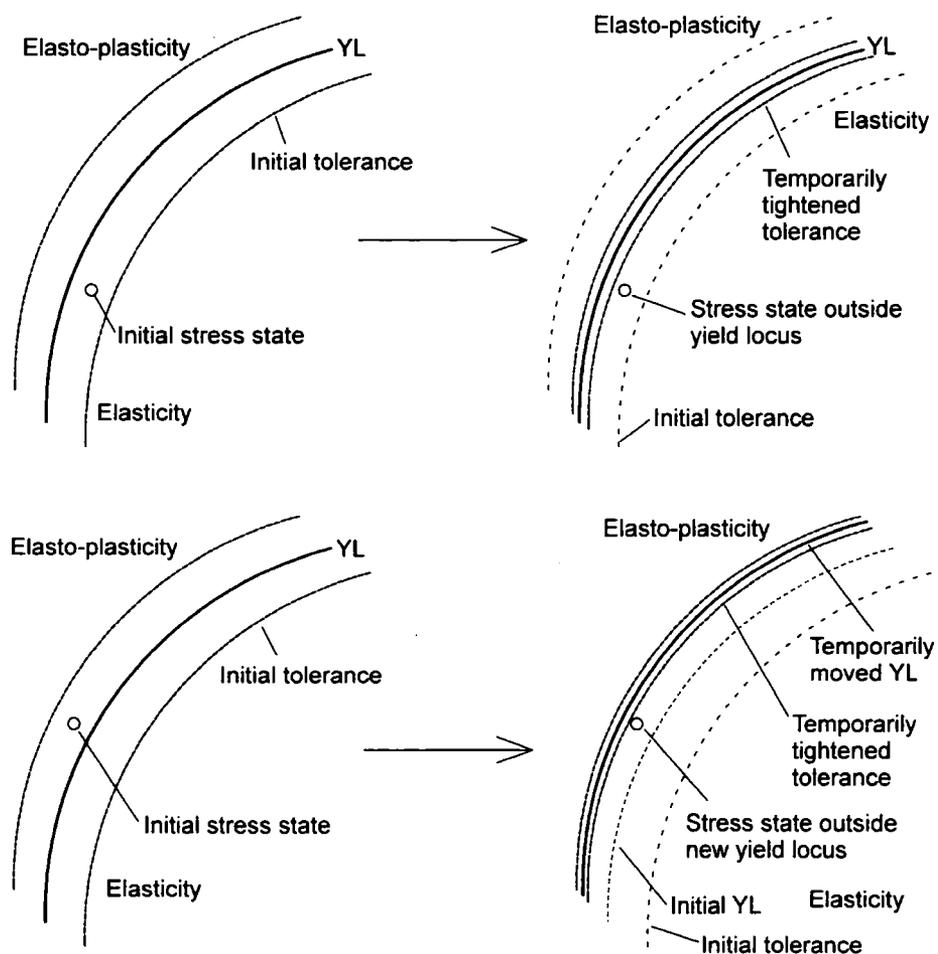
Figure 6.4. Graphical illustration of the modification of the yield tolerance during unloading-loading case for the Pegasus algorithm. Yield tolerance modified when the initial stress state lies on the elastic side of the yield locus (top). Yield tolerance modified and yield locus temporarily moved when the initial stress state lies on the elasto-plastic side of the yield locus (bottom).

117

6.3.2. Computation of elasto-plastic matrix and drift correction

Having calculated the stress increment associated with the purely elastic response, the remaining part of the subincrement will be elasto – plastic. The stress increment corresponding to that part of the strain increment is calculated using an explicit stress integration scheme with subincrementation (substepping) and error control. For such schemes, it is necessary to calculate the elasto-plastic tangent matrix $\mathbf{D}^{ep}$. This matrix is derived below.

The yield function F and plastic potential G are defined in terms of the net stress $\boldsymbol{\sigma}$, suction s and the hardening parameter p_0^* as

$$F = F(\boldsymbol{\sigma}, s, p_0^*) = 0 \qquad (6.45)$$

$$G = G(\boldsymbol{\sigma}, s, p_0^*) = 0 \qquad (6.46)$$

Through the flow rule, the plastic strain change is dependent on the stress derivative of the plastic potential

$$d\boldsymbol{\varepsilon}^{pl} = \Lambda \frac{\partial G(\boldsymbol{\sigma}, s, p_0^*)}{\partial \boldsymbol{\sigma}} \qquad (6.47)$$

where Λ is the plastic multiplier. The volumetric plastic strain increment $d\varepsilon_v^{pl} = d\varepsilon_{11}^{pl} + d\varepsilon_{22}^{pl} + d\varepsilon_{33}^{pl}$ is related to a change of the hardening parameter p_0^* according to the following equation

$$dp_0^* = \frac{\partial p_0^*}{\partial \varepsilon_v^{pl}} d\varepsilon_v^{pl} \qquad (6.48)$$

The consistency condition to be satisfied by all infinitesimal quantities is

$$dF = \left(\frac{\partial F}{\partial \boldsymbol{\sigma}}\right)^T d\boldsymbol{\sigma} + \left(\frac{\partial F}{\partial s}\right)^T ds + \left(\frac{\partial F}{\partial p_0^*}\right)^T dp_0^* = 0 \qquad (6.49)$$

The differential form of the stress – strain relationship for the BBM, is given by

$$d\boldsymbol{\sigma} = \mathbf{D}^{el} d\boldsymbol{\varepsilon}^{el} = \mathbf{D}^{el}\left(d\boldsymbol{\varepsilon} - d\boldsymbol{\varepsilon}^{pl} - \frac{1}{3}\mathbf{m}\frac{\kappa_s ds}{(p_{at} + s)v}\right) \qquad (6.50)$$

where $\mathbf{D}^{el}$ is the elastic tangent matrix calculated at the beginning of the increment, $d\varepsilon$ is the strain increment, $d\varepsilon^{pl}$ is the plastic component of the strain increment, κ_s is the

swelling parameter associated to suction change and p_{at} is atmospheric pressure. Introducing (6.47) into (6.50) gives

$$d\mathbf{\sigma} = \mathbf{D}^{el}d\mathbf{\epsilon} - \Lambda\mathbf{D}^{el}\frac{\partial G(\mathbf{\sigma},s,p_0^*)}{\partial\mathbf{\sigma}} - \frac{1}{3}\mathbf{D}^{el}\mathbf{m}\frac{\kappa_s ds}{(p_{at}+s)\nu} \qquad (6.51)$$

After introducing (6.51) into (6.49) and recognising that the transpose of a scalar variable coincides with the scalar variable itself, the following relationship is obtained

$$\left(\frac{\partial F}{\partial\mathbf{\sigma}}\right)^{T}\left(\mathbf{D}_{el}d\mathbf{\epsilon} - \mathbf{D}_{el}\frac{\partial G(\mathbf{\sigma},s,p_0^*)}{\partial\mathbf{\sigma}}\Lambda - \frac{1}{3}\mathbf{D}_{el}\mathbf{m}\frac{\kappa_s ds}{(p_{at}+s)\nu}\right) + \frac{\partial F}{\partial s}ds + \frac{\partial F}{\partial p_0^*}dp_0^* = 0 \quad (6.52)$$

As dp_0^* is a function of the plastic volumetric strain increment as indicated in (6.48), then

$$\left(\frac{\partial F}{\partial p_0^*}\right)dp_0^* = \left(\frac{\partial F}{\partial p_0^*}\right)\left(\frac{\partial p_0^*}{\partial\epsilon_v^{pl}}\right)d\epsilon_v^{pl} \qquad (6.53)$$

and, after expressing $d\epsilon_v^{pl}$ as

$$d\epsilon_v^{pl} = \sum_{i=1}^{3}d\epsilon_{ii}^{pl} = \Lambda\mathbf{m}^{T}\left(\frac{\partial G(\mathbf{\sigma},s,p_0^*)}{\partial\mathbf{\sigma}}\right) \qquad (6.54)$$

the following result is obtained

$$\left(\frac{\partial F}{\partial p_0^*}\right)dp_0^* = \Lambda\left(\frac{\partial F}{\partial p_0^*}\right)\left(\frac{\partial p_0^*}{\partial\epsilon_v^{pl}}\right)\mathbf{m}^{T}\left(\frac{\partial G(\mathbf{\sigma},s,p_0^*)}{\partial\mathbf{\sigma}}\right) \qquad (6.55)$$

After introducing (6.55) into (6.52), Λ can be expressed as

$$\Lambda = \frac{\mathbf{a}^{T}\mathbf{D}^{el}d\mathbf{\epsilon} + \left[c - \mathbf{a}^{T}\mathbf{D}^{el}\mathbf{b}\right]ds}{\mathbf{a}^{T}\mathbf{D}^{el}\mathbf{g} - d} \qquad (6.56)$$

where

$$\mathbf{a} = \frac{\partial F}{\partial\mathbf{\sigma}}, \quad \mathbf{b} = \frac{1}{3}\mathbf{m}\frac{\kappa_s}{p_{at}+s}, \quad c = \frac{\partial F}{\partial s}, \quad d = \frac{\partial F}{\partial p_0^*}\frac{\partial p_0^*}{\partial\epsilon_v^{pl}}\mathbf{m}^{T}\frac{\partial G}{\partial\mathbf{\sigma}}, \quad \mathbf{g} = \frac{\partial G}{\partial\mathbf{\sigma}}$$

Having calculated the scalar plastic multiplier Λ, the infinitesimal stress increment is then equal to

$$d\mathbf{\sigma} = \mathbf{D}^{el}d\mathbf{\epsilon}^{el} = \mathbf{D}^{el}\left(d\mathbf{\epsilon} - d\mathbf{\epsilon}^{pl} - d\mathbf{\epsilon}^{s}\right) = \mathbf{D}^{el}d\mathbf{\epsilon} - \Lambda\mathbf{D}^{el}\frac{\partial G(\mathbf{\sigma},s,p_0^*)}{\partial\mathbf{\sigma}} - \frac{1}{3}\mathbf{D}^{el}\mathbf{m}\frac{\kappa_s ds}{p_{at}+s}$$

substituting (6.56) in to the above gives

$$d\sigma = D^{el}d\varepsilon - D^{el}g\frac{a^TD^{el}d\varepsilon + \left[c - a^TD^{el}b\right]ds}{a^TD^{el}g - d} - \frac{1}{3}D^{el}m\frac{\kappa_s ds}{p_{at} + s}$$

which leads to

$$d\sigma = \left(D^{el} - \frac{D^{el}ga^TD^{el}}{a^TD^{el}g - d}\right)d\varepsilon + \left(D^{el}g\frac{\left(c - a^TD^{el}b\right)}{a^TD^{el}g - d} - \frac{1}{3}D^{el}m\frac{\kappa_s}{p_{at} + s}\right)ds$$

This can be simplified to

$$d\sigma = D^{ep,eps}d\varepsilon + D^{ep,s}ds = D^{ep}d\varepsilon^{enh} \qquad (6.57)$$

where

$d\varepsilon^{enh} = \{d\varepsilon, ds\}^T = \{d\varepsilon_{11}, d\varepsilon_{22}, d\varepsilon_{33}, d\varepsilon_{12}, d\varepsilon_{13}, d\varepsilon_{23}, ds\}^T$, $D^{ep,eps} = D^{el} - \dfrac{D^{el}ga^TD^{el}}{a^TD^{el}g - d}$ is a 6x6

matrix and $D^{ep,s} = D^{el}g\dfrac{\left(c - a^TD^{el}b\right)}{a^TD^{el}g - d} - \dfrac{1}{3}D^{el}m\dfrac{\kappa_s}{p_{at} + s}$ is a column matrix.

The 6x7 elasto-plastic matrix D^{ep} can be reduced to the square 6x6 form, similar as for pure elasticity (see section 6.3.1). The rule to be followed in such a transformation is that the resulting stresses must be the same as obtained from the 6x7 matrix. Thus the product of $D^{ep,s}ds$ must be added to the result of multiplication $D^{ep,eps}d\varepsilon$. This can be achieved by modifying the strains $d\varepsilon$ (obtaining $d\varepsilon^{(mod)}$) so

$$d\sigma = D^{ep,eps}d\varepsilon + D^{ep,s}ds = D^{ep,eps}d\varepsilon^{(mod)} \qquad (6.58)$$

To obtain the modified strains, the strains $d\varepsilon_{11}$, $d\varepsilon_{22}$, $d\varepsilon_{33}$ should be altered by the same amount (the suction acts isotropic). Another possibility is to modify the $D^{ep,eps}$ matrix (to obtain $D^{ep\,(mod)}$) so

$$d\sigma = D^{ep,eps}d\varepsilon + D^{ep,s}ds = D^{ep(mod)}d\varepsilon \qquad (6.59)$$

To obtain $D^{ep\,(mod)}$ only the three first elements the diagonal should be modified. Unfortunately, both of these solutions required knowledge of relative amounts of suction and strain increments before calculations of the relevant matrix and thus are inelegant.

The additional problem that must be addressed in the explicit stress integration is the problem of drift correction. The drift correction algorithm used has been described in section 6.1.4. Here it will be described in detail for the case of BBM.

The stress state is said to drift from the yield locus and needs to be corrected back with a drift correction algorithm when, after integrating the stress, the final stress state is not on the yield surface within the requested tolerance (however as the whole subincrement was elasto-plastic, it should be).

Before integration of a subincrement, the initial stress state σ_A lies on the yield locus at point A, that is $F(\sigma_A, s_A, p_{0(A)}^*) = 0$. After calculating the stress increase $\delta\sigma$, as explained in the previous section, the stress state changes to $\sigma_B = \sigma_A + \delta\sigma$ moving to point B. This will no longer be on the yield locus, i.e. $F(\sigma_B, s_B, p_{0(B)}^*) \neq 0$. The drift correction algorithm imposes a change of the elastic strain $\delta\varepsilon^e$ (by maintaining unchanged the total strain increment $\delta\varepsilon$, i.e. $\delta\varepsilon^e = -\delta\varepsilon^{pl}$), which results in the correction of the stress state to point C lying on the yield locus. The yield locus equation after correction will therefore be

$$F(\sigma_C, s, p_{0C}^*) = F(\sigma_B + \delta\sigma_{drift}, s, p_{0B}^* + \delta p_0^*) = 0 \qquad (6.60)$$

where $\Delta\sigma$ and δp_0^* are the corrections to the stress state and hardening parameter respectively and no correction to suction is applied as explained below.

After expanding (6.60) in Taylor series we obtain

$$F(\sigma_C, s, p_{0C}^*) = F(\sigma_B, s, p_{0B}^*) + \left(\frac{\partial F}{\partial \sigma}\right)^T \delta\sigma_{drift} + \frac{\partial F}{\partial s}\delta s + \frac{\partial F}{\partial p_0^*}\delta p_0^* + \dots \qquad (6.61)$$

where the stress change $\delta\sigma_{drift}$ is

$$\Delta\sigma_{drift} = \Delta\sigma_{drift}(\delta\varepsilon^{el}) = D^{el}\delta\varepsilon^{el} = -D^{el}\delta\varepsilon^{pl} = -D^{el}\Lambda\frac{\partial G}{\partial \sigma} \qquad (6.62)$$

After substituting (6.62) and (6.55) into (6.61), neglecting second order terms and above and noticing that the change of suction δs is equal to zero (as suction change is proportional to the variation of strain $\delta\varepsilon$ which remains unchanged) the following expression for λ is obtained

$$\Lambda = \frac{F(\sigma_B, s, p_{0B}^*)}{\left(\frac{\partial F}{\partial \sigma}\right)^T D^{el}\frac{\partial G}{\partial \sigma} - \frac{\partial F}{\partial p_0^*}\frac{\partial p_0^*}{\partial \varepsilon^{pl}}m^T\frac{\partial G(\sigma, s, p_0^*)}{\partial \sigma}} \qquad (6.63)$$

The stress state in point C is then equal to

$$\sigma_C = \sigma_B - \Lambda \mathbf{D}^{el} \frac{\partial G}{\partial \sigma} \qquad (6.64)$$

In the unlikely situation when, after the first correction, the stress state still lies outside the yield locus, the above algorithm is performed again until the stress state is mapped back onto the yield locus within the set tolerance. During tests it appeared that the algorithm is more stable when the derivatives are computed at point B. Note, however, that drift correction after calculating the subincrement should be rather an exception than a rule, as the results should be accurate enough to be within set tolerance from the yield locus. If drift correction is performed too often it slows down the algorithm. To overcome this once can consider increasing the integration tolerance (it will be shown in the subsequent chapter that this may even increase the overall speed of algorithm) or increase the tolerance at which it is assumed that the stress state is still on the yield locus.

6.3.3. Stress integration with Runge – Kutta and extrapolation

The Runge-Kutta integration for the BBM follows the scheme for the general case presented in section 6.1.2. The method is started with an attempt to compute the stress increment due to the whole strain increment in one step. If this is unsuccessful (the error is too large), the strain increment is divided into subincrements and for each subincrement the stress increment is calculated. The stress in each subincrement may be calculated in several stages, depending on the specific Runge-Kutta method. The stress for each stage of the method is computed using (6.57) with initial conditions as required by (6.7). After computing the stress for each stage of the Runge-Kutta method, the error is assessed and the subincrement size is modified. The whole change of stress due to drift correction (performed as in 6.3.2) is added to the error of the method. The stress integration is finished when the whole strain increment is covered.

The stress integration with the extrapolation method is performed as described in section 6.2.3. Again, the required elasto-plastic matrix is calculated with (6.57). The stress state is checked for being within the tolerance of the yield surface; however seldom any drift correction is required. If such a case arises then the whole change of stress due to drift correction is added to the error measure and possibly an additional iteration of the method is required.

6.4. Stress integration for a multi-cell enhanced model

In this section a stress integration algorithm for the multi-cell enhanced model is presented. The algorithm is kept general, i.e. it can be used for any model adopting a multi-cell extension as long as a stress integration algorithm for the model is given. However, it is likely that a more efficient algorithm for each specific model could be found. The following algorithm should be treated simply as a proof of concept.

The input to the stress integration algorithm is a change of strain $\Delta\varepsilon$ and a change of suction Δs. The change of strain in individual cells will differ from once cell to another; however the average of strain increments over all the cells must be equal to the supplied change of strain. Given n cells

$$\frac{1}{n}\sum_{c=1}^{n}\Delta\varepsilon_c = \Delta\varepsilon \quad c = 1,2,...,n \tag{6.65}$$

(subscript c denotes the c-th cell). On the other hand, the stress increment in each of the cells must be equal, so

$$\underset{c=1..n}{\forall}\ \Delta\sigma_c = \Delta\sigma \quad c = 1,2,...,n \tag{6.66}$$

In the proposed algorithm, initially, a distribution of suction in the cells is calculated, as the suction increment is known. The suction increment for every individual cell is known and constant (though not the same for all the cells) thus will not be changed during the iterations of the algorithm.

In the proposed procedure, the algorithm starts by computing the stress state $\sigma_i^{(1)}$ in all the cells with the stress integration procedure assuming that the strain increments are the same and equal to $\Delta\varepsilon$ for all the cells (superscript $^{(1)}$ denotes first iteration). The input suction change for given cell is constant and equal to the initially computed suction increment. After this initial stage, the stress distribution in all the cells is known and the stress in the c-th cell is $\sigma_c^{(1)}$. However, the stress distribution is likely to be unequal between the cells. Now, an average stress $\sigma_{av}^{(1)}$ can be computed as

$$\sigma_{av}^{(1)} = \frac{1}{n}\sum_{c=1}^{n}\sigma_c^{(1)} \tag{6.67}$$

and a correction stress for each of the cells as

$$\Delta\sigma_c^{(1)} = \sigma_{av}^{(1)} - \sigma_c^{(1)} \tag{6.68}$$

For each of the cells a corresponding elasto-plastic matrix $\mathbf{D}_c^{(1)}$ can be computed and its inverse will allow for the approximation to the strain correction required

$$\delta\varepsilon_c^{(1)} = \mathbf{D}_c^{(1)^{-1}}\Delta\sigma_c^{(1)} \tag{6.69}$$

Now, all the cells have constant stresses. Unfortunately, this will likely result in the average strain increment being different from the prescribed strain increment (i.e. the sum of all corrections $\delta\varepsilon_c^{(1)}$ will not be equal to zero). The average of unbalanced strains can be calculated as

$$\delta\varepsilon_{unb}^{(1)} = \frac{1}{n}\sum_{c=1}^{n}\delta\varepsilon_c^{(1)} \tag{6.70}$$

The aim of the subsequent part of the algorithm is to reach a situation when the average of the strain increments over all the cells is equal to the input strain increment, and the stress computed in each of the cells, using the tangent matrix, will be the same. After reaching this goal, the strains obtained are integrated and the error of integration is checked.

The balancing of the strains and stresses is achieved in relatively crude way. However, this part of the algorithm is relatively cheap, as it involves neither stress integration nor calculation of tangent matrices.

Out of all tangent matrices $\mathbf{D}_c^{(1)}$ that with minimum value of first component on the diagonal is chosen:

$$\mathbf{D}_{min}^{(1)} = \min\mathbf{D}_c^{(1)}[1,1] \quad c = 1,2,...,n \tag{6.71}$$

This matrix is likely to give the smallest changes in stress for the given strain increment. Now, the average unbalanced strain is multiplied by $\mathbf{D}_{min}^{(1)}$ and a correction to the stress state is computed

$$\delta\sigma = \mathbf{D}_{min}^{(1)}\delta\varepsilon_{unb}^{(1)} \tag{6.72}$$

This correction is generally small. The new stress state we aim for is

$$\sigma_{av}'^{(1)} = \sigma_{av}^{(1)} + \delta\sigma \tag{6.73}$$

For each cell a new correction for stresses follows

$$\Delta\sigma_c'^{(1)} = \sigma_{av}^{(1)} - \sigma_c^{(1)} \tag{6.74}$$

and strains may be computed

$$\delta\varepsilon_c'^{(1)} = \mathbf{D}_c^{(1)^{-1}} \Delta\sigma_c'^{(1)} \tag{6.75}$$

The new unbalanced average strain can be calculated as

$$\delta\varepsilon_{unb}'^{(1)} = \frac{1}{n}\sum_{c=1}^{n}\delta\varepsilon_c'^{(1)} \tag{6.76}$$

The steps (6.72) to (6.76) are repeated (each time with updated values of the average unbalanced strain) until the unbalanced strains satisfy the convergence requirements. The convergence requirements could be that this unbalanced strain is smaller than a given percentage of the strain increment of smaller than some predefined absolute value.

Once the unbalanced average strain is considered to be small enough, the stresses are integrated using the provided stress integration procedure for the given model (with the appropriate inner iteration of strains $\Delta\varepsilon_c'^{(1)}$ and suction increment) and a new stress state $\sigma_c^{(2)}$ is reached. The steps of the algorithm (equations 6.67 - 6.76) are now repeated until the differences in stress states in all the cells are within an acceptable tolerance. This iterative procedure is required as tangent matrices $\mathbf{D_c}$ were used during the calculations.

Convergence is reached when the average absolute difference in actual stress state and the average stress state in each of the stress components is smaller than a given for the last iteration (denoted last).

$$\frac{1}{n}\sum_{c=1}^{n}abs\left(\sigma_{av}^{(last)} - \sigma_c^{(last)}\right) \le \text{Tolerance} \tag{6.77}$$

If this convergence criterion is is not valid, another iteration of the algorithm is performed (unless the number of iterations becomes too large or the algorithm appears to diverge).

It is easy to modify this convergence condition so the average value of the stress state in all the cells must be close enough to the average stress state in relative terms

$$\frac{1}{n}\sum_{c=1}^{n}abs\left(\frac{\sigma_{av}^{(last)} - \sigma_c^{(last)}}{\sigma_{av}^{(last)}}\right) \le \text{Tolerance} \tag{6.78}$$

Another possible convergence criteria may require a stress state in each of the cells being close enough to the average stress value

$$\underset{c=1..n}{\forall} \quad \mathrm{abs}\left(\sigma_{av}^{(last)} - \sigma_c^{(last)}\right) \le \text{Tolerance} \qquad (6.79)$$

or within a percentage value of the average stress

$$\underset{c=1..n}{\forall} \quad \mathrm{abs}\left(\frac{\sigma_{av}^{(last)} - \sigma_c^{(last)}}{\sigma_{av}^{(last)}}\right) \le \text{Tolerance} \qquad (6.80)$$

Any of the equations (6.77) – (6.80) should be valid for each stress component. Note that in the case of a percentage tolerance, as given by (6.78) or (6.80), a further check on whether $\sigma_{av}^{(last)}$ is not too close to zero is necessary.

When the unbalanced stresses increase with the number of iterations of the algorithm, the procedure diverges. In such a case (or when no convergence has been reached after a given number of iterations), the given strain increment should be divided into smaller subincrements, which should be subsequently integrated.

Such simple substepping algorithm has been introduced and coded for the multi-cell version of the Barcelona Basic Model. In such an algorithm, if convergence is not reached after 10 iterations, the integrated strain increment is divided in two and the strain subincrements are subsequently integrated.

The described stress integration algorithm was used to integrate a multi-cell enhanced Barcelona Basic Model (with twenty cells, n=20). The model parameters were as given in 5.2.3, with an initial suction 200 kPa and initial hardening parameter p_0^* equal to 50 kPa. The strain increment corresponded to isotropic loading (increase of volumetric strain by 3%) and then oedometric loading. It was observed that to ensure convergence a fairly strict tolerance is helpful. Thus a tolerance of 0.01 kPa coupled with rule (6.77) was used. The results of integration are given in Fig. 6.5 and the maximum error in any stress component and error in stress as measured by (6.77) is presented in Fig. 6.6.
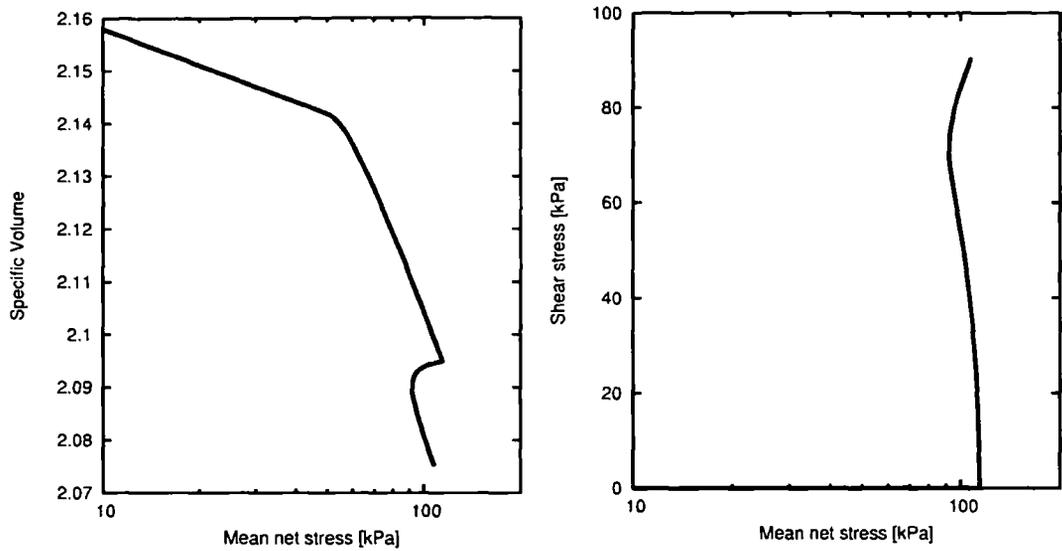
Figure 6.5. Stress integration: initial increment of 3% volumetric strain (as in isotropic loading) followed by 1% of ε_{11} increment (as in oedometric loading). Evolution of mean net stress versus specific volume (left) and mean net stress versus shear stress (right).
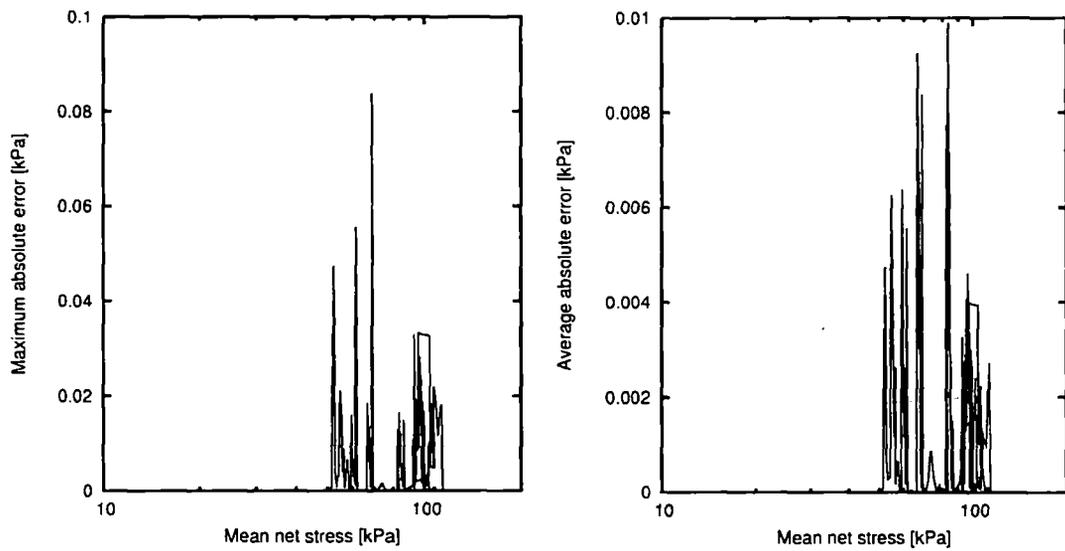
Figure 6.6. Error in integration shown in Fig. 6.5 (left) due to multi-cell enhancement. Maximum error among all stress components in all cells (measured against averaged stress over all the cells, left) and average error of non-zero stress components (measured against averaged stress over all the cells, right).

127

7. Testing and comparisons of stress integration schemes

This chapter presents the results of testing of the stress integration algorithms described in the previous chapter. The Runge-Kutta algorithms and extrapolation scheme are compared against rigorous solutions and against each other. The tests on efficiency and accuracy of those algorithms are also presented.

7.1. Tests against rigorous solutions of BBM

This section describes validation tests for the stress integration algorithms for BBM. The algorithms were checked against independently obtained rigorous solutions. In subsections 7.1.1-7.1.2 the general solution for any strain increment is provided, whereas subsections 7.1.3-7.1.6 consider specific paths.

The tests were performed under assumption that all the suction increments are elastic (i.e. that the suction increase SI yield curve of the BBM is never attained by the stress path, which is also the assumption made in the presented stress integration algorithms). The rigorous solutions were programmed in Microsoft Excel, using macros and a built in solver. In the cases where a closed form solution cannot be obtained, a large number of substeps were used in the Excel macro to ensure the required accuracy. In such cases, solutions were deemed accurate when the changes in computed results with doubled number of substeps were negligible (i.e. close to the machine accuracy).

The tests were performed using the BBM parameters given in Table 7.1. Stresses were integrated by the various algorithms developed in this work with the tolerance of 20%, used in conjunction with EPS error control. Such a high value of tolerance (advised tolerances for the integration in FE application are at most 1%) was required to show clearly the integration error during comparison with rigorous solutions. With a tolerance of 1%, the integration errors were usually too small to be seen in the graphs.

For the tests shown in this section only the Modified Euler Runge-Kutta and extrapolation method were used. In particular, the results of the tests for the extrapolation scheme are presented because of the novelty of this methodology for stress integration. Among the several Runge-Kutta methods investigated in this work, only the results for the Modified Euler scheme are presented. All other Runge-Kutta

schemes have proven to be at least as accurate as the Modified Euler scheme and are tested against each other in subsequent sections of this chapter.

Table 7.1. BBM parameters used in tests

Parameter description	Value
G – shear modulus (constant)	20 MPa
κ – elastic stiffness for changes in mean net stress	0.02
$\lambda(0)$ – stiffness parameter for changes in mean net stress during virgin loading with suction s=0	0.2
M – critical state line slope	0.5
p_c – reference stress	10 kPa
N(0) – specific volume at zero suction for mean net stress equal to reference stress p_c	1.9
p_{atm} – atmospheric pressure	100 kPa
κ_s – elastic stiffness for changes in suction	0.008
k – parameter describing the increase in cohesion with suction	0.6
β – parameter defining the rate of increase of soil stiffness with suction	0.01 kPa^{-1}
r – parameter defining the limit soil stiffness when suction tends to infinity	0.75

7.1.1. Elastic solution: general case

If the initial value of suction s=s$_i$, mean stress p=p$_i$ and shear stress q=q$_i$ are given, the initial specific volume can be calculated as (Alonso et al. 1990)

$$v_i = N(0) - \lambda(s_i)\ln\frac{p_{0,i}}{p^c} - \kappa_s \ln\frac{s_i + p_{atm}}{p_{atm}} + \kappa\ln\frac{p_0}{p_i} \tag{7.1}$$

where $p_{0,i}$ is the preconsolidation pressure (depending on hardening parameter p_0^* and suction). All tests assume that the initial state is elastic (i.e. $p_i < p_0$) and that the increase of suction is proportional to the increment of strain (not increment of stress). The incremental change of specific volume is given as

$$\frac{\delta v}{v} = -\delta\varepsilon_v \tag{7.2}$$

The total elastic change of specific volume is connected to the elastic strain increment

$$\Delta v^e = v_i(e^{-\Delta \varepsilon_v^{el}} - 1) = v_i(e^{-\alpha \cdot \Delta \varepsilon_v} - 1) \tag{7.3}$$

where α is a scalar quantity. In the general case the sample is loaded with an enhanced strain increment $\Delta \varepsilon^{enh} = (\Delta \varepsilon_v, \Delta \varepsilon_q, \Delta s)$ consisting of increments of volumetric strain, shear strain and suction. Firstly, the intersection of the strain path with the yield locus must be found. That is, the factor α that satisfies the following set of equations must be found

$$
\begin{cases}
\Delta \varepsilon^e = \alpha \cdot \Delta \varepsilon = (\alpha \cdot \Delta \varepsilon_v, \alpha \cdot \Delta \varepsilon_q, \alpha \cdot \Delta s) \\
\Delta \sigma^e = \Delta \sigma(\Delta \varepsilon^e) = (\Delta p^e, \Delta q^e, \Delta s^e) = (\Delta p^e, G \cdot \alpha \cdot \Delta \varepsilon_q, \alpha \Delta s) \\
F(\sigma_i + \Delta \sigma^e , s_i + \Delta s^e) = \\
= (q_i + \Delta q^e)^2 - M^2 (p_i + \Delta p^e + k \cdot (s_i + \Delta s^e))(p_{0,i} + \Delta p_0 - (p_i + \Delta p^e)) = 0
\end{cases}
$$

where the increments of stresses $\Delta \sigma^e$ corresponding to the increment of the elastic strain $\Delta \varepsilon^{e,enh}$ bring the initial stress state to the yield locus. The yield stress state should therefore satisfy the initial yield locus equation

$$(q_i + \Delta q^e)^2 - M^2(p_i + \Delta p^e + k \cdot (s_i + \Delta s^e))(p_{0,i} + \Delta p_0 - (p_i + \Delta p^e)) = 0 \tag{7.4}$$

The specific volume on the yield locus is

$$v_{yield} = N(0) - \lambda(s_i + \alpha \cdot \Delta s)\ln\frac{p_{0,i}}{p^c} - \kappa\ln\frac{p_i + \Delta p^e}{p_0} - \kappa_s \ln\frac{s_i + \alpha \cdot \Delta s + p_{atm}}{p_{atm}} = v_i + \Delta v^e \tag{7.5}$$

After introduction of equation (7.1) into (7.3) and (7.3) into (7.5) only α and Δp^e are unknown. The yield locus equation (7.4) is a quadratic equation in terms of mean stress p. Thus Δp^e can be calculated from equation (7.3) and introduced into equation (7.5) so that α can also be found.

After calculating the enhanced elastic strain increment, the elasto-plastic part of the strain increment is given from the difference between the prescribed strain increment $\Delta \varepsilon^{enh}$ and the computed enhanced elastic strain increment. The stress state at the end of the elastic increment $\Delta \varepsilon^{e,enh}$ is on the yield locus. The stress increment $\Delta \sigma^{ep}$ corresponding to the elasto-plastic strain increment $\Delta \varepsilon^{ep,enh} = (\Delta \varepsilon_v^{ep}, \Delta \varepsilon_q^{ep}, \Delta s^{ep}) = (1 - \alpha) \cdot \Delta \varepsilon^{enh}$ needs to be calculated next.

7.1.2. Elasto-plastic solution: general case

In the general case, only an incremental quasi-rigorous solution for the elasto-plastic loading in BBM may be computed, although rigorous solutions for specific tests can be obtained in closed form. The general solution can be obtained by solving the set of equations below (quantities without superscript refer to values at the yield surface)

$$\Delta v^{ep} = v(e^{\Delta \varepsilon_v^{ep}} - 1) \tag{7.6}$$

$$v = N(0) - \lambda(s) \ln \frac{p_0 + \Delta p_0^{ep}}{p^c} - \kappa \ln \frac{p + \Delta p^{ep}}{p_0} - \kappa_s \ln \frac{s + p_{atm} + \Delta s^{ep}}{p_{atm}} = v_{yield} + \Delta v^{ep} \tag{7.7}$$

$$\left(q + 3G\Delta \varepsilon_q^e\right)^2 - M^2\left(p + \Delta p^{ep} + k \cdot s + k\Delta s^{ep}\right)\left(p_0 + \Delta p_0^{ep} - p - \Delta p^{ep}\right) = 0 \tag{7.8}$$

$$p_0 + \Delta p_0^{ep} = p^c \left(\frac{p_0^* + \Delta p_0^*}{p^c}\right)^{\frac{\lambda(0) - \kappa}{\lambda(0)[(1-r)e^{-\beta s - \beta \Delta s^{ep}} + r] - \kappa}} \tag{7.9}$$

$$\Delta \varepsilon_q^e + \Delta \varepsilon_q^p = \Delta \varepsilon_q^{ep} \tag{7.10}$$

$$\Delta \varepsilon_v^e + \Delta \varepsilon_v^p = \Delta \varepsilon_v^{ep} \tag{7.11}$$

$$\ln \frac{p_0^* + \Delta p_0^*}{p_0^*} = \frac{v_{yield} + \Delta v^{ep}}{\lambda(0) - \kappa} \Delta \varepsilon_v^{ep} \tag{7.12}$$

$$d\varepsilon_v^p = \Lambda \cdot \frac{\partial F}{\partial p} = \Lambda \cdot \left(M^2(2p + ks - p_0)\right) \tag{7.13}$$

$$d\varepsilon_s^p = \Lambda \cdot \frac{\partial F}{\partial q} = \Lambda \cdot 2q \quad \text{or} \quad \Lambda \cdot 2q \frac{M(M-9)(M-3)}{9(6-M)} \frac{1}{1 - \frac{\kappa}{\lambda(0)}} \tag{7.14}$$

(the second option in equation 7.14 applies to the a non-associated flow rule as used in the original formulation of BBM). The unknowns are: change of mean net stress Δp^{ep}, change of specific volume Δv^{ep}, change of hardening parameter Δp_0^*, change of preconsolidation stress Δp_0^{ep}, change of elastic shear strain $\Delta \varepsilon_q^e$, change of plastic shear strain $\Delta \varepsilon_q^p$, change of elastic volumetric strain $\Delta \varepsilon_v^e$, change of plastic volumetric strain $\Delta \varepsilon_v^p$ and scalar plastic multiplier Λ. When a rigorous solution of equations (7.13) and

(7.14) is not possible, a quasi-rigorous solution was obtained by dividing the strain increment in very small substeps as described previously.

7.1.3. Isotropic loading under variable suction

In this test soil in isotropic stress state is loaded with a volumetric strain increment $\Delta\varepsilon_v$ and suction increment Δs. At yield $p = p_0$ and the elastic solution is computed directly by combining equation (7.3) and (7.5) as

$$v_{yield} = N(0) - \lambda(s_i + \alpha \cdot \Delta s) \ln\frac{p_{0,i} + \Delta p_0^{el}}{p^c} - \kappa_s \ln\frac{s_i + \alpha \cdot \Delta s + p_{atm}}{p_{atm}} = v_i e^{-\alpha \cdot \Delta\varepsilon_v} \quad (7.15)$$

The equation (7.15) can be solved for α as Δp_0^{el} is in this case a function of α only. At the end of loading the final specific volume is given by

$$v_{end} = N(0) - \lambda(s_i + \Delta s) \ln\frac{p_{0,fin}}{p^c} - \kappa_s \ln\frac{s_i + \Delta s + p_{atm}}{p_{atm}} = v_i + \Delta v.$$ As the specific volume

increment is $\Delta v = v_i(e^{-\Delta\varepsilon_v} - 1)$ the final mean stress $p_{0,fin}$ is

$$p_{0,fin} = p^c e^{\dfrac{N(0) - \left(v_i + \Delta v + \kappa_s \ln\frac{s + \Delta s + p_{atm}}{p_{atm}} \right)}{\lambda(s_i + \Delta s)}} \quad (7.16)$$

Comparison of the rigorous solution with the integration from the Modified Euler scheme (which is a second order Runge-Kutta scheme with first order error estimate) and the extrapolation method are given in Fig. 7.1. An initial mean net stress equal to 15 kPa and an initial suction of 100 kPa were assumed. The initial value of the hardening parameter p_0^* was set to 50kPa.

It can be seen that the solution from both integration schemes is generally accurate and it is only at extremely high values of volumetric strain (reaching 15%) that some larger error, in the case of the extrapolation method, can be observed. Still, these errors are just around 20%, which was the tolerance set for the integration with the EPS error control. Again, such a high strain increment has been deliberately chosen to enable a clear assessment when the integration error is becoming significant. Note that the small strain assumption at this value of volumetric strain is quite crude (as the Lagrangean and Eulerian strain measures will differ) and a proper analysis should be performed under large strain theory.

132
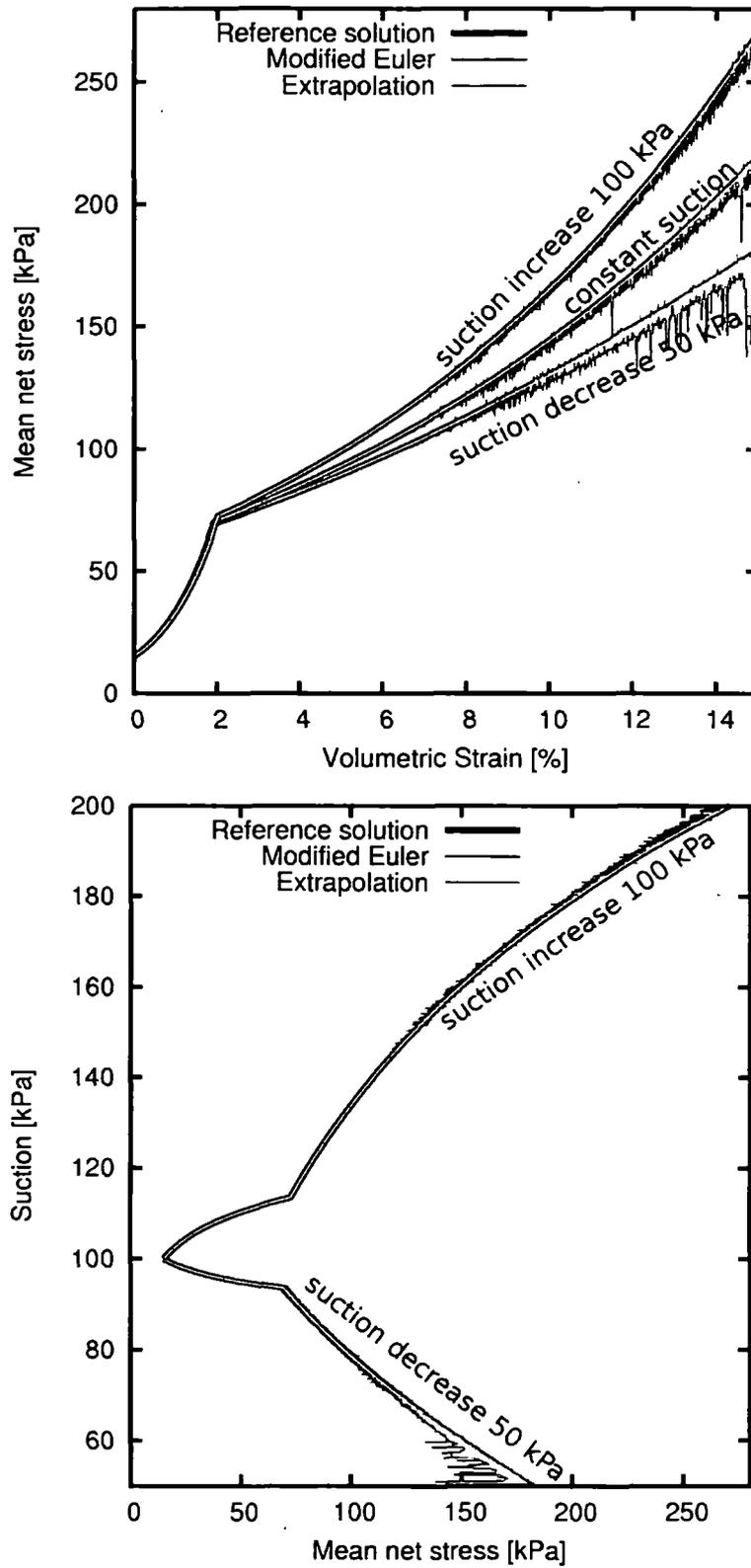
Figure 7.1. Isotropic loading at variable suction starting from an initial isotropic stress state: mean net stress versus volumetric strain (top) and suction versus mean net stress (bottom)

133

7.1.4. Isotropic loading under variable suction with initial non-isotropic stress state

The initial stress is given here in terms of mean net stress $p_i=15$ kPa, shear stress $q_i=30$kPa and suction $s_i=100$ kPa. The soil is loaded with series of progresively larger volumetric strain $\Delta\varepsilon_v$ and a suction increment Δs, always starting from the same initial state. The elastic solution in this case was obtained from (7.1 - 7.5), noting that $\Delta\varepsilon_s = 0$. Using the set of general equations (7.6-7.14) the quasi-rigorous solution is obtained in Excel for the elasto-plastic loading as previously explained..

Results are given in Figs 7.2 and 7.3, which indicate that very different accuracies are obtained by the extrapolation method depending on whether an associated or non-associated flow rule is employed. This is the only case when such a large error and oscillations were observed during stress integration with the extrapolation method. It is unclear why such a big discrepancy occurred; it has been however observed that the extrapolation algorithm fares relatively poorly on purely volumetric paths while the accuracy is usually excellent when variations of shear stresses are involved. It must be mentioned that the algorithms for associated and non-associated flow rules are the same – the only difference is in the change of the parameter value defining the type of flow rule in the BBM. Finally, it must be remembered that the amount of error given in Fig. 7.2 (obtained with the EPS error control) would be much reduced when using a smaller integration tolerance (e.g. 1% or less as usually done in FE applications) than the value of 20% employed in such tests. Additionally, it should be noted that the errors in shear stress are large relative to the current value (which is very small). However, even for the largest error in shear stress, the absolute magnitude of such error is similar to the absolute magnitude of the error in the mean net stress.
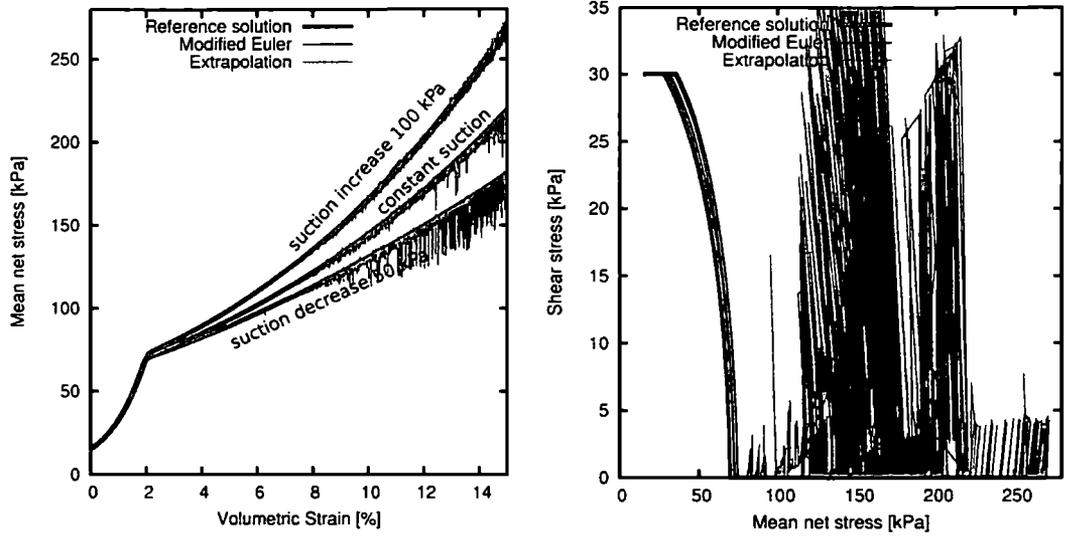
Figure 7.2. Isotropic loading at variable suction starting from an initial non-isotropic stress state with associated flow rule: mean net stress versus volumetric strain (left) and shear stress versus mean net stress (right).
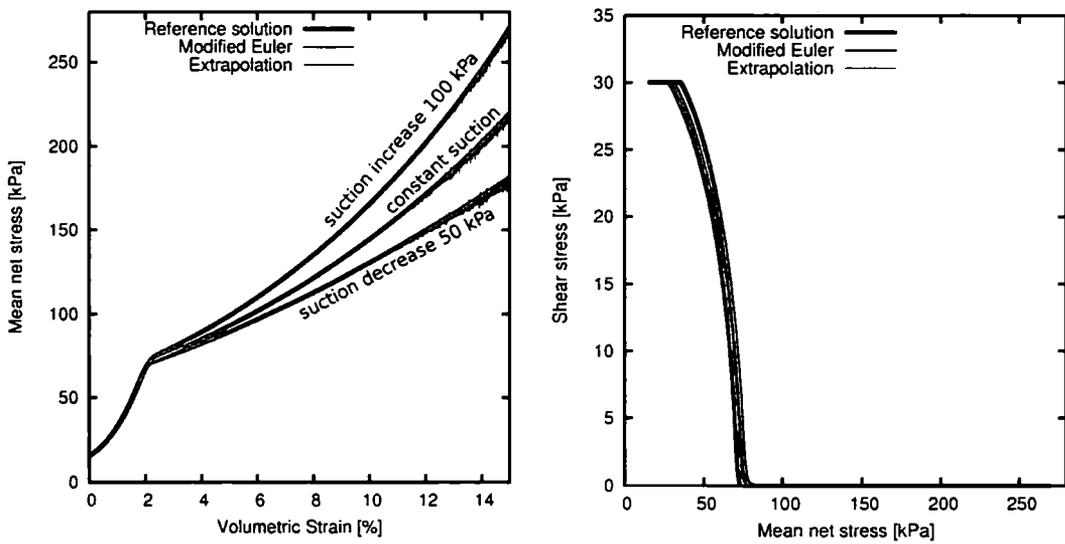
Figure 7.3. Isotropic loading at variable suction starting from an initial non-isotropic stress state with non-associated flow rule: mean net stress versus volumetric strain (left) and shear stress versus mean net stress (right).

7.1.5. Oedometric loading under variable suction with initial non-isotropic stress state

Oedometric loading is defined by an increment of strain components such as $\Delta\varepsilon^{enh} = (\varepsilon_1, 0,0,0,0,0, \Delta s)$. For this case the relationship between the increments of volumetric strain and shear strain is given as

$$\Delta\varepsilon_s = \frac{2}{3}\Delta\varepsilon_1 . \tag{7.17}$$

The soil is loaded with both an increment of volumetric strain and an increment of suction. The rigorous elastic and quasi-rigorous elasto-plastic solution was obtained in sections 7.1.1 and section 7.1.2 respectively.

In the results shown in Figs 7.4 - 7.7 the initial value of suction was equal to 100 kPa and the initial value of the hardening parameter p_0^* was equal to 200kPa. The oedometric tests were calculated for two cases: i) a heavily preconsolidated soil with an initial mean net stress equal to 5 kPa and ii) a slightly preconsolidated soil with an initial mean net stress of 200 kPa. The initial shear stress was zero in all cases. The soil was loaded on the oedometric path (i.e. with non-zero ε_{11} but all other strain components equal to zero) until a volumetric strain of 15% was attained. The EPS error control was used with the tolerance set to 20%.

Inspection of Figs 7.4-7.7 indicates that in all cases the extrapolation method matches almost perfectly the rigorous solution (with the exception of loading combined with wetting with associated flow rule, where some small oscillations can be seen for very large strain increments). In the case of the Modified Euler scheme, a noticeable departure from the rigorous solution can be observed. The visible cyclical increase and decrease in solution accuracy is likely an effect of automatic subincrementation. The large discrepancy between the Modified Euler scheme and the rigorous solution is deliberate and due to the very large value of the integration tolerance assumed in these tests (combined with very large strain increments to integrate). If the tolerance is set to a smaller value, typically 1% or less, the difference between the integrated stresses and the rigorous would be difficult to notice.

136
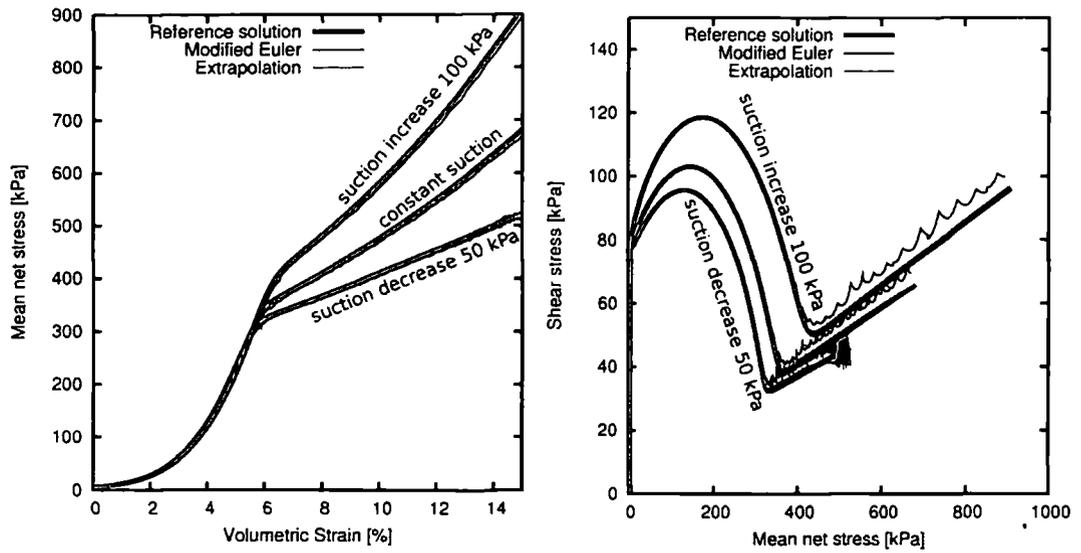
Figure 7.4. Oedometric loading at variable suction for heavily overconsolidated soil with associated flow rule: mean net stress versus volumetric strain (left) and shear stress versus mean net stress (right)
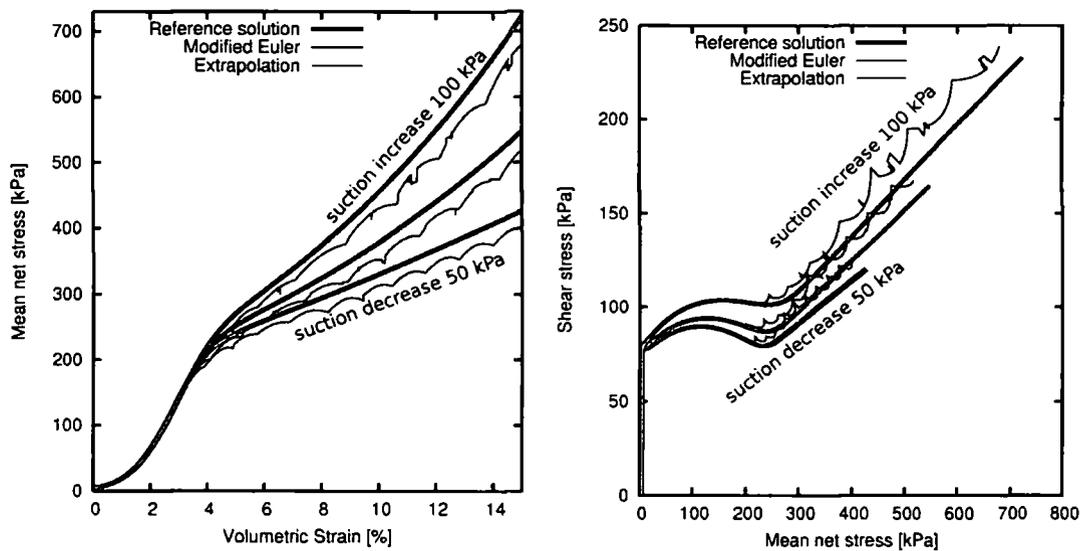
Figure 7.5. Oedometric loading at variable suction for heavily overconsolidated soil with non-associated flow rule: mean net stress versus volumetric strain (left) and shear stress versus mean net stress (right)
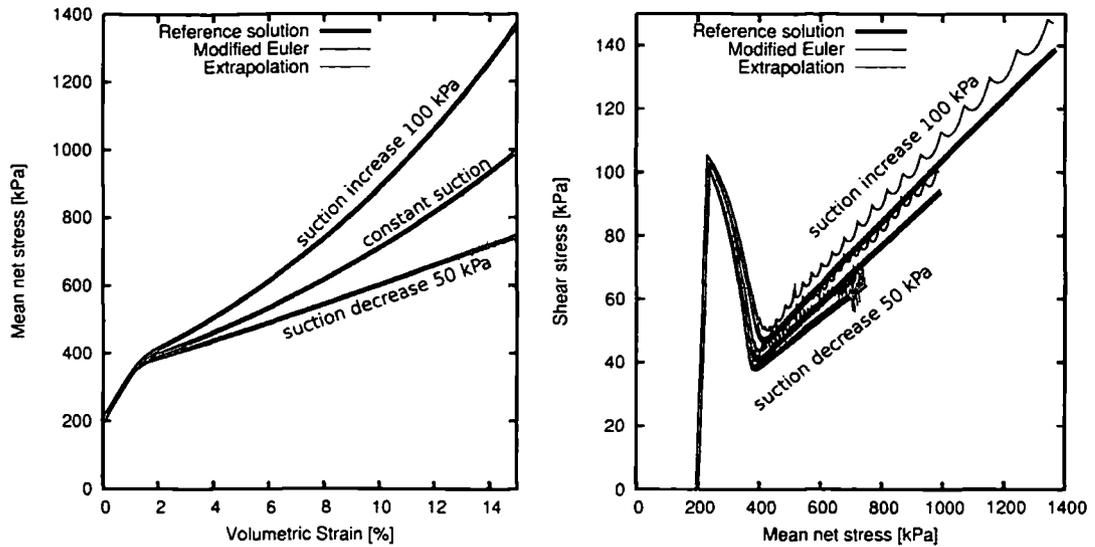
Figure 7.6. Oedometric loading at variable suction for slightly overconsolidated soil with associated flow rule: mean net stress versus volumetric strain (left) and shear stress versus mean net stress (right)
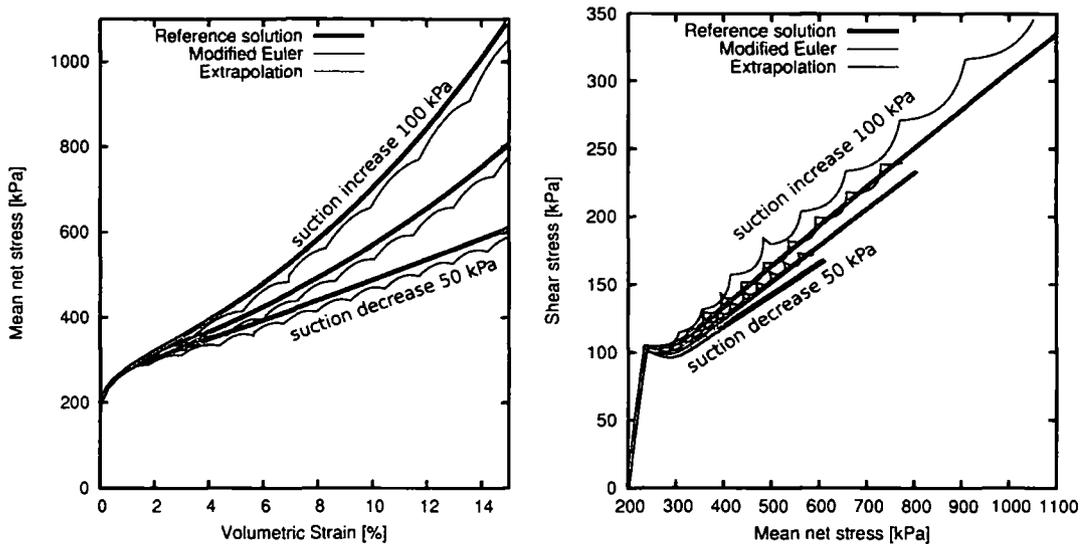
Figure 7.7. Oedometric loading at variable suction for slightly overconsolidated soil with non-associated flow rule: mean net stress versus volumetric strain (left) and shear stress versus mean net stress (right)

7.1.6. Wetting under constant volume

In this test the soil is wetted while its volume is kept constant, so the strain increment is given by $\varepsilon = (\Delta\varepsilon_v, \Delta\varepsilon_s) = (0,0)$ while the non-null suction increment is equal to Δs. This test may be regarded similar to a isotropic compression test combined with wetting, where the amount of compression/swelling due to the change in the isotropic stress state is such that it exactly counters the collapse/swelling due to a change of suction (so the change of specific volume is null). Therefore the rigorous solution for this test

138

corresponds to that for a special case of isotropic compression where suction change is applied but the volumetric strain is equal to zero. Thus, the equations previously given in Section 7.1.4. for the isotropic compression would apply also to this case.

The tests undertaken were performed for both associated and non-associated flow rules but these gave virtually the same results and are not distinguishable in Fig.7.8. The tests were performed for both isotropic (p=70 kPa and q=0) and non-isotropic (p=15 kPa and q=30 kPa) initial stress states and involved full wetting from initial suction of 100 kPa. The initial hardening parameter p_0^* was equal to 50 kPa in both cases. However, as only the test with a non-isotropic initial stress state had any shear stress, it is only this test which is depicted in Fig. 7.8 (right). It can be observed that an excellent agreement exists between the rigorous solution and the results obtained from the integration algorithms despite using a large value of the integration tolerance (20%).
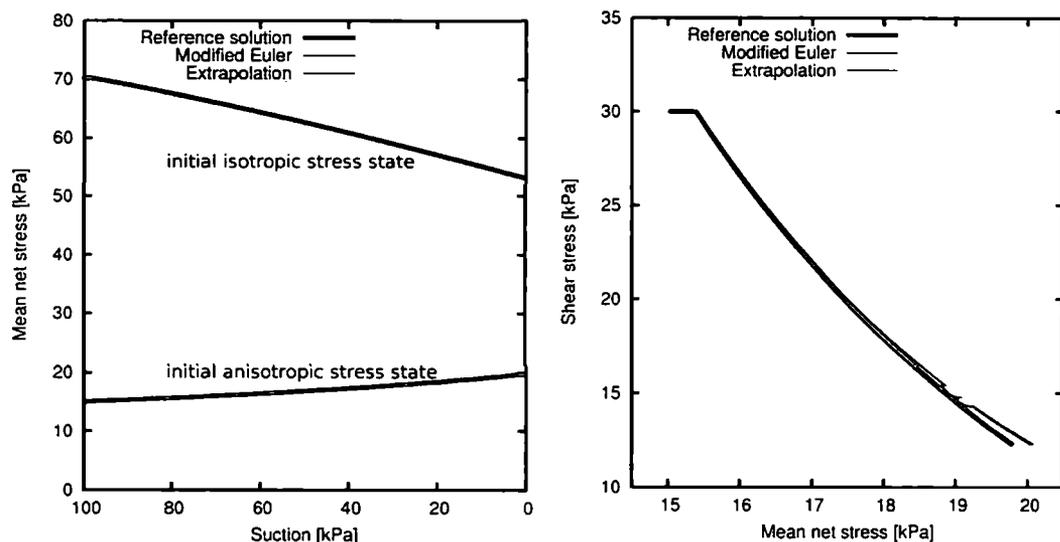
Figure 7.8. Isochoric wetting starting from both initial isotropic and anisotropic stress states: mean net stress versus suction (left) and shear stress versus mean net stress (right).

7.2. Efficiency of stress integration algorithms

In this section, the efficiency and accuracy of all stress integration algorithms developed in this work is further evaluated. Firstly the evaluation is performed based on random strain increments, whereafter results are presented from tests with prescribed strain increments, shown in the form of iso-error maps.

139

7.2.1. Evaluation of stress integration algorithms basing on random strain increments

The efficiency of the algorithms has been assessed in terms of the computational time and number of evaluations of the elasto-plastic matrix required to integrate 6000 strain increments. Each strain increment was randomly generated with increments of strain components ε_{11}, ε_{22}, ε_{33} varying over the range [-5%; 5%], increments of strain components ε_{12}, ε_{13}, ε_{23} varying over the range [-3%; 3%] and suction increments varying over the range [-100kPa; 200kPa].

These randomly generated strain increments were imposed starting from three different initial triaxial stress states, which were located close to the yield locus corresponding to a hardening parameter value $p_0^* = 200$ kPa. In particular, these three initial triaxial stress states are located on the yield ellipse at a constant suction of 100 kPa and correspond to three different angles measured from the mean net stress (p) axis about the centre of the ellipse. The chosen angles were $0°$ (initial isotropic stress state), $60°$ (initial stress state on the right side of the constant suction yield ellipse) and $120°$ (initial stress state on the left side of the constant suction yield ellipse). The BBM parameter values used in all integrations are the same as in the tests described in section 7.1 and are listed in Table 7.1.

Although three initial stress states have been used in these tests, here the comprehensive results for only one initial stress state are shown – i.e. the initial stress state located on the mean net stress axis with the initial mean net stress equal to 350 kPa. Only results corresponding to this initial stress state are presented because no qualitative difference has been observed for the other two states examined.

Reference quasi-rigorous net stress solutions were calculated for each randomly generated strain increment by dividing such increment into one million equal sized subincrements and using an explicit forward Euler scheme for the integration. To minimise the errors due to machine accuracy, a 30-digit storage was used to calculate these solutions. The error for the different integration schemes was quantified against these reference solutions. A single measure of the error E_{av} was obtained by averaging the error across all net stress components and all randomly generated strain increments. In particular, the average error E_{av} is calculated as

$$E_{av} = \frac{1}{6000} \sum_{n=1}^{6000} \frac{1}{6} (E_{11}^{(n)} + E_{22}^{(n)} + E_{33}^{(n)} + E_{12}^{(n)} + E_{13}^{(n)} + E_{23}^{(n)}) \qquad (7.18)$$

140

$E_{ij}^{(n)}$ is the relative error of the ij-th component of the net stress increment corresponding to the n-th randomly generated increment of strain and is defined as

$$E_{ij}^{(n)} = \frac{abs(\Delta\sigma_{ij} - \Delta\sigma_{ij\,ref})}{\Delta\sigma_{ij\,abs}} \qquad i, j = 1,2,3 \qquad (7.19)$$

where the $\Delta\sigma_{ij}$ is the net stress increment computed by the relevant integration scheme, $\Delta\sigma_{ij\,ref}$ is the reference net stress increment calculated according to the quasi-rigorous solution given in section 7.1 and $\Delta\sigma_{ij}$ abs is the sum of the absolute values of the reference net stress changes computed in each of the one million subincrements.

The quantity $\Delta\sigma_{ij\,abs}$ is used instead of $\Delta\sigma_{ij\,ref}$ in order to reduce the likelihood of a null denominator in equation (2). It might happen that, for given strain and suction increments, one or more components of the corresponding reference net stress increment are equal to zero. However, it is unlikely that net stress changes are equal to zero in all subincrements (even if the overall net stress increment given by the sum of such sub-steps is equal to zero). This definition of relative error also gives a better approximation of the real error. Otherwise, in the case where the change of a net stress component is close to zero (over the entire strain and suction increments), the computed error would be unrealistically high.

The efficiency of the Runge-Kutta schemes and the extrapolation method are compared in terms of the computational time and number of computations of the elasto-plastic tangent stiffness matrix required to integrate all 6000 strain increments. The tolerance was never set to more than 30 % as this value seems to be more than a value required even for the roughest of engineering simulations. On the other hand, due to limited accuracy of the rigorous solution, the tightest tolerance was set so that the error did not lie much below 0.001 %. This accuracy, again, is likely to be beyond the accuracy needed in most engineering applications.

It has been found that the accuracy of 30% led to, on average, much more accurate solutions when the EPUS error control method was used (compare Fig. 7.15) and thus the lowest accuracy obtained with the EPUS method is below 1%.

A comparison of the computational times for the best performing Runge-Kutta schemes and the extrapolation method is given in Fig. 7.9 where the effect of using different error control methods (i.e. Error per Step (EPS, as given by Sloan 1987) versus Error per Unit Step (EPUS)) can also be appreciated (see sections 6.1.4 and 6.2.3 for

description of EPS and EPUS error control). Each of the different curves in Fig. 7.9 has been obtained by running the relevant algorithm with a different integration scheme.

Inspection of Fig. 7.9 indicates that the time of computation with the EPS or EPUS error control is similar only for the highest fifth order Runge-Kutta schemes (i.e. Cash-Karp and England schemes). For all other schemes, the use of EPS reduced the time required for computations over the whole range of average errors. However, even in the case when the highest order Runge-Kutta schemes are used, integration algorithms coupled with EPUS error control are less robust.

In general, the extrapolation method appears less efficient than Runge-Kutta schemes and, similarly to lower order Runge-Kutta schemes, efficiency improves when EPS instead of EPUS control is used. The extrapolation method is also the most robust among all tested schemes, and always converges to a solution even when coupled with EPUS control. This relatively higher stability stems from the fact that the extrapolation method is based on the estimation of a global error over the whole strain increment rather than on a local error estimation, as it is the case for all Runge-Kutta schemes with automatic subincrementation. The extrapolation routine in the extrapolation method only increases the convergence rate and thus the algorithm will finally always converge, being at worst similar in efficiency to the constant step forward midpoint method.
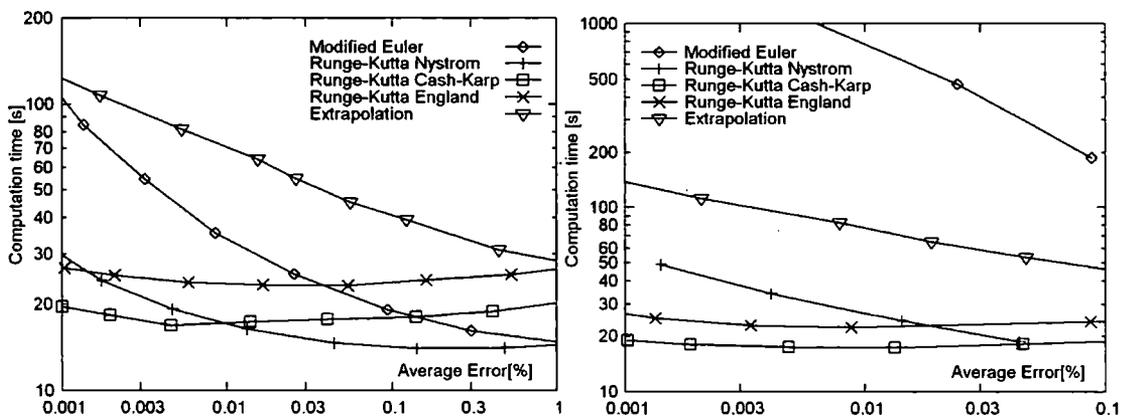
Figure 7.9. Computation times versus average error for best Runge-Kutta schemes and extrapolation method with EPS control (left) and EPUS error control (right).

Figs 7.10 and 7.11 present a more detailed comparison of the efficiency (in terms of computation times and number of evaluations of the tangent elasto-plastic matrix) of Runge-Kutta schemes of different orders when using both EPS and EPUS control. Figures 7.10 and 7.11 compare the efficiency of the second order Modified Euler

scheme, the best performing third order scheme (i.e. Nystrom), the fourth order scheme and the best performing fifth order scheme (i.e. Cash-Carp).

The variations of computation time and number of evaluations of the elasto-plastic matrix follow approximately the same trend with average error. This is expected because the majority of computation time is spent by the algorithms in evaluating the elasto-plastic matrix in each substep. The slight discrepancies between the two trends may be explained by the additional computation time associated with plastic drift occurring at the end of some sub-steps, which requires mapping the stress state back to the yield locus as described in section 6.3.2.

For the two lower order schemes, there is a clear tendency of the computational time to increase when the average error decreases, as expected. However, the two higher order schemes show only a slight variation when average errors change by several orders of magnitude. Moreover, a counterintuitive decrease of computational time with decreasing average error is initially observed. This behaviour (especially evident in Fig. 7.10 where EPS error control is used) might also be explained by the drift correction at the end of some substeps. Any drift correction is added to the estimated error leading to larger numbers of rejected sub-steps and hence longer computational times when lenient tolerances are used (i.e. at high values of the average error). On the other hand, the drift correction becomes largely irrelevant when the integration tolerance is stricter.

Inspection of Fig. 7.10 indicates that, in the case of EPS error control, the Modified Euler is the most efficient scheme for very crude accuracies while higher order schemes become more competitive as the average error decreases. Overall, the third order Nystrom scheme appears the best for the range of average errors considered. This scheme remains competitive even for relatively stringent accuracies and is outperformed by the fourth order scheme and fifth order Cash-Karp scheme only when the average error decreases to about 0.01%.

When EPUS error control is used, the fourth order scheme and the fifth order Cash–Karp scheme are the most efficient choices throughout the whole range of accuracies, as shown in Fig. 7.11. The Cash–Karp scheme is also the most efficient scheme when high accuracy is required, regardless whether it is used in conjunction with EPS or EPUS control.

Computation times are generally lower when EPS control is used. However such gain of efficiency is mainly limited to the lower order schemes. In particular, it is worth noting that the second order Modified Euler scheme becomes very inefficient when used in

143

conjunction with EPUS control as shown in Fig. 7.11, which confirms that the EPUS error control effectively reduces the method order by one (e.g. Shampine 1994). For the fourth order scheme and the fifth order Cash–Karp scheme the efficiency remain largely unchanged regardless whether the EPS or EPUS control is used.

Fig. 7.12 compare efficiency of the two third order schemes (i.e. the Nystrom and Bogacki-Shampine schemes) while Fig. 7.13 presents the same comparisons for the four fifth order schemes (i.e. the Bogacki-Shampine, England, Cash-Karp and Dormand-Prince schemes). The results presented in both these figures refer to the case where EPS control is used. A similar comparison for the four fifth order schemes used in conjunction with EPUS control is shown in Fig. 7.14.

Figures 7.12, 7.13 and 7.14 indicate that the recently proposed Bogacki–Shampine third order and fifth order schemes are noticeably less efficient than the third order Nystrom and fifth order Cash-Karp schemes respectively. This is partly because both these Bogacki–Shampine schemes do not take advantage of the FSAL (First Same As Last) technique, which is one of their distinctive features. The FSAL technique allows saving one evaluation of the elasto-plastic stiffness matrix by using the last evaluation within a successful sub-step as the first evaluation of the following sub-step. The FSAL technique cannot be implemented here because the stress state might change due to drift correction, so the last evaluation of the elasto-plastic matrix might no longer be relevant to the stress state at the start of the subsequent sub-step. A partial version of the FSAL technique has, however, been tested whereby the last evaluation of the elasto-plastic stiffness matrix is used again in the subsequent sub-step in case no drift correction was performed. This only led to a slightly better performance of the Bogacki–Shampine schemes, which still remained less efficient than othe Runge-Kutta options.
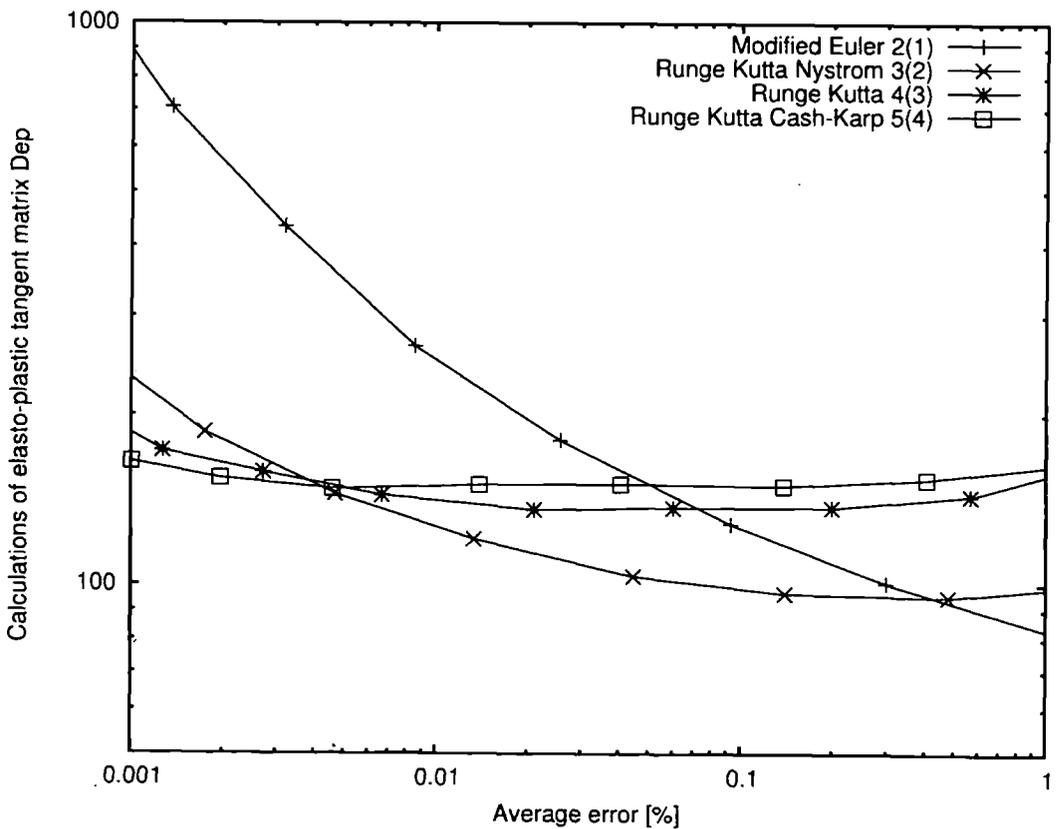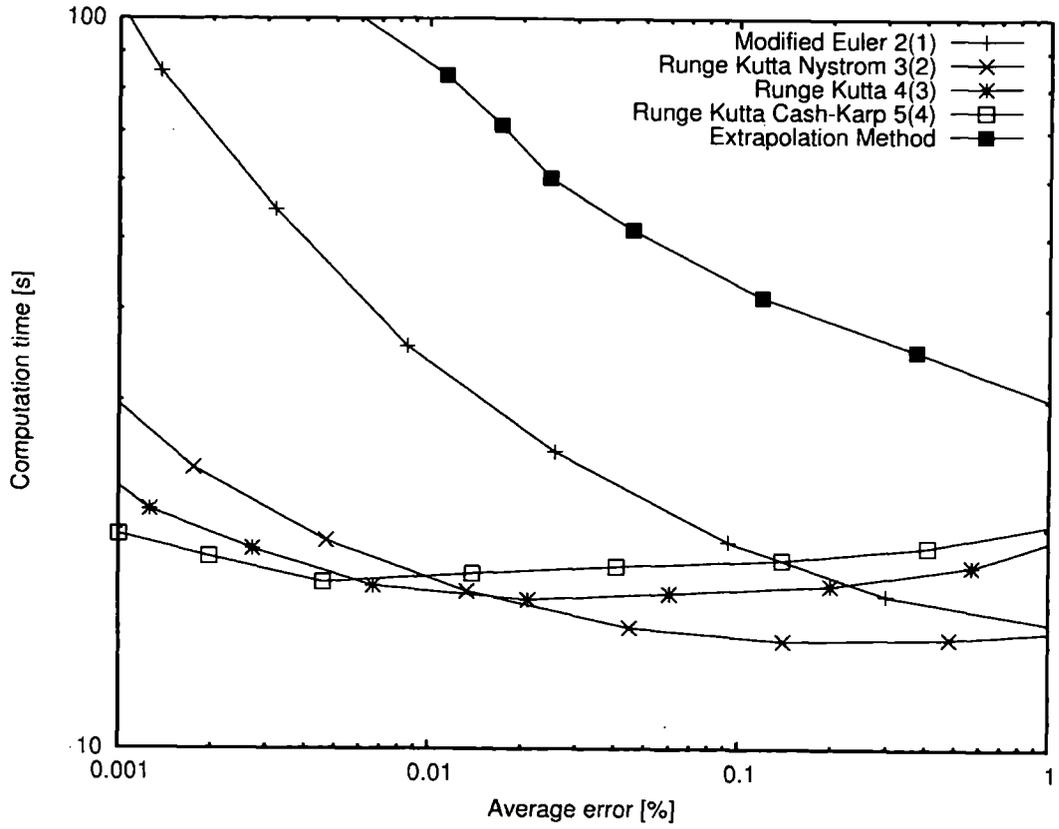
Figure 7.10. Comparison of efficiency for best Runge-Kutta schemes of order two, three, four and five and extrapolation method when coupled with EPS error control.
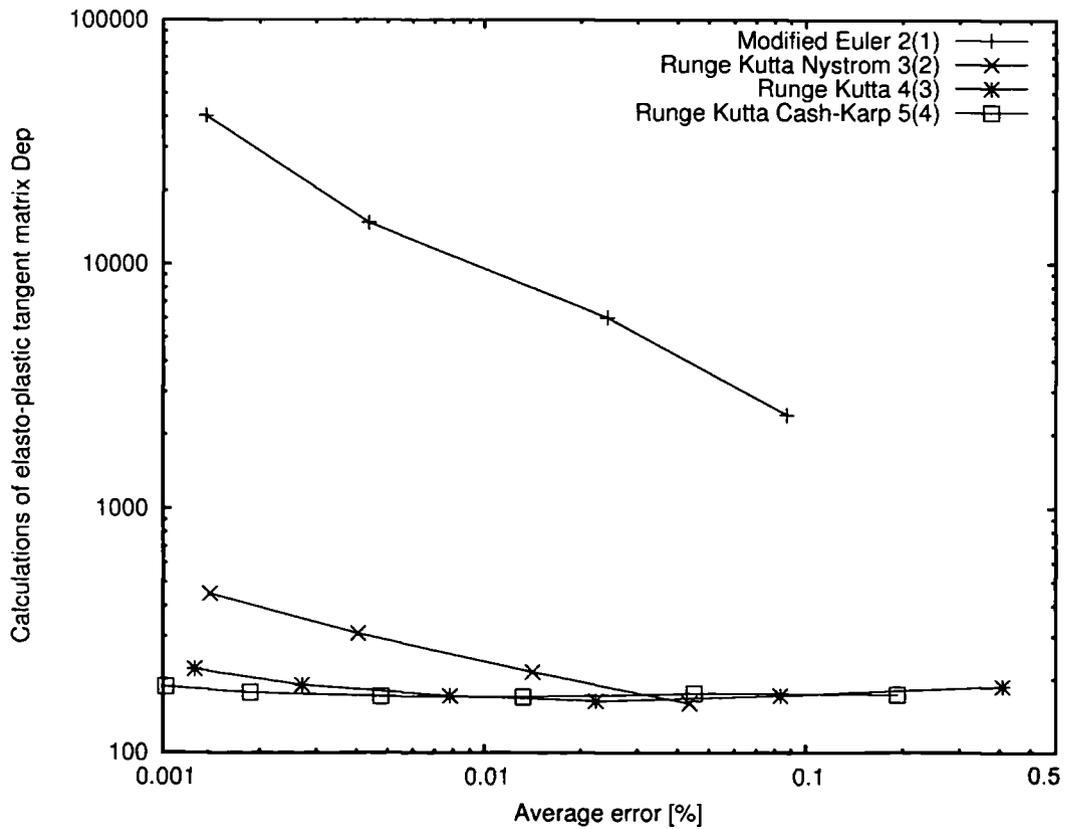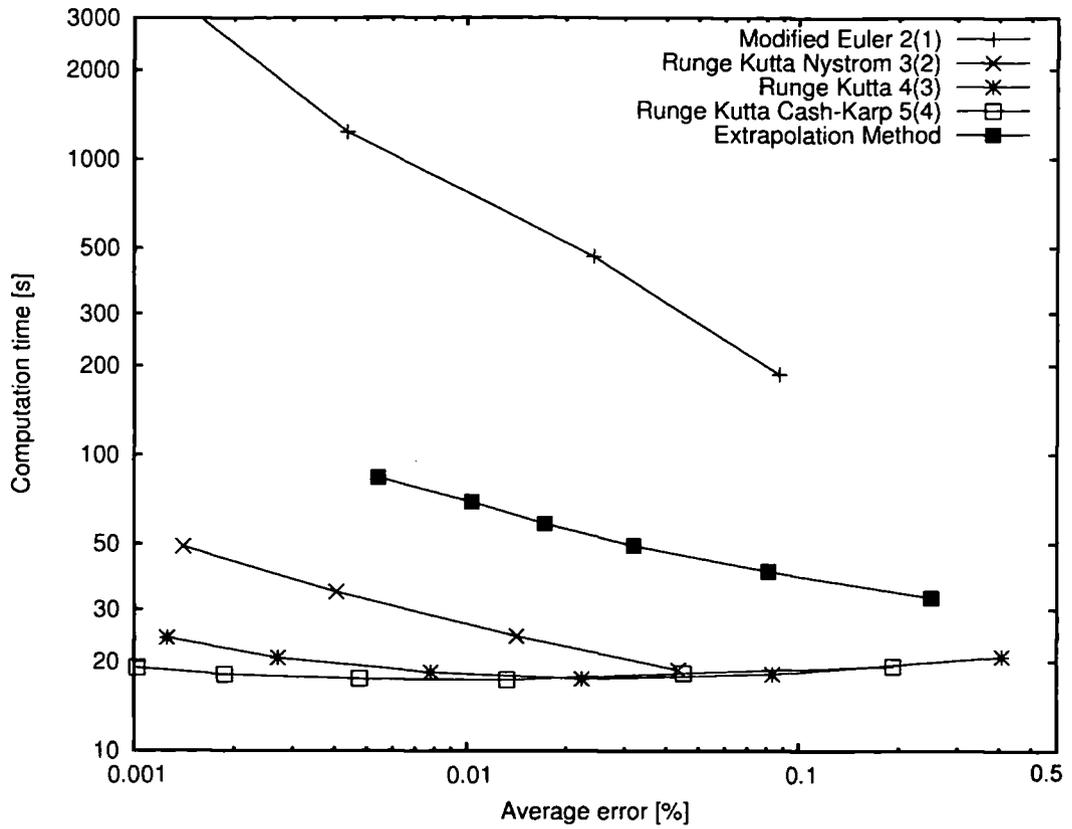
Figure 7.11. Comparison of efficiency for best Runge-Kutta schemes of order two, three, four and five and extrapolation method when coupled with EPUS error control.
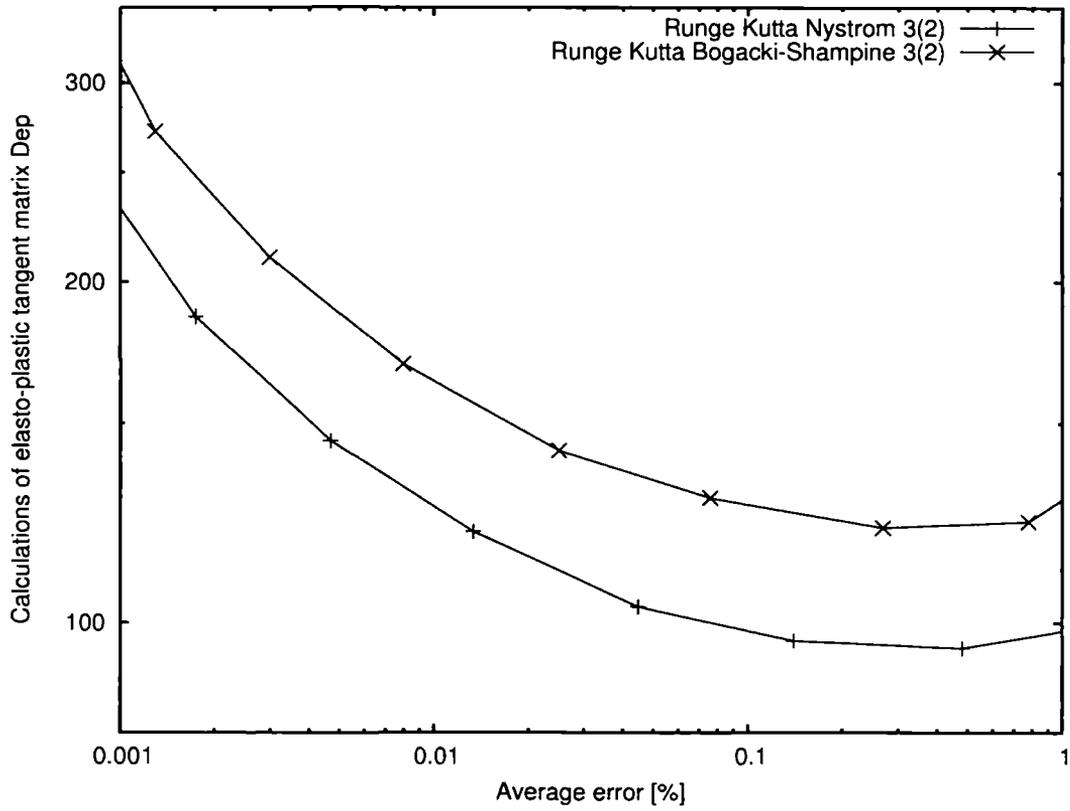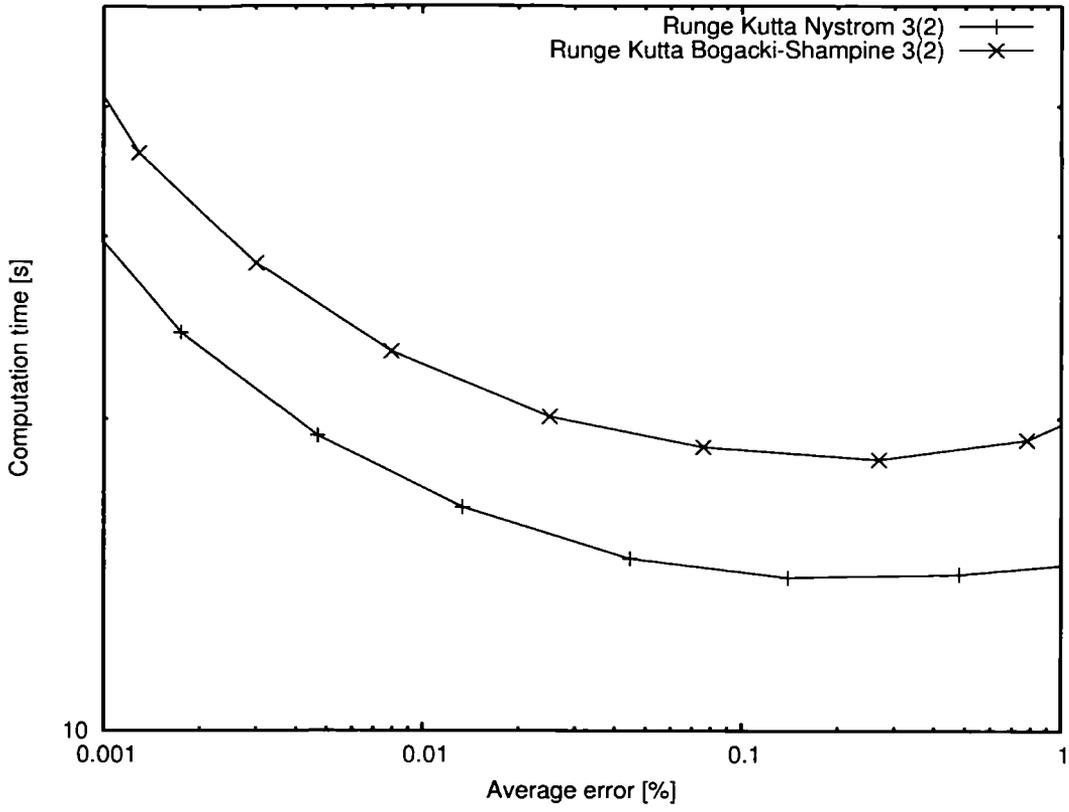
Figure 7.12. Comparison of efficiency for third order Runge-Kutta schemes with EPS control.
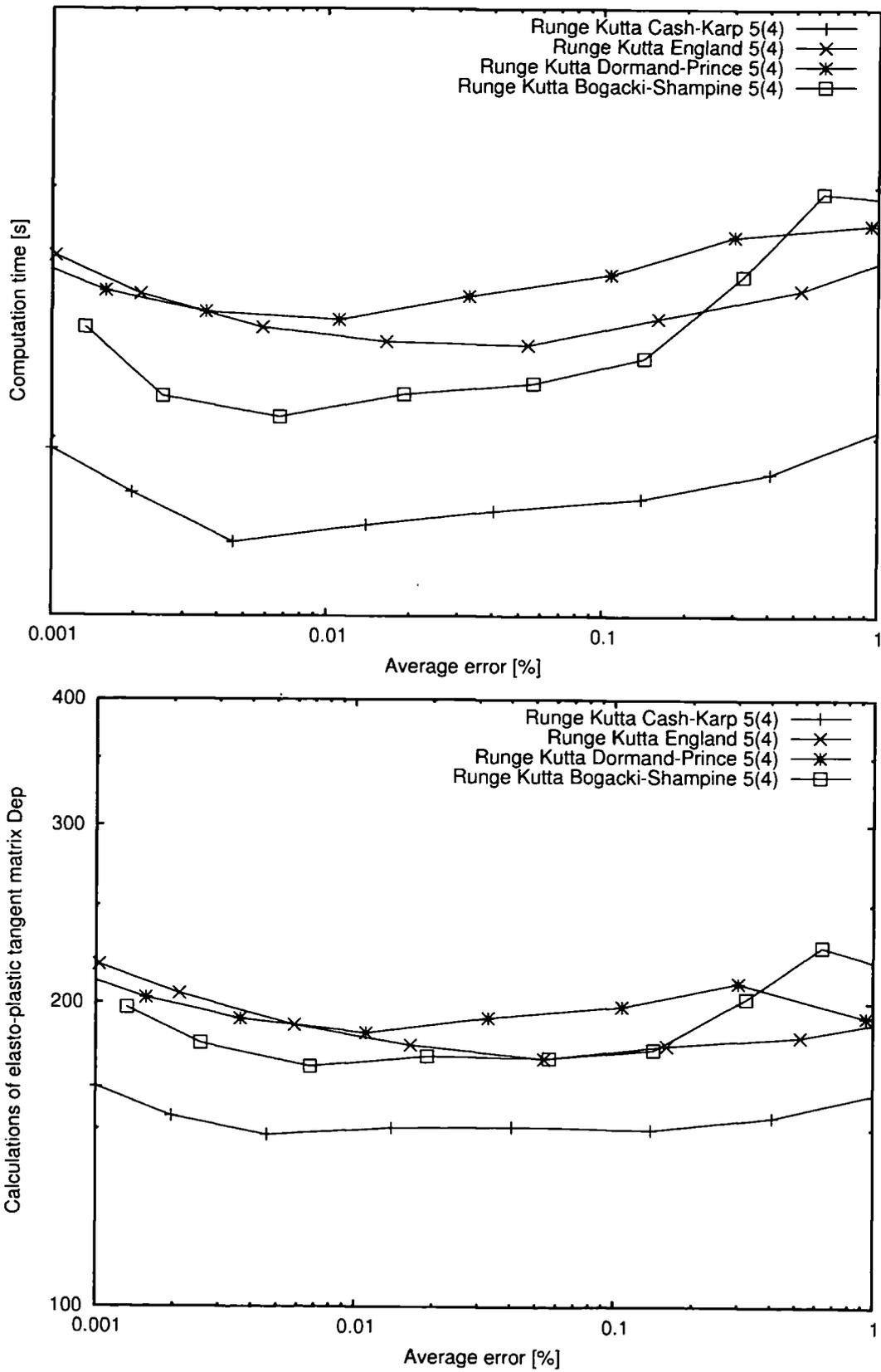
Figure 7.13. Comparison of efficiency for fifth order Runge-Kutta schemes with EPS error control.
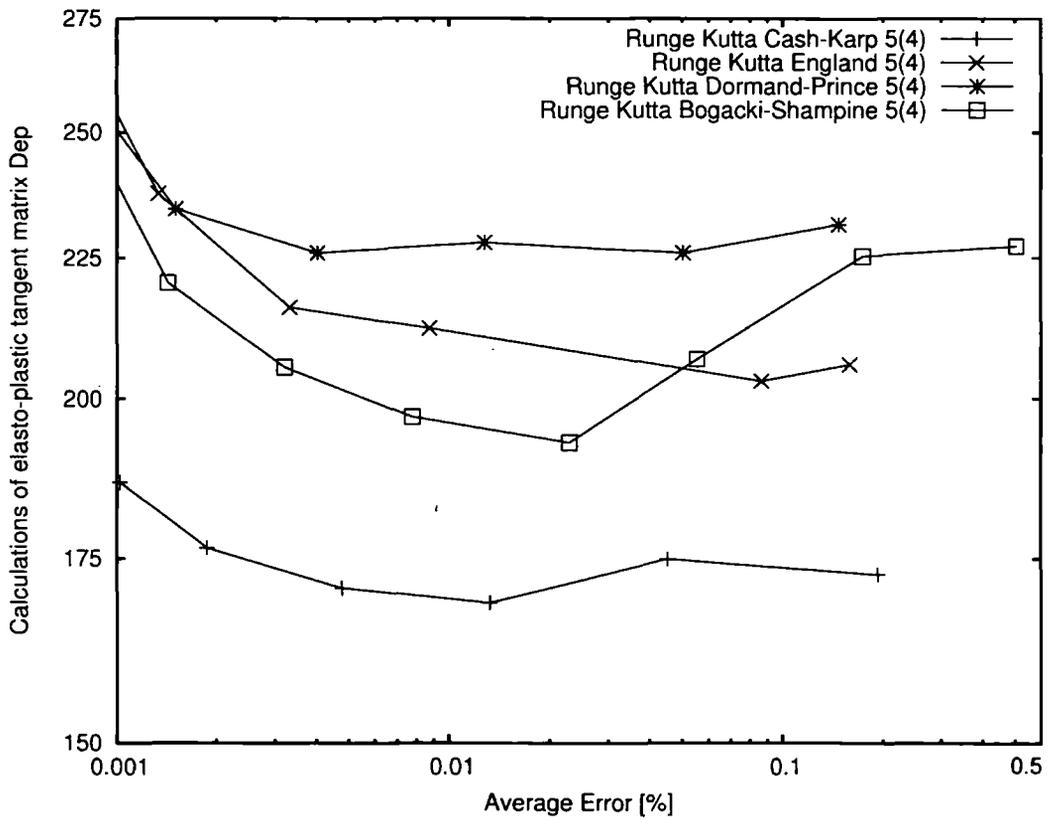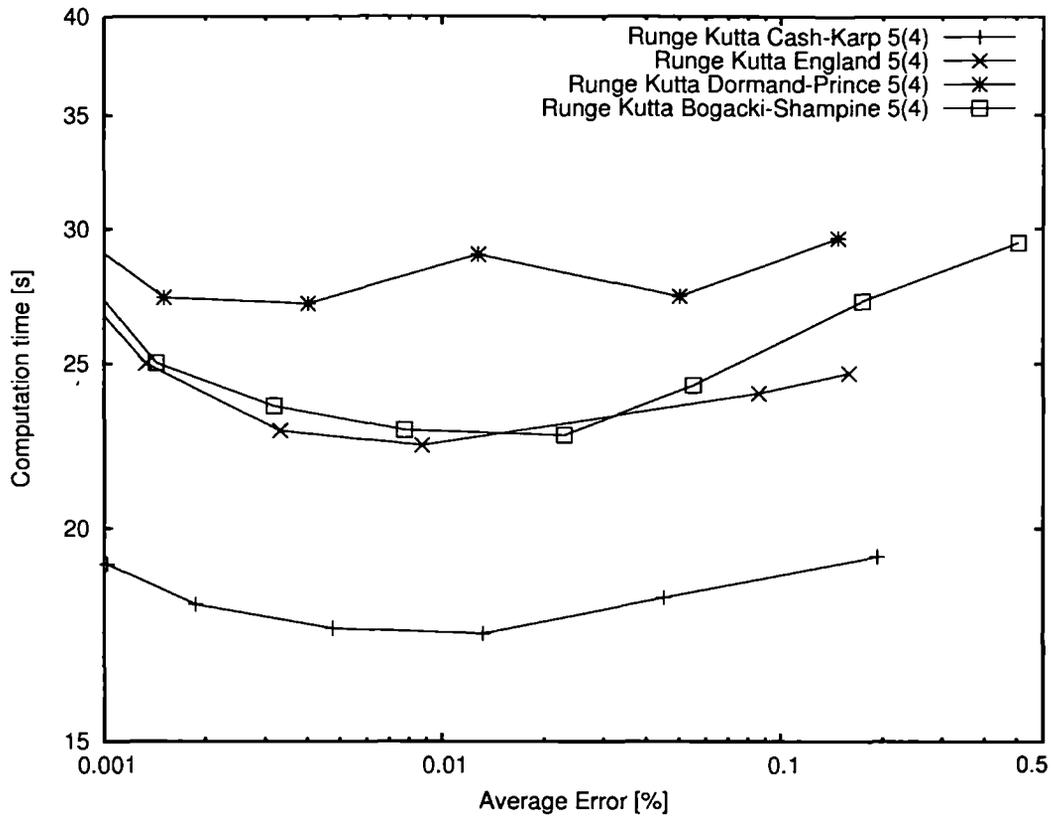
Figure 7.14. Comparison of efficiency for fifth order Runge-Kutta schemes with EPUS error control .

Fig. 7.15 compares the relationship between average error and integration tolerance for the Runge-Kutta schemes when used in conjunction with both EPS and EPUS control. It can be noticed that the average error is generally smaller than the set tolerance. Such difference is particularly noticeable when EPUS control is used resulting in significantly more accurate integration than required. The difference between the two error controls is not surprising given that EPUS imposes a stricter constraint on integration than EPS as it calculates the estimated error in each sub-step relative to the corresponding stress increment (rather than relative to the current stress value as in EPS). This also implies that, in the case of EPUS control, the average error is significantly smaller than the integration tolerance in the vast majority of subincrements.

Inspection of Fig. 7.15 indicates that, for all schemes, a linear relationship can reasonably be assumed between the logarithm of the average error and the logarithm of the integration tolerance. The Modified Euler and Nystrom schemes are not shown for higher accuracies as the time of calculations was prohibitive. Note also that the Runge-Kutta England scheme is the most accurate for a given accuracy. However, this scheme also takes longer to compute the stress increments and overall efficiency of this scheme is worse than that of Runge-Kutta Cash Karp method (Fig. 7.14). An opposite situation is true for the fifth order Bogacki-Shampine scheme. This scheme is the one giving highest error for prescribed accuracy, but it is no more efficient than the other schemes with calculations at the given error level.
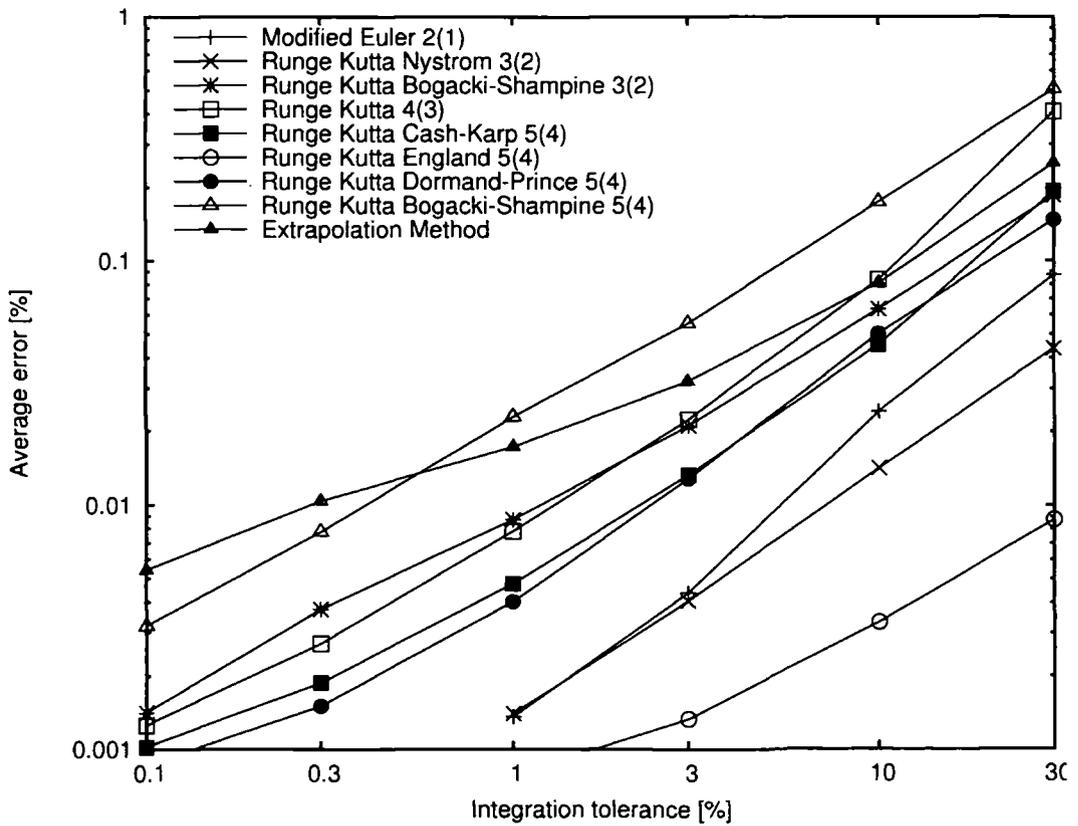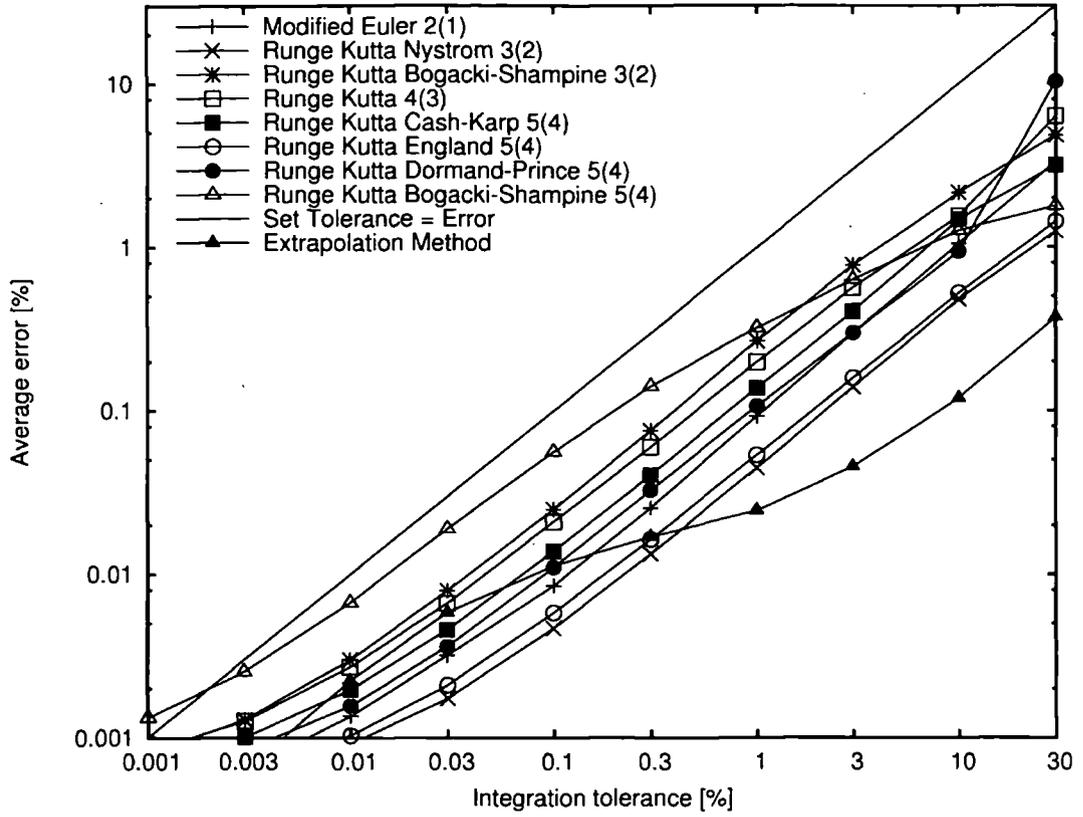
Figure 7.15. Average error vs tolerance for Runge-Kutta methods and extrapolation method with EPS error control method (top) or EPUS error control method (bottom).

151

The results shown here refer to large strain increments, so it is expected that the sub-step size is close to optimal. However, previous Finite Element analyses of boundary value problems (see e.g. Sloan 1987, Sheng et al. 2003b, Potts and Zdravkovic 1999) show that, even when suboptimal sub-step sizes are possibly used in conjunction with EPS control, the error remains smaller than the set tolerance and varies proportionally with the tolerance value, as expected for strictly dissipative systems (Deuflhard and Bornemann 2002).

It is worth re-stating here that the average errors shown in Figure 7.15 are mean values as defined by equation (7.18) across all net stress components and across 6000 increments of enhanced strain. The integration error for an individual enhanced strain increment might be quite different from such average values as shown in the next section.

7.2.2. Evaluation of stress integration algorithms: error maps

According to the results shown in section 7.2.1, there appears to be little motivation for the use of the EPUS control. However, when the error properties are investigated in greater depth, some advantages of the EPUS approach become apparent. Comparison of error maps for both EPS and EPUS control (see Figs. 7.16 and 7.17) shows that, when using EPUS control for the integration of generic strain increments, the error remains almost invariably below the set integration tolerance (see Table 7.2). On the other hand, when EPS control is used, the error is more likely to exceed the set integration tolerance for specific strain increments. This difference between the two types of error control is not surprising given that EPUS imposes a stricter constraint on integration than EPS, as discussed in the previous section.

This advantage in terms of accuracy, resulting from the use of EPUS control, comes however at the price of longer computation times. It is therefore necessary to make a judgement whether an improvement in the error properties of the integration schemes justify the use of longer computation times associated to the use of EPUS control (bearing in mind that EPUS control might also be less stable particularly in the case of low order schemes).

The error maps shown in Figs 7.16 and 7.17 were created starting from the same initial stress state and using the same set of parameter values for the BBM (see Table 7.1.) as described in the previous section. The error maps were drawn by integrating strain increments over a dense mesh of 101 x 101 points in the volumetric strain shear strain

plane, giving a total of 10201 strain increments to integrate. Such a dense mesh allows capture of the full behaviour of the algorithm and the fine details of the error variations (as shown by the rather uneven contour of iso-error lines). In this case, the rigorous reference solution for the calculation of the error was obtained by using the Cash - Karp integration scheme with a large number of constant step size subincrements. The error maps present the maximum error in any of the stress components.

The results are summarised in Table 7.2, where the percentage of points with accuracy exceeding the integration tolerance is given for all integration schemes used in this work. Nystrom and Modified Euler schemes fail to converge when used in conjunction with EPUS control, which is why the results from these methods are not included in the table. The third-order Bogacki–Shampine method is also not recommended for use in conjuction with the EPUS; although in this case it gave quite reasonable results in acceptable time, it was still substantially slower than the high order methods.

The error maps shown in this section are a sample of a wider range of tests, which were performed for two suction increments (i.e. no change of suction or reduction of suction by 50 kPa) and three integration tolerances (1%, 0.1% and 0.01%). The results presented refer to an integration tolerance of 1%, as this order of magnitude is probably closest to the accuracy often used in FE applications, and a reduction of suction by 50kPa, as wetting paths seemed to be most taxing for the stress integration algorithms.

Table 7.2. Percentage of points in the mesh with maximum error (in any of the stress components) above the set tolearance.

Method	Error control type	Integration accuracy set to:			Average [%]
		1 %	0.1 %	0.01 %	
		Points with error exceeding tolerance [%]			
Modified Euler	EPS	13.4	15.6	16.8	15.3
Nystrom	EPS	8.0	10.0	11.2	9.7
Bogacki-Shampine 3(2)	EPS	24.8	32.8	40.0	32.5
	EPUS	1.56	2.34	1.38	1.76
Runge – Kutta 4(3)	EPS	16.6	19.1	22.6	19.4
	EPUS	0.37	0.04	0.03	0.15
Cash – Karp	EPS	9.4	11.2	8.4	9.67
	EPUS	0.05	0.02	0.1	0.06
England	EPS	6.9	7.6	8.5	7.67
	EPUS	0	0	0	0
Dormand – Prince	EPS	3.7	4.8	5.6	4.7
	EPUS	0.02	0	0	0
Bogacki – Shampine 5(4)	EPS	10.1	22.2	18.8	17.0
	EPUS	1.75	0.98	0.30	1.01
Extrapolation	Any	0	0	0	0
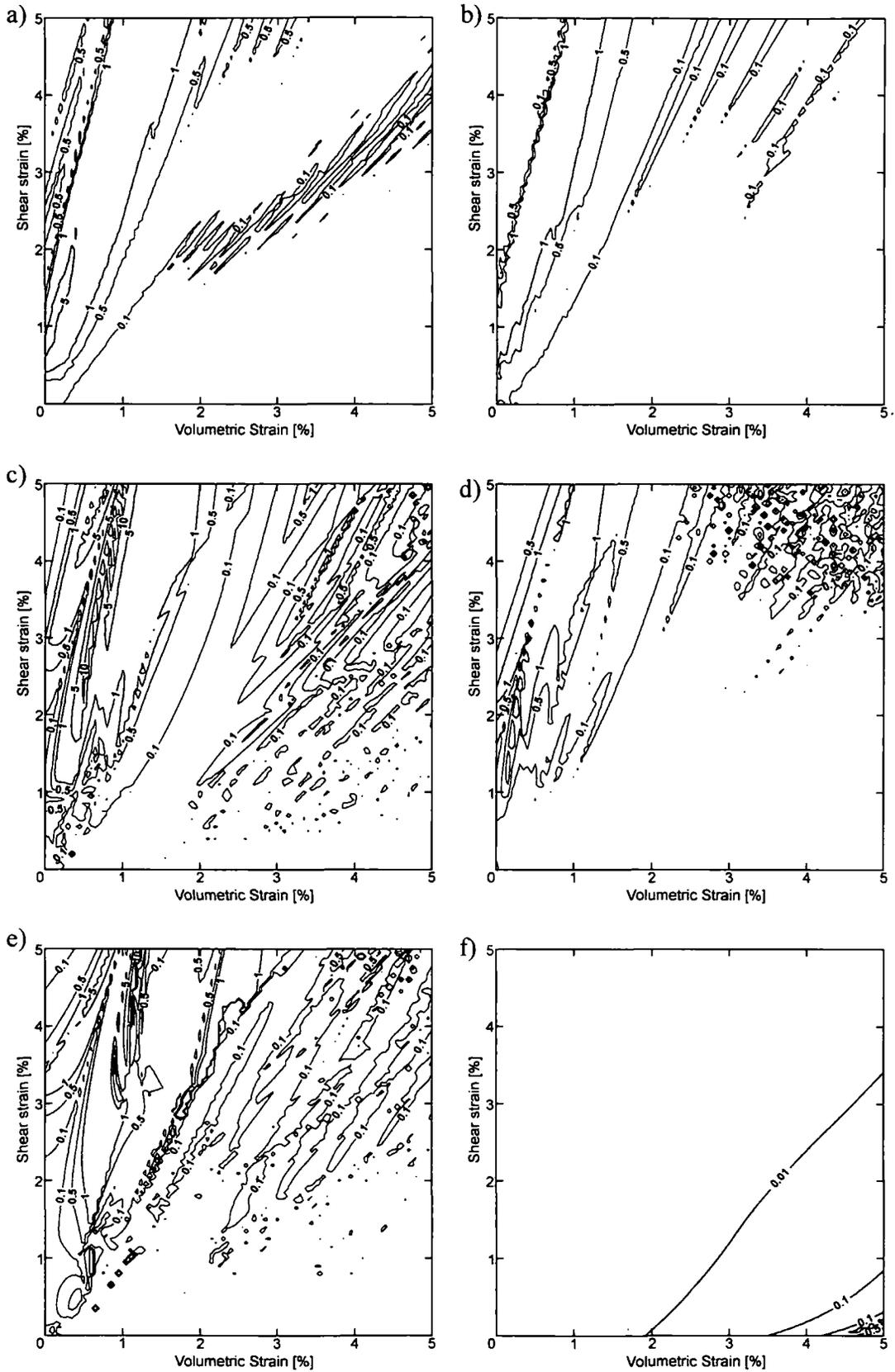
Figure 7.16. Error maps for EPS error control. Percentage error in stresses integrated with: a) Modified Euler 2(1), b) Nystrom 3(2) c) fourth order R-K method 4(3) d) England 5(4) e) Cash–Karp 5(4) f) extrapolation method. In all cases the tolerance was set to 1%. Areas with error larger than 1% are greyed out.
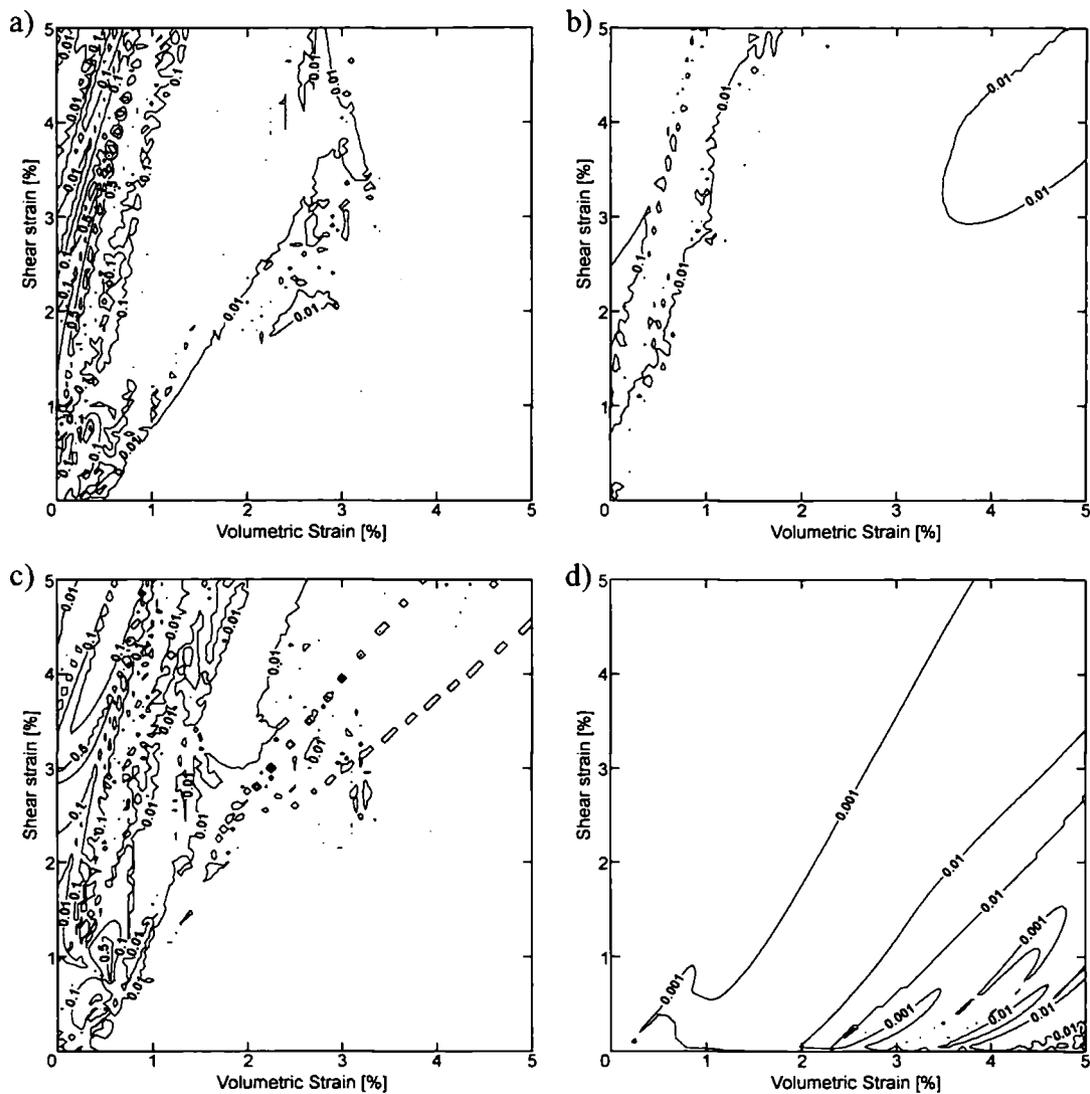
Figure 7.17. Error maps for EPUS error control. Percentage error in stresses integrated with: a) fourth order R-K method 4(3), b) England 5(4) c) Cash-Karp 5(4) and d) extrapolation method. In all cases the tolerance was set to 1%. Areas with error larger than 1% are greyed out.

7.3. Comparison between explicit and implicit stress integration algorithms

In this section, some general findings about accuracy and efficiency of explicit and implicit stress integration algorithms are given. This work was undertaken in cooperation with Matthias Hofmann from Innsbruck University. All the implicit schemes used for comparison have been created in Innsbruck University. The implicit algorithms used were: (i) an algorithm similar to that described by Simo and Hughes (1998) and Vaunat et al. (2000), (ii) implicit algorithms further improved by Hofmann (see Hofmann 2009).

156

The explicit algorithms used in the comparison were the Modified Euler, Nystrom, Cash-Karp and extrapolation, all coupled with Error Per Step (EPS) error control. The algorithms adopted a TOL value of 10%. Such a high value was used in an attempt to reduce the difference in running time, as the explicit algorithms were several times slower than the best implicit scheme created by Hofmann.

The difference in the calculation time required by the implicit and explicit algorithms may be due to a range of factors. One of the reasons may be the size of the matrices used. The quick implicit schemes were coded in Fortran and were highly optimised. The explicit algorithms were coded in C++ with regard of reusability and used full 6x6 matrices. The multiplication of 6x6 matrix by another 6x6 matrix takes 216 operations (as coded) comparing to 8 in the case of 2x2 matrices and 27 in the case of 3x3 matrices. This gives 27 or 8 times more operations respectively. It is entirely feasible to create the explicit algorithm operating on such matrices that would result in comparable increase of integration speed. This difference in speed is similar for implicit algorithms, where the general scheme is more than a level of magnitude slower than the algorithms created specifically for the BBM.

The algorithms were compared against each other using three sets of parameters for the Barcelona Basic Model. Two sets of parameters were taken from the Alonso et al. (1990) paper (corresponding to Compacted Kaolin and Lower Cromer till). The final test was performed with the parameters calibrated for the Barcelona sandy silt, tested by Barrera (2002).

The major outcomes of the study were that (i) the general implicit algorithm was less accurate and less stable than the explicit algorithm, meaning that it failed to converge for larger strain increments (see Fig. 7.18), (ii) the accuracy of the advanced implicit algorithms is comparable to the accuracy of explicit algorithms with set tolerance of 10%, though the explicit algorithms were more accurate for large strain increments (see Figs 7.19 and 7.20), (iii) the advanced implicit algorithms were stable and consistently around ten times faster than the explicit algorithms.

These outcomes are notable as the implicit algorithms are often believed to be more robust than the explicit ones. As the accuracy of the explicit algorithm was set to 10% which is a high value, it also shows that the implicit schemes are not that accurate. On the other hand, the explicit algorithm can be as accurate as desired due to choice of the TOL value. This can be regarded as an advantage over implicit schemes. However, the absolute error in stresses integrated with the implicit algorithms is likely to be

acceptable in most engineering analyses, especially given that large strain increments are fairly rare in real FE simulations (as global convergence often requires small substeps in the global Newton-Raphson iterations).

The advanced implicit algorithms were consistently faster than the explicit ones (this may be due to differences in coding, as mentioned above). However, the speed of the general implicit algorithm was comparable to the explicit algorithms. This general algorithm was also unstable when the strain increment was too large. The improved implicit algorithms were stable even for relatively large strain increments.

Finally, the implicit algorithms offered smooth error maps compared with the explicit algorithms (compare Figs 7.19 and 7.20). This means that one can be fairly sure of high accuracy when the strain increment is small enough. For explicit schemes, sudden changes of error may appear when more than one substep is required to satisfy the error criterion. Sometimes the local error control may be misled and the stress is integrated with one substep when more substeps are in fact needed. This is less true for the extrapolation scheme, where the global error control is used and this algorithm offered a more consistent error distribution. Further details of these comparisons can be found in Solowski and Hofmann (2009).
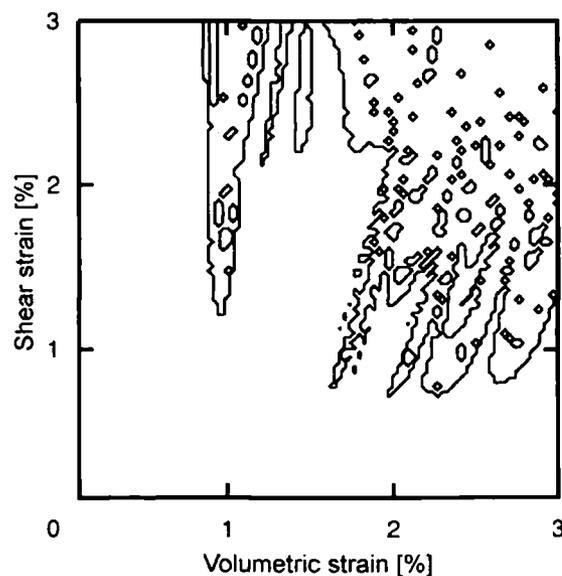
Figure 7.18. Shaded areas of the map indicate non – convergence of the general implicit algorithm. Tests were done for BBM with parameters for Lower Cromer till (Alonso 1990). The initial stress state was p=500 kPa q=0, initial suction 800 kPa and suction increment -300 kPa, constant for each strain increment (volumetric and shear strain increment were as indicated on the axes). Data obtained by Solowski and Hofmann.
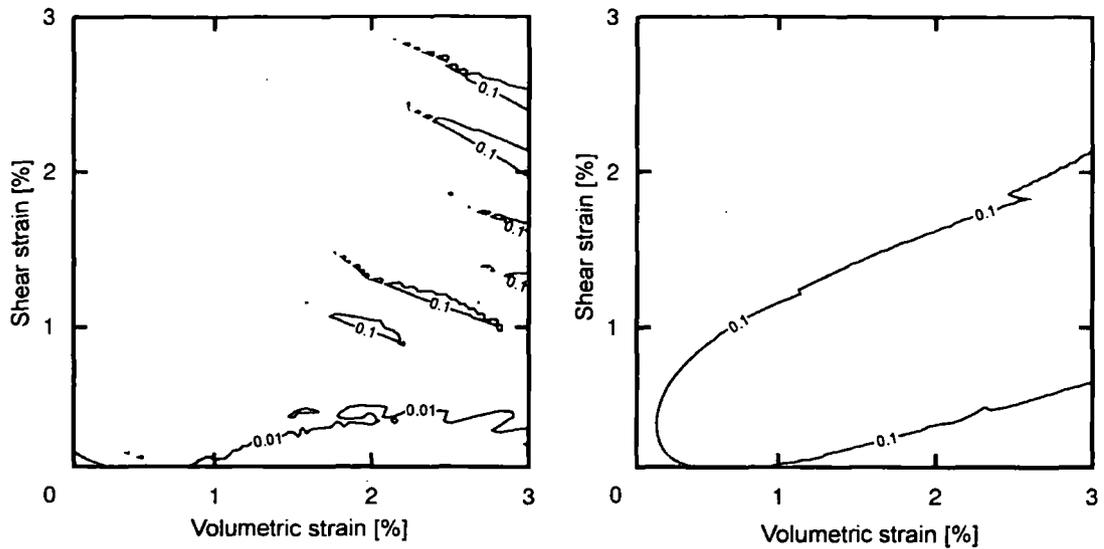
Figure 7.19. Percentage error in mean net stress integrated with explicit Modified Euler scheme (left) and advanced implicit algorithm (right). BBM parameters, strain increment, suction increment and initial stress state same as in Fig. 7.18. Data obtained by Solowski and Hofmann.
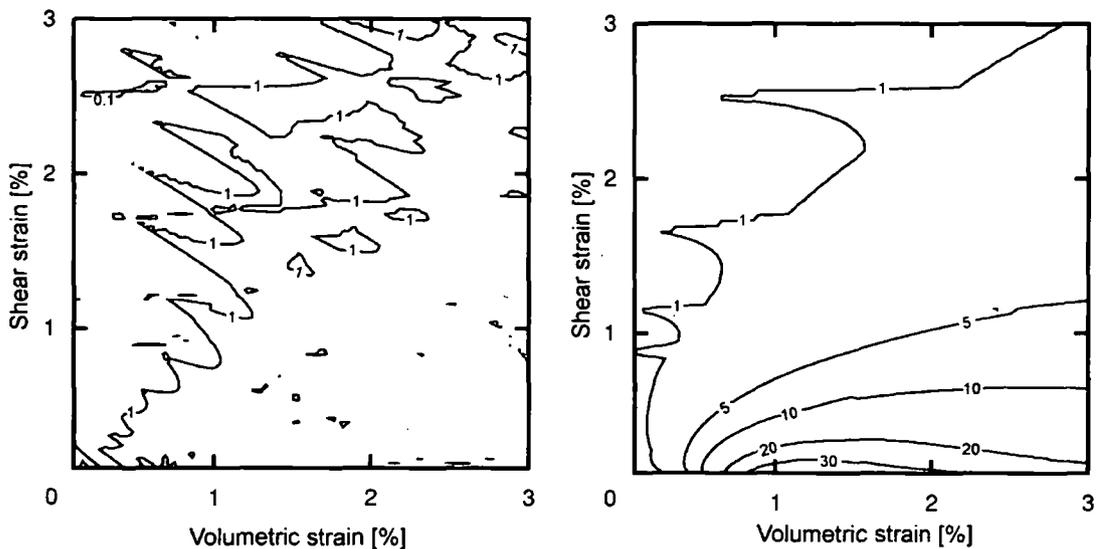
Figure 7.20. Percentage error in shear stress integrated with explicit Modified Euler scheme (left) and advanced implicit algorithm (right). BBM parameters, strain increment, suction increment and initial stress state same as in Fig. 7.18. The large percentage error in the case of implicit algorithm (left) is misleading, as the absolute value of shear stress was low for increments with small shear strain increment. Data obtained by Solowski and Hofmann.

7.4. Conclusions

The validation of the explicit algorithms with substepping and error control developed in this work, together with an evaluation of their efficiency and accuracy, has been presented in this chapter. Based on the performed tests, it appears that the main advantages of stress integration with the proposed explicit schemes are accuracy and robustness. The explicit algorithms are also not difficult to code. If an integration error smaller than the set tolerance must be ensured for all strain increments, then it is advisable to use either Runge-Kutta schemes in combination with the Error Per Unit Step (EPUS) control or the extrapolation method regardless of the type of error control used. Unfortunately, the Runge-Kutta schemes with EPUS error control are significantly slower and not so robust compared with Runge-Kutta coupled with the usual Error Per Step (EPS) error control. To eliminate convergence problems associated with the EPUS error control, the extrapolation Method can be used instead. This algorithm offers superior robustness and ensures accuracy, but is slower than Runge-Kutta schemes.

The recommended algorithm for use with the EPS error control is the third order Runge-Kutta Nystrom scheme. This scheme is nearly as efficient as the Modified Euler scheme for low accuracies and competitive with high order Runge-Kutta schemes for high accuracies. When the EPUS error control method is used, any high order Runge-Kutta scheme is recommended. In the tests, the fifth order Runge-Kutta Cash-Karp was most efficient, but Rugne-Kutta England or Runge-Kutta Dormand-Prince schemes were almost equally as good.

Finally, the scheme that is most robust and has best error control among the algorithms tested is the extrapolation scheme. Unfortunately, stress integration with extrapolation is also slower then the stress integration performed with Runge-Kutta schemes.

The implicit schemes require more sophisticated coding and calculation of second order derivatives, which may be inconvenient for more advanced constitutive models. Fine tuning of the implicit algorithm to the given constitutive model is also needed; otherwise the implicit algorithm may neither be very robust nor very accurate. The advanced implicit schemes tend to work well and offer acceptable accuracy for most practical cases.

Due to integration errors, it is crucial that the implicit schemes are used with a consistent elasto-plastic tangent matrix in the global Newton-Raphson iteration. The

stability of the global solution with implicit stress integration and the continuum tangent elasto-plastic matrix is not sufficient. However, if the consistent tangent matrix is used, the solution asymptotically converges at a quadratic rate. This is often cited as a big advantage of implicit integration. In the explicit integration, no consistent tangent matrix is used. The tangent elasto-plastic matrix is used instead. As the accuracy of the explicit integration is much higher, this is usually not a problem; still more research in this area is required.

8. Conclusions, implications and recommendations

Research on partially saturated soil behaviour has progressed quickly recently, however, the field remains relatively immature. The work reported in this thesis has dealt with the constitutive modelling of unsaturated soil and the stress integration of such constitutive models.

In chapter three the theoretical derivation of water content and average mean stress in the menisci area of soil was given. Findings suggest that the average mean stress in the menisci area is essentially independent of the value of suction. That chapter also revealed that the menisci contribution to the mean stress can be very significant when the soil is fine grained. This contribution is however unlikely to be seen in reality, as the small particles are not arranged as assumed in the derivation (i.e. under simple cubic packing) but are typically grouped into larger clusters referred to as aggregates. Those aggregates are saturated and one can only speak about menisci formed between aggregates. This leads to a menisci contribution to the average stress in the range of tens of kPa. Such an amount can still be significant, especially since it does not depend a great deal on suction. It is, however, unclear whether the number of menisci connecting the aggregates is the same at low suction level. It is evident that soil must be unsaturated before the menisci are created, thus suction must be equal at least to the air entry value (or air expulsion value during wetting). It is thus likely that until suction attains a value in the range of tens of kPa, the aggregates would be difficult to distinguish (or the soil would be fully saturated) in a fine grained soil.

Chapter five introduces a multi–cell enhancement and its evolution (a random multi-cell enhancement) allowing construction of a new form of constitutive model. This novel concept in unsaturated soils does not require the introduction of any additional material constants to the constitutive models. It also seems that a multi-cell enhancement can be fairly simple to implement in a whole class of models for unsaturated soils that deal with suction and do not include any dependency on water retention behaviour. The use of the multi-cell enhancement provides several advantages. As illustrated in the example of the Barcelona Basic Model, the random multi-cell approach allows for a smoother transition between elastic and elasto-plastic states and the modelling of the increase of plastic deformation during cycles of wetting and

drying. The smoother transition between elastic and elasto-plastic states does not only allow a more realistic prediction of unsaturated soil behaviour, but also may improve stability of large scale Finite Element analyses. Additionally, the increase of deformations during cyclic wetting and drying (as given by the random multi-cell approach) is a well documented phenomenon and the ability to approximate such behaviour is an asset for any constitutive model for unsaturated soil. Motivated by considerations of the soil fabric, the multi-cell enhancement allows an engineer to get closer to address the microscale influence on the macroscopic behaviour of unsaturated soils. Such an approach may lead to improvements in soil modelling without any necessary increase in the number of material constants of the model. This is valuable, as additional material constants generally imply that more laboratory tests are required. The latter typically leads to an increase of expenses associated not only with the cost of additional laboratory tests but also with the time spent waiting for the results of those tests. Geotechnical laboratory data are often not so easy to interpret even by experienced researchers (compare d'Onza et al. 2008) and even relatively simple constitutive models are not straightforward to calibrate. Calibration of a complex model with large number of material parameters is usually even more difficult, especially when unique (uncoupled) physical phenomena cannot be identified (and measured) for each material constant.

Stress integration is one of the key issues when introducing an elasto-plastic constitutive model into Finite Element codes. This was addressed in chapter six which provides a detailed review of the explicit stress integration method. A great deal of attention is given to the accuracy and stability of the calculations. Thus an extrapolation method, a method not yet used for stress integration, was described alongside with a more accurate EPUS error control method. The stress integration methods were then compared in chapter seven. It appears that: (i) the EPUS error control properties are better than the traditional error control method, as given by Sloan (1987) but the Sloan approach is quicker and more stable, (ii) the global error control, as provided by the extrapolation method, essentially guarantees an error below a set tolerance, (iii) the extrapolation method offers superior stability compared to all other methods, but is slower, (iv) the traditional Runge-Kutta Modified Euler scheme is best when low accuracy is required and if is used with an error control method as proposed by Sloan (1987), (v) it may be advisable to use the Runge-Kutta Nystrom method instead of the Runge-Kutta Modified Euler method as it is nearly as efficient at lower accuracies and significantly faster when

a higher accuracy is required, (vi) high order Runge-Kutta methods have no advantage over the Nystrom and Modified Euler schemes unless a very high accuracy is required and (vii) if use of the EPUS error control is desired, then it should be coupled with a high order Runge-Kutta method due to both stability and efficiency reasons.

As the constitutive models for unsaturated soils are currently not implemented in the majority of commercial Finite Element codes, it is likely that some test cases for the evaluation of the algorithms may be needed. The benchmark tests used for evaluation of the stress integration algorithms for the Barcelona Basic Model, given in chapter seven, may allow engineers to check the accuracy and quality of stress integration algorithms in future commercial codes.

Partially saturated soil mechanics is a dynamic area of research. Thus it is not surprising that the understanding of unsaturated soil is still evolving. Yet, it appears that the microstructural behaviour of unsaturated soil is still not thoroughly understood. For example, it is unclear whether the soil dried from a remoulded state and compacted soils behave, in principle, similarly and it is uncertain just what are the requirements for a constitutive model to correctly model both kinds of soils.

Another issue that would benefit from further investigation is the shear strength of unsaturated soils. It is not so clear whether the conventional models are able to describe the shear strength properly. Also the shape of the yield locus and anisotropy present in unsaturated soils need to be better understood.

Because of those gaps in our understanding, creation of a constitutive model for unsaturated soils that would cover all the aspects of soil behaviour and provide valuable insights into the evolution of the soil microstructure appears to be possible only at some distant time in the future. Nevertheless, research in this direction and creation of constitutive models that not only describe macroscopic behaviour but also provide insight into microstructural changes of soil fabric is, in the author's opinion, highly desirable. Unsaturated soil mechanics is slow to be adopted by practicing engineers. This is partially because of a lack of implementation of a suitable constitutive model into the commercial Finite Element codes.

The comparisons between the explicit integration schemes suggest that some improvements in the area are possible – though it would be of course desirable to provide such a comparison not only on the level of single material (Gauss) point, but also on a structural level through a wide range Finite Element analyses. Only then could

the advantages of a given stress integration algorithm be truly assessed. Such comparisons could also answer the question about how big an influence the error in the stress integration algorithm has on results of the engineering analyses. It would be particularly interesting to see whether the high accuracy and stability of the extrapolation method leads to faster convergence of the global Finite Element solutions.

References

Alonso E.E., Gens A., Josa A. (1990) A constitutive model for partially saturated soils. *Géotechnique* **40**(3): 405-430.

Alonso E.E., Gens, A., Josa, A., Hight D.W. (1987) Special problems soils. General Reports. In: *Proceedings of the 9th European Conference on Soil Mechanics and Foundation Engineering.* Dublin. Vol.3: 1087-1146.

Alonso E.E., Vaunat J., Gens A. (1999) Modelling the mechanical behaviour of expansive clays. *Engineering Geology,* **54**:173-183.

Barrera M.B. (2002) *Estudio experimental del comportamiento hidro-mecanico de suelos colapsables.* PhD thesis. Universitat Politecnica de Catalunya, Barcelona, Spain (in Spanish).

Bishop A.W. (1954) The use of pore pressure coefficients in practice. *Géotechnique* **4**(4): 148-152.

Bishop A.W. (1959) The principle of effective stress. *Tek. Ukeblad,* Oslo, Norway, **106**(39):859-863.

Blatz J. A., Graham J. (2003) Elastic-plastic modelling of unsaturated soil using results from a new triaxial test with controlled suction. *Géotechnique* **53**(1):113–122.

Bogacki P., Shampine L.F. (1996) An efficient Runge-Kutta (4,5) pair. *Computers Math. Applic.* **32**(6):15-28. See also: www.netlib.org/ode/rksuite.

Bolzon G., Schrefler B., Zienkiewicz O.C. (1996) Elastoplastic soil constitutive laws generalised to partially saturated states. *Géotechnique* **46**(2): 279-289.

Borja R.I. (2004) Cam-Clay plasticity. Part V: A mathematical framework for three-phase deformation and strain localization analyses of partially saturated porous media. *Comput. Methods Appl. Mech. Engrg.* 193(48-51): 5301-5338.

Butcher J.C. (1987) The numerical analysis of ordinary differential equations. Runge – Kutta and general linear methods. Wiley, Chichester, UK.

Butterfield R. (1979) A natural compression law for soils (an advance on e-log p'), *Géotechnique* **29**(4):469-480.

Chan T.P., Govindaraju R.S. (2004) Estimating soil water retention curve from particle-size distribution data based on polydisperse sphere systems. *Vadose Zone Journal*, **3**:1443–1454.

Cho G.C. (2001) *Unsaturated soil stiffness and post-liquefaction soil strength*. PhD. Thesis. Georgia Institute of Technology.

Cho G.C. and Santamarina J.C. (2001) Unsaturated Particulate Materials – Particle-Level Studies. *Journal of Geotechnical and Geoenvronmental Engineering* **127**(1):84-96.

Colmenares Montañez J. E. (2002) *Suction and volume changes of compacted sand-bentonite mixtures*. PhD thesis. University of London. Imperial College. London, UK.

Cui Y.J., Delage P., Sultan N. (1995) An elasto-plastic model for compacted soils. Unsaturated soils. *Sols Non Saturés. Alonso & Delage Eds. Proceedings of the First International Conference in Unsaturated Soils. Paris 1995*. Vol. **2**:703-709. Balkema, Rotterdam.

Cuisinier O., Laloui L. (2004) Fabric evolution during hydromechanical loading of a compacted silt. *Int. J. Numer. Anal. Meth. Geomech.*, **28**:483-499.

Cui Y.J. (1993) *Etude du comportement d'un limon compacté non saturé et de sa modélisation dans un cadre élasto-plastique*. PhD thesis, ENPC, Paris.

Cui Y.J., Delage P. (1996) Yielding and plastic behaviour of an unsaturated compacted silt. *Géotechnique* **46**(2):291-311.

Day R.W. (1994) Swell-Shrink Behavior of Compacted Clay. Technical Note. *J. Geotech. Engrg.* **120**(3):618-623.

Delage P., Tessier D., Marcel-Audiger M. (1982) Use of the Cryoscan apparatus for observation of freeze-fractured planes of a sensitive Quebeck clay in scanning electron microscopy. *Can. Geotech. J.*, **19**:111-114.

Delage P., Lefebvre G., (1984) Study of the structure of a sensitive Champlain clay and of its evolution during consolidation. *Can. Geotech. J.*, **21**:21-35.

Delage P, Audiguier M., Cui Y-J, Howat M.D. (1996) Microstructure of a compacted silt. *Can. Geotech. J.* **33**:150-158.

Deuflhard P., Bornemann F. (2002) Scientific computing with ordinary differential equations. Text in applied mathematics 42. Springer.

Dolinar B, Trauner L. (2007) The impact of structure on the undrained shear strength of cohesive soils. *Engineering Geology* **92**:88-96.

D'Onza F., Gallipoli D., Wheeler S. (2007) MUSE Task B. Benchmark B8. Parameter determination for the Barcelona Basic Model. Unpublished, please contact the authors for a copy.

Dormand J. R. (1996) Numerical methods for differential equations. A computational approach. Boca Raton New York London Tokyo:CRC Press.

Dowell M. and Jarratt P. (1972) The "Pegasus" method for computing the root of an equation., *Nordisk Tidskr. Informationsbehandling (BIT. Numerical Mathematics)* **12**:503-508.

Estabragh A.R., Javadi A.A. (2006) Yielding of unsaturated compacted silty soil under anisotropic conditions. Proc. Fourth Int. Conf. on Unsat. Soils, Carefree, Phoenix, Arizona. ASCE, Vol 1:1259-1266.

Fisher R.A. (1926) On the capillary forces in an ideal soil; Correction of formuale given by W.B. Haines. *J. Agric. Sci.* London, **16**:492-505.

Ferber V., Auriol J.C., Magnan J.P., Cui Y.J., De Laure E., Gerente C. (2006) A microstructural model for the volume changes of unsaturated clayey soils due to wetting. Proc. Fourth Int. Conf. on Unsat. Soils, Carefree, Phoenix, Arizona. ASCE, Vol 1:861-872.

Fredlund D.G., Pham H.Q. (2006) A volume-mass constitutive model for unsaturated soils in terms of two independent stress variables. Proc. Fourth Int. Conf. on Unsat. Soils, Carefree, Phoenix, Arizona. ASCE, Vol 1:105-134.

Fredlund D.G., Rahardjo H. (1993) *Soil mechanics for unsaturated soils.* Wiley, New York.

Gallipoli D. (2000) *Constitutive and numerical modelling of unsaturated soils.* PhD thesis, University of Glasgow, UK.

Gallipoli D., Gens A., Sharma R., Vaunat J. (2003a) An elasto-plastic model for unsaturated soil incorporating the effects of suction and degree of saturation on mechanical behaviour. *Géotechnique* **53**(1):123–135.

Gallipoli D., Wheeler S.J., Karstunen M. (2003b) Modelling the variation of degree of saturation in a deformable unsaturated soil. *Géotechnique* **53**(1) :105 :112.

Gasparre A. (2005) *Advanced laboratory characterisation of London Clay.* PhD Thesis. Imperial College, London, UK.

Gear W.G. (1971) *Numerical initial value problems in ordinary differential equations.* Englewood Cliffs, New Jersey USA: Prentice Hall Inc.

Geiser F. (1999) *Comportement mécanique d'un limon non saturé.* PhD thesis (in French), EPFL, Lausanne, Switzerland.

Gens A., Alonso E.E. (1992) A framework for the behaviour of unsaturated expansive clays. *Can. Geotech. J.* **29**:1013-1032.

van Genuchten M. Th. (1980) A closed-form equation for predicting the hydraulic conductivity of unsaturated soils. *Soil Sci. Soc. Am. J.* **44**(5):892-898.

Gillott J.E., (1973) Methods of sample preparation in microstructural analysis of soil. Soil microscopy. Proc. 4th international working-meeting on soil micro-morphology, Kingston, 143-164.

Georgiadis K. (2003) *Development, implementation and application of partially saturated soil models in finite element analysis.* PhD thesis, Imperial College, London, UK

Georgiadis K., Potts D.M., Zdravkovic L. (2005) Three-dimensional constitutive model for partially saturated soils. *Int. Jour. of Geomech. ASCE.* **5**(3):244-256.

Ghorbel A., Leroueil S. (2006) An elasto-plastic model for unsaturated soils. Proc. Fourth Int. Conf. on Unsat. Soils, Carefree, Phoenix, Arizona. ASCE, Vol 2:1908-1919.

González N., Colmenares J.E. (2006) Influence of matric suction on the volume change behaviour of a compacted clayey soil. Proc. Fourth Int. Conf. on Unsat. Soils, Carefree, Phoenix, Arizona. ASCE, Vol 1:825-836.

Gragg W.B. (1965) On extrapolation algorithms for ordinary initial value problems. *SIAM J. Numer. Anal.* **2**:384-403.

Hofmann M. H. (2009?) PhD thesis. Innsbruck University, Innsbruck, Austria.

Hong Z., Tateishi Y, Han J. (2006) Experimental study of macro- and microbehaviour of natural diatomite. *J. Geotech. Geoenv. Eng. ASCE* **132**(5):603-610.

Hassanizadeh M., Gray W.G. (1990) Mechanics and thermodynamics of multiphase flow in porous media including interphase boundaries. *Adv. Water Resour.* **13**:169-186.

Hillel D. (1998) *Environmental soil physics: fundamentals, applications, and environmental considerations.* Academic Press (Elsevier).

Houlsby G. T. (1981) *A Study of Plasticity Theories and Their Applicability to Soils*, Ph.D. Thesis, University of Cambridge, UK.

Houlsby G. T. (1997) The work input to an unsaturated granular material. *Géotechnique* **47**(1):193-196.

Hutter K., Laloui L. and Vuliet L. (1999) Thermodynamically based mixture models of saturated and unsaturated soils. *Mechanics of Cohesive-Frictional Materials* **4**:295-338.

Imre E., Rajkai K., Firgi T., Trang Q.P., Telekes G. (2006) Closed-form functions for the soil water-retention curve of sand fractions and sand mixtures. Proc. Fourth Int. Conf. on Unsat. Soils, Carefree, Phoenix, Arizona. ASCE, Vol 2:2408-2419.

Jafari M.K., Shafiee A. 2004. Mechanical behaviour of compacted composite clays. *Can. Geotech. J.* **41**:1152-1167.

Josa Garcia-Tornel A. (1988) *Un modelo elastoplastico para suelos no saturados.* PhD thesis (in Spanish), UPC, Barcelona, Spain.

Jotisankasa A. (2005) *Collapse behaviour of a compacted silty clay.* PhD thesis. University of London. Imperial College. London, UK.

Kohler R., Hofstetter G. (2008) A cap model for partially saturated soils. *Int. J. Numer. Anal. Meth. Geomech.* **32**:981–1004.

Koliji A., Laloui L., Cuisinier O., Vulliet L. (2006) Suction induced effects on the fabric of a structured soil. *Transport in Porous Media* **64**:261-278.

170

Koliji A. (2008) *Mechanical behaviour of unsaturated aggregated soils.* PhD thesis, Ecole Polytechnique Fédérale de Lausanne, Lausanne.

Laloui L., François B., Nuth M., Peron H., Koliji A. (2008) A thermo-hydro-mechanical stress-strain framework for modelling the performance of clay barriers in deep geological repositories for radioactive waste , in: *Unsaturated Soils: Advances in Geo-Engineering – Toll et al. Eds. Proceedings from the First European Conference on Unsaturated Soils E-UNSAT, Durham, UK.* 63-80. Taylor & Francis Group, London, UK.

Lambert J.B. (1973) *Computational methods in ordinary differential equations.* London: John Wiley & Sons.

Lee H.J., Schiesser W.E. (2003) Ordinary and partial differential equation routines in C, C++, Fortran, Java, Maple, and Matlab. Boca Raton:CRC Press.

Li X.S. (2007) Thermodynamics-based constitutive framework for unsaturated soils. 1:Theory. *Géotechnique* **57**(5):411-422.

Likos W.J., Lu N. (2004) Hysteresis of capillary stress in unsaturated granular soil. *ASCE Journal of Engineering Mechanics* **130**(6):646-655.

Lourenço S. D. N. (2008) *Suction measurements and water retention in unsaturated soils.* PhD thesis, Durham University, Durham, UK.

Lu N., Likos W.J. (2004) *Unsaturated soil mechanics.* Wiley, New Jersey.

Lu N., Likos W.J. (2006) Suction stress characteristic curve for unsaturated soils. *ASCE Journal of Geotechnical nad Geoenvironmental Engineering* **132**(2):131-142.

Loret B., Khalili N. (2002) An effective stress elastic–plastic model for unsaturated porous media. *Mechanics of Materials* 34:97–116.

Marinho F.A.M. (1994) *Shrinkage behaviour of some plastic soils.* PhD thesis, Imperical College, London, UK.

Marinho F.A.M. (2005) Nature of soil-water characteristic curve for plastic soils. *J. Geotech. Geoenv. Eng. ASCE* **131**(5):654-661.

Marinho F.A.M. (2006) A method of estimating the soil-water retention curve for plastic soils. Proc. Fourth Int. Conf. on Unsat. Soils, Carefree, Phoenix, Arizona. ASCE, Vol 2:1473-1481.

Mašin D., Khalili N. (2008) Modelling of the collapsible behaviour of unsaturated soils in hypoplasticity. In: *Unsaturated Soils: Advances in Geo-Engineering – Toll et al. Eds. Proceedings from the First European Conference on Unsaturated Soils E-UNSAT, Durham, UK.* 659-665. Taylor & Francis Group, London, UK.

Mei C.C. (2004) MIT Lecture notes: Fluid dynamics. Chapter 7.b Surface tension. Can be found at: http://web.mit.edu/1.63/www/lecnote.html. Last accessed 18 July 2008.

Miao L, Houston S.L., Cui Y., Yuan J. (2007) Relationship between soil structure and mechanical behaviour for an expansive unsaturated clay. *Can. Geotech. J.* **44**:126-137.

Monroy R. (2005) *The influence of load and suction changes on the volumetric behaviour of compacted London clay.* PhD thesis. Imperial College, London, UK.

Muir Wood D. (1990). *Soil behaviour and critical state soil mechanics.* Cambridge Univ. Press, Cambridge UK.

Nishimura T., Toyota H. (2002) Interpretation of the direct shear strength of desiccated compacted soil in high soil suction ranges. *Environmental Geomechanics*, Monte Verita, 201-206.

Nuth M., Laloui L. (2008) Advanced hydro-mechanical coupling for unified constitutive modelling of unsaturated soils. , in: *Unsaturated Soils: Advances in Geo-Engineering – Toll et al. Eds. Proceedings from the First European Conference on Unsaturated Soils E-UNSAT, Durham, UK.* 559-565. Taylor & Francis Group, London, UK.

Pham H.Q., Fredlund D.G., Barbour S.L. (2005) A study of hysteresis models for sol-water characteristic curves. . *Can. Geotech. J.* **42**:1548-1568.

Pham H.Q., Fredlund D.G. (2008) Equations for the entire soil-water characteristic curve of a volume change soil. *Can. Geotech. J.* **45**:443-453.

Potts D.M., Ganendra D. (1994) An evaluation of substepping and implicit stress point algorithms. Comput. Methods Appl. Mech. Engrg. **119**:341-354.

Potts D.M., Gens A. (1985) A critical assessment of methods of correcting for drift from the yield surface in elasto-plastic finite element analysis. *Int. J. Numer. Anal. Meth. Geomech.* **9**:149-159.

Potts D.M., Zdravkovic L. (1999) *Finite element analysis in geotechnical engineering. Theory.* London, Thomas Telford Publishing.

Press W.H., Teukolsky S.A., Vetterling W.T., Flannery B.P. (2002) Numerical recipes in C++. The art of scientific computing. Second edition. Cambridge University Press.

Rampino C., Mancuso C., Vinale F. (2000) Experimental behaviour and modelling of an unsaturated compacted soil. *Can. Geotech. J.* 37:748-763.

Raveendiraraj A. (2008?) PhD thesis. Glasgow University, UK. Unpublished.

Romero E., (1999) *Characterisation and thermal-hydro-mechanical behaviour of unsaturated Boom clay: an experimental study.* Ph.D. thesis, Universitat Politecnica de Catalunya, Barcelona, Spain.

Roscoe K.H., Burland J.B. (1968) On the generalised stress-strain behaviour of 'wet' clay. Engineering Plasticity (J. Heyman, Leckie F.A. eds), Cambridge University Press, Cambridge, 535-609.

Russel A.R., Khalili N. (2006) A unified bounding surface plasticity model for unsaturated soils. *Int. J. Numer. Anal. Meth. Geomech,* **30**: 181-212.

Russo G., Dal Vecchio S., Macolo G. (2007) Microstructure of a lime stabilised compacted silt. Proc. of the 2nd International Conference "Mechanics of Unsaturated Soils", Experimental Unsaturated Soil Mechanics Series: Springer Proceedings in Physics , Vol. 112, 49-56, Springer, Weimar, Germany.

Sánchez M., Gens A., Guimarães L.N., Olivella S. (2005) A double structure generalized plasticity model for expansive materials. *Int. J. Numer. Anal. Meth. Geomech.,* **29**:751-787.

Shampine L. F. (1994) Numerical solution of ordinary differential equations. New York, London: Chapman & Hall.

Sharma R.S. (1998) *Mechanical behaviour of unsaturated highly expansive clays.* PhD thesis, Keble College, University of Oxford, UK.

Sheng D., Fredlund D.G., Gens A. (2008) A new modelling approach for unsaturated soils using independent stress variables. *Can. Geotech. J.,* **45**:511-534.

Sheng D., Sloan S. W., Gens A., Smith D. W. (2003a) Finite element formulation and algorithms for unsaturated soils. Part I: Theory. *Int. J. Numer. Anal. Meth. Geomech.*, **27**:745-765.

Sheng D., Sloan S. W., Gens A., Smith D. W. (2003b) Finite element formulation and algorithms for unsaturated soils. Part II: Verification and application. *Int. J. Numer. Anal. Meth. Geomech.*, **27**:767-790.

Sheng D., Sloan S.W., Yu H.S. (2000) Aspects of finite element implementation of critical state models. *Comp. Mech.* **26**:185-196.

Simo J.C., Hughes T.J.R. (1998) *Computational inelasticity*. Interdisciplinary applied mathematics series, vol. 7. Springer.

Sivakumar V. (1993) *A critical state framework for unsaturated soil*. PhD thesis. University of Sheffield, UK.

Sloan S. W. (1987) Substepping schemes for the numerical integration of elastoplastic stress-strain relations. *Int. J. Numer. Methods Eng.* 24: 893-911.

Sloan S. W., Abbo A. J., Sheng D. (2001) Refined explicit integration of elastoplastic models with automatic error control. *Engineering Computations* **18**(1/2): 121-154.

Solowski W.T., Hofmann M.H. (planned 2009) Comparison of efficiency and accuracy of explicit and implicit integration schemes for Barcelona Basic Model.

Sun D., Sheng D., Sloan S.W. (2007a) Elastoplastic modelling of hydraulic and stress–strain behaviour of unsaturated soils. *Mechanics of Materials* **39**:212–221.

Sun D., Sheng D., Xu Y. (2007b) Collapse behaviour of unsaturated compacted soil with different initial densities. *Can. Geotech. J.*, **44**:673-686.

Stange C.F., Horn R. (2005) Modelling the soil water retention curve for conditions of variable porosity. *Vadose Zone Journal* **4**:602–613.

Stoer J., Bulirsch R. (2002) *Introduction to Numerical Analysis*. Third Edition. New York:Springer.

Stropeit K., Wheeler S.J, Cui Y.J. (2008) An anisotropic elasto-plastic model for unsaturated soils, in: *Unsaturated Soils: Advances in Geo-Engineering – Toll et al. Eds. Proceedings from the First European Conference on Unsaturated Soils E-UNSAT, Durham, UK.* 625-631. Taylor & Francis Group, London, UK.

Tamagnini R. (2004) An extended Cam-Clay model for unsaturated soils with hydraulic hysteresis. Technical Note. *Géotechnique,* **54**(3):223–228.

Tarantino A. (2007) Coupling between mechanical and water retention behaviour in unsaturated soils. Presentation during MUSE school in Naples. May be downloaded from MUSE website muse.dur.ac.uk.

Tarantino A. (2008) A new model for water retention behaviour. To be published in *Géotechnique.*

Thom R, Sivakumar V., Murray E.J., Mackinnon P. (2007) Pore size distribution of unsaturated compacted kaolin: the initial states and final states following saturation. *Géotechnique,* **57**(5):469-474.

Thu T.M., Rahardjo H., Leong E.-C. (2007) Elastoplastic model for unsaturated soil wih incorporation of the soil-water characteristic curve. *Can. Geotech. J.* **44**:62-77.

Toll D.G. (1990) A framework for unsaturated soil behaviour. *Géotechnique,* **40**(1):31-44.

Toll, D.G. (2000) The influence of fabric on the shear behaviour of unsaturated compacted soils. in *Advances in Unsaturated Geotechnics* (proceedings of GeoDenver 2000 conference, Shackelford, Houston, Chang Eds.), Geotechnical Special Publication (99):222-234, ASCE.

Toll D.G., Ong B.H. (2003) Critical-state paramters for an unsaturated residual sandy clay. *Géotechnique,* **53**(1):93-103.

Vasallo R. (2003) *Compartamento di terreni costipati non saturi a piccolo, medie e grandi deformazioni.* PhD thesis (in Italian), Università di Roma "La Sapienza" and Università di Napoli "Federico II", Naples, Italy.

Vaunat J., Cante J.C., Ledesma A., Gens A. (2000) A stress point algorithm for an elastoplastic model in unsaturated soils. *International Journal of Plasticity* **16**: 121-141.

Vaunat J. (2007) MUSE Task C. Benchmark for Task C5b "Collapse of a soil column by wetting" Specifications. Unpublished, please contact author for a copy.

Vaunat J., Merchán V., Romero E., Pineda J. (2007) Residual strength of clays at high suctions. Proc. of the 2nd International Conference "Mechanics of Unsaturated

Soils", Theoretical and Numerical Unsaturated Soil Mechanics Series: Springer Proceedings in Physics , Vol. 113, 151-162, Springer, Weimar, Germany.

Vesga L.F., Vallejo L.E. (2006) Direct and indirect tensile tests for measuring the equivalent effective stress in a kaolinite clay. Proc. Fourth Int. Conf. on Unsat. Soils, Carefree, Phoenix, Arizona. ASCE, Vol 1:1290-1301.

Villar M.V., (2000) Thermo-hydro-mechanical characterization of Cabo de Gata Bentonite. Ph.D. thesis. Complutense University, Madrid, Spain (in Spanish).

Wang Y.-H., Siu W.-K., (2006) Structure characteristics and mechanical properties of kaolinite soils. I. Surface charges and structural characterizations. *Can. Geotech. J.* **43**:587-600,

Wang Y.-H., Siu W.-K., (2006) Structure characteristics and mechanical properties of kaolinite soils. II. Effects of structure on mechanical properties. *Can. Geotech. J.* **43**:601-617.

Wang Y.-H., Xu D., (2007) Dual porosity and secondary consolidation. *J. Geotech. Geoenv. Eng .ASCE* **133**(7):793-801.

Wheeler S.J., Gallipoli D., Karstunen M. (2002) Comments on use of the Barcelona Basic Model for unsaturated soils. Int. J. Numer. Anal. Meth. Geomech. **26**:1561-1571.

Wheeler S.J., Sharma R.J., Buisson M.S.R. (2003) Coupling of hydraulic hysteresis and stress-strain behaviour in unsaturated soils. *Géotechnique* **53**(1):41–54.

Wheeler S.J., Sivakumar V. (1995) An elasto-plastic critical state framework for unsaturated soil. *Géotechnique,* **45**(1):35–53.

Yudhbir (1982) Collapsing behaviour of residual soils. Proc. 7th Southeast Asia Geot. Conf., Hong Kong, vol. 1:915–930.

Zhang G, Germaine J.T., Whittle A. J., Ladd C.C., (2003) Soil structure of a highly weathered old alluvium. *Géotechnique,* **54**(7):27–40.

Appendix: Runge-Kutta pairs coefficients

This appendix provides a list of tables (for each of the eight Runge-Kutta schemes used in this work) with the relevant values of the coefficients $a^{(ij)}$, $b^{(i)}$, $c^{(i)}$ and $d^{(i)}$ as defined by equations (6.7) and (6.8). The number of rows in each table corresponds to the number of stages NoS of the method. The description (a,b) denotes a scheme of order a with an embedded error estimation scheme of order b.

Table A.1. Modified Euler-Runge-Kutta (2,1) (Sloan 1987)

Stage number (i)	$c^{(i)}$	$a^{(i1)}$	$b^{(i)}$	$d^{(i)}$
1	0	-	$\dfrac{1}{2}$	1
2	1	1	$\dfrac{1}{2}$	0

Table A.2. Midpoint-Runge-Kutta (2,1) (Sloan 1987)

Stage number (i)	$c^{(i)}$	$a^{(i1)}$	$b^{(i)}$	$d^{(i)}$
1	0	-	0	1
2	0.5	0.5	1	0

Table A.3. Nystrom-Runge-Kutta (3,2) (Lee and Schiesser 2003)

Stage number (i)	$c^{(i)}$	$a^{(i1)}$	$a^{(i2)}$	$b^{(i)}$	$d^{(i)}$
1	0	-	-	$\dfrac{2}{8}$	$\dfrac{1}{4}$
2	$\dfrac{2}{3}$	$\dfrac{2}{3}$	-	$\dfrac{3}{8}$	$\dfrac{3}{4}$
3	$\dfrac{2}{3}$	0	$\dfrac{2}{3}$	$\dfrac{3}{8}$	0

Table A.4 Bogacki - Shampine Parameters for Embedded Runge- Kutta method (3,2) – four stages FSAL (first same as last) procedure (Bogacki and Shampine 1996)

i	$c^{(i)}$	$a^{(ij)}$			$b^{(i)}$	$d^{(i)}$
1	0	-	-	-	$\dfrac{2}{9}$	$\dfrac{7}{24}$
2	$\dfrac{1}{2}$	$\dfrac{1}{2}$	-	-	$\dfrac{1}{3}$	$\dfrac{1}{4}$
3	$\dfrac{3}{4}$	0	$\dfrac{3}{4}$	-	$\dfrac{4}{9}$	$\dfrac{1}{3}$
4	1	$\dfrac{2}{9}$	$\dfrac{1}{3}$	$\dfrac{4}{9}$	0	$\dfrac{1}{8}$
	j=	1	2	3	-	-

Table A.5. Parameters for Runge-Kutta method (4,3) (Lee and Schiesser 2003) Error estimate coefficients given instead of the third order solution.

i	$c^{(i)}$	$a^{(ij)}$				$b^{(i)}$	$e^{(i)}$
1	0	-	-	-	-	$\dfrac{1}{10}$	$-\dfrac{1}{15}$
2	$\dfrac{1}{3}$	$\dfrac{1}{3}$	-	-	-	0	0
3	$\dfrac{1}{3}$	$\dfrac{1}{6}$	$\dfrac{1}{6}$	-	-	$\dfrac{3}{10}$	$\dfrac{3}{10}$
4	$\dfrac{1}{2}$	$\dfrac{1}{8}$	0	$\dfrac{3}{8}$	-	$\dfrac{4}{10}$	$-\dfrac{4}{15}$
5	1	$\dfrac{1}{2}$	0	$-\dfrac{3}{2}$	2	$\dfrac{2}{10}$	$\dfrac{1}{30}$
	j=	1	2	3	4	-	-

Table A.6. Parameters for England-Runge-Kutta method (5,4) (Sloan 1987, Lee and Schiesser 2003) Error estimate coefficients given instead of the fourth order solution.

i	$c^{(i)}$	$a^{(ij)}$					$b^{(i)}$	$e^{(i)}$
1	0	-	-	-	-	-	$\dfrac{14}{336}$	$-\dfrac{42}{336}$
2	$\dfrac{1}{2}$	$\dfrac{1}{2}$	-	-	-	-	0	0
3	$\dfrac{1}{2}$	$\dfrac{1}{4}$	$\dfrac{1}{4}$	-	-	-	0	$-\dfrac{224}{336}$
4	1	0	-1	2	-	-	$\dfrac{35}{336}$	$-\dfrac{21}{336}$
5	$\dfrac{2}{3}$	$\dfrac{7}{27}$	$\dfrac{10}{27}$	0	$\dfrac{1}{27}$	-	$\dfrac{162}{336}$	$\dfrac{162}{336}$
6	$\dfrac{2}{10}$	$\dfrac{28}{625}$	$-\dfrac{125}{625}$	$\dfrac{546}{625}$	$\dfrac{54}{625}$	$-\dfrac{378}{625}$	$\dfrac{125}{336}$	$\dfrac{125}{336}$
	j=	1	2	3	4	5	-	-

Table A.7. Parameters for Cash-Karp Runge-Kutta method (5,4) (Press et al. 2002, Lee and Schiesser 2003)

i	$c^{(i)}$	$a^{(ij)}$					$b^{(i)}$	$d^{(i)}$
1	0	-	-	-	-	-	$\dfrac{37}{378}$	$\dfrac{2825}{27648}$
2	$\dfrac{2}{10}$	$\dfrac{2}{10}$	-	-	-	-	0	0
3	$\dfrac{3}{10}$	$\dfrac{3}{40}$	$\dfrac{9}{40}$	-	-	-	$\dfrac{250}{621}$	$\dfrac{18575}{48384}$
4	$\dfrac{6}{10}$	$\dfrac{3}{10}$	$-\dfrac{9}{10}$	$\dfrac{12}{10}$	-	-	$\dfrac{125}{594}$	$\dfrac{13525}{55296}$
5	1	$-\dfrac{11}{54}$	$\dfrac{5}{2}$	$-\dfrac{70}{27}$	$\dfrac{35}{27}$	-	0	$\dfrac{277}{14336}$
6	7/8	$\dfrac{1631}{55296}$	$\dfrac{175}{512}$	$\dfrac{575}{13824}$	$\dfrac{44275}{110592}$	$\dfrac{253}{4096}$	$\dfrac{512}{1771}$	$\dfrac{1}{4}$
	j=	1	2	3	4	5		

Table A.8. Parameters for Dormand-Prince (5,4). First Same as Last (FSAL) procedure. (Dormand 1996)

i	$c^{(i)}$	$a^{(ij)}$						$b^{(i)}$	$d^{(i)}$
1	0	-	-	-	-	-	-	$\dfrac{35}{384}$	$\dfrac{5179}{57600}$
2	$\dfrac{2}{10}$	$\dfrac{2}{10}$	-	-	-	-	-	0	0
3	$\dfrac{3}{10}$	$\dfrac{3}{40}$	$\dfrac{9}{40}$	-	-	-	-	$\dfrac{500}{1113}$	$\dfrac{7571}{16695}$
4	$\dfrac{8}{10}$	$\dfrac{44}{45}$	$-\dfrac{56}{15}$	$\dfrac{32}{9}$	-	-	-	$\dfrac{125}{192}$	$\dfrac{393}{640}$
5	$\dfrac{8}{9}$	$\dfrac{19372}{6561}$	$-\dfrac{25360}{2178}$	$\dfrac{64448}{6561}$	$-\dfrac{212}{729}$	-	-	$-\dfrac{2187}{6784}$	$-\dfrac{92097}{339200}$
6	1	$\dfrac{9017}{3168}$	$-\dfrac{355}{33}$	$\dfrac{46732}{5247}$	$\dfrac{49}{176}$	$-\dfrac{5103}{18656}$	-	$\dfrac{11}{84}$	$\dfrac{187}{2100}$
7	1	$\dfrac{35}{384}$	0	$\dfrac{500}{1113}$	$\dfrac{125}{192}$	$-\dfrac{2178}{6784}$	$\dfrac{11}{84}$	0	$\dfrac{1}{40}$
	$j=$	1	2	3	4	5	6		

Table A.9. Parameters for Bogacki - Shampine Runge – Kutta method (5,4) (Bogacki and Shampine 1996)

i	$c^{(i)}$	$a^{(ij)}$							$b^{(i)}$	$d^{(i)}$
1	0	-	-	-	-	-	-	-	$\dfrac{578}{8064}$	$\dfrac{2479}{34992}$
2	$\dfrac{1}{6}$	$\dfrac{1}{6}$	-	-	-	-	-	-	0	0
3	$\dfrac{2}{9}$	$\dfrac{2}{27}$	$\dfrac{4}{27}$	-	-	-	-	-	$\dfrac{4440339}{15491840}$	$\dfrac{123}{416}$
4	$\dfrac{3}{7}$	$\dfrac{183}{1372}$	$-\dfrac{162}{343}$	$\dfrac{1053}{1372}$	-	-	-	-	$\dfrac{24353}{124800}$	$\dfrac{612941}{3411720}$
5	$\dfrac{2}{3}$	$\dfrac{68}{297}$	$-\dfrac{4}{11}$	$\dfrac{42}{143}$	$\dfrac{1960}{3861}$	-	-	-	$\dfrac{387}{44800}$	$\dfrac{43}{1440}$
6	$\dfrac{3}{4}$	$\dfrac{597}{22528}$	$\dfrac{81}{352}$	$\dfrac{63099}{585728}$	$\dfrac{58653}{366080}$	$\dfrac{4617}{20480}$	-	-	$\dfrac{2152}{5985}$	$\dfrac{2272}{6561}$
7	1	$\dfrac{174197}{959244}$	$-\dfrac{30942}{79937}$	$\dfrac{8152137}{19744439}$	$\dfrac{666106}{1039181}$	$-\dfrac{29421}{29068}$	$\dfrac{482048}{414219}$	-	$\dfrac{7267}{94080}$	$\dfrac{79937}{1113912}$
8	1	$\dfrac{587}{8064}$	0	$\dfrac{4440339}{15491840}$	$\dfrac{24353}{124800}$	$\dfrac{387}{44800}$	$\dfrac{2152}{5985}$	$\dfrac{7267}{94080}$	0	$\dfrac{3293}{556956}$
	j=	1	2	3	4	5	6	7		

Note that this Bogacki-Shampine pair has an additional error estimate, different to the one given in the table above. The estimate has the coefficients $[-\dfrac{3}{1280},\ 0,\ \dfrac{6561}{632320},\ -\dfrac{343}{20800},\ \dfrac{243}{12800},\ -\dfrac{1}{95},\ 0]$. This error estimate does not require finishing the last stage of the procedure; in case this error estimate is too large, calculations of the last stage of the procedure should be skipped and the substep should be rejected.